

WAYNE STATE UNIVERSITY

DOCTORAL THESIS

---

Measurement of the Branching ratios of  
 $D_s \rightarrow \pi^0 l \nu$ ,  $\rho l \nu$  and  $K_s l \nu$  decays at  
Belle near  $\Upsilon(4s)$  and  $\Upsilon(5s)$  energies.

---

*Author: Sudeshna Ganguly*

*Supervisor: Giovanni Bonvicini*

*A thesis submitted to the Graduate School in partial fulfilment of the requirements  
for the degree of **Doctor of Philosophy***

*in the*

Department Of Physics and Astronomy

Wayne State University Approved by:

\_\_\_\_\_  
Advisor

\_\_\_\_\_  
Date

\_\_\_\_\_

\_\_\_\_\_  
Date

\_\_\_\_\_

\_\_\_\_\_  
Date

\_\_\_\_\_

\_\_\_\_\_  
Date

# Declaration of Authorship

I, Sudeshna Ganguly, declare that this thesis titled, 'Thesis Title' and the work presented in it are my own. I confirm that:

- This work was done wholly or mainly while in candidature for a research degree at this University.
- Where any part of this thesis has previously been submitted for a degree or any other qualification at this University or any other institution, this has been clearly stated.
- Where I have consulted the published work of others, this is always clearly attributed.
- Where I have quoted from the work of others, the source is always given. With the exception of such quotations, this thesis is entirely my own work.
- I have acknowledged all main sources of help.
- Where the thesis is based on work done by myself jointly with others, I have made clear exactly what was done by others and what I have contributed myself.

Signed:

---

Date:

---

## *Acknowledgements*

I would like to take this opportunity to convey my appreciation to my advisor Professor Giovanni Bonvicini for helping me throughout my research work and his continuous support and encouragement over last four and half years. I would like to thank our former group member Peng Zhou for teaching me all the basics of the analysis procedure and Smith Mackenzie for the discussions. I would like to thank our two other froup members Ryan Gillard and Hussein Farhat who have graduated recently, for their continuous support and friendship. Many many thanks to our Belle collaborator Anze Zupanc for replying to all my question really quick. And of course I am grateful for all the support my loving parents and my fiancs shown me throughout this entire process of getting my Ph.D, so I would like to say a big thank you to them.

# Contents

<b>Declaration of Authorship</b>	<b>i</b>
<b>Acknowledgements</b>	<b>ii</b>
<b>Contents</b>	<b>iii</b>
<b>List of Figures</b>	<b>vi</b>
<b>List of Tables</b>	<b>ix</b>
<b>1 Introduction</b>	<b>1</b>
1.1 Abstract	1
1.2 Standard Model	2
1.2.0.1 Fundamental bosons	4
1.2.0.2 Fundamental fermions	4
1.2.0.3 Symmetries	5
1.2.0.4 Standard Model Interactions	7
1.2.0.5 The Strong Force	7
1.2.0.6 The Electromagnetic Force	8
1.2.0.7 The Weak Force	8
1.2.0.8 Higgs boson	10
1.2.0.9 Standard Model operations	11
1.2.0.10 Decays: Inclusive and Exclusive	11
1.2.0.11 D ( $D_s$ ) meson	11
1.2.0.12 Idea behind this Thesis	13
<b>2 Belle Experiment</b>	<b>16</b>
2.1 Belle Experiment	16
2.1.1 KEKB Accelerator	17
2.1.2 Belle Detector	19
2.1.2.1 Beam Pipe	20
2.1.3 Silicon Vertex Detector (SVD)	20
2.1.3.1 Central Drift Chamber	21
2.1.3.2 Aerogel Cherenkov Counter (ACC)	23
2.1.3.3 Time of Flight	25

2.1.3.4	Electromagnetic Calorimeter	25
2.1.3.5	$K_L/\mu$ Detector	27
2.1.3.6	Particle identification	28
2.1.3.7	Solenoid Magnet	29
2.2	Triggering and Data Collection	29
2.2.1	Trigger system	29
2.3	Data Acquisition (DAQ)	31
2.4	Software and Simulation	31
2.4.1	Monte Carlo Simulation	32
2.4.1.1	Event Generators	32
2.4.1.2	Simulation of the Detector Response	33
<b>3</b>	<b>Experimental methods and results in Monte Carlo</b>	<b>34</b>
3.1	Outline of the analysis method	34
3.1.1	Reconstruction of the final state particles and selection criteria applied on them	35
3.1.2	$D_{tag}$ reconstruction	38
3.1.3	Primary kaon reconstruction	38
3.1.4	$X_{frag}$ reconstruction	39
3.1.5	Reconstruction of inclusive $D_s^*$ candidates	40
3.1.6	Reconstruction of Inclusive $D_s$ candidates	40
3.2	Monte Carlo samples	40
3.2.1	Signal MC samples	40
3.2.2	Generic MC samples	41
3.3	Monte Carlo background categories characterization	41
3.4	Fit to $M_0$ in Monte Carlo data.	43
3.4.1	Summary of MC analysis.	43
3.5	Reconstruction of exclusive $D_s \rightarrow \pi^0/\rho/K_s l \nu$ decays	44
3.5.1	$E_{ecl}$ , $E_\nu$ and $MM^2$	46
3.5.2	Yield determination procedure	46
3.6	$D_s \rightarrow \pi^0 l \nu$ analysis	48
3.6.1	MC analysis.	48
3.6.2	Fit procedure.	50
3.7	$D_s \rightarrow \rho l \nu$ analysis.	57
3.7.1	MC analysis.	57
3.8	$D_s \rightarrow K_s l \nu$ analysis.	67
3.8.1	MC analysis.	67
<b>4</b>	<b>Data analysis</b>	<b>76</b>
4.1	Introduction	76
4.2	Reconstruction of Inclusive $D_s$ candidates in Data	76
4.3	$D_s \rightarrow \pi^0 l \nu$ fit in Data	77
4.3.1	True branching fraction: $\mathcal{B}(\text{in data})-\mathcal{B}(\text{in MC})$	78
4.3.2	Systematic errors	79
4.4	$D_s \rightarrow \rho e \nu$ fit in Data	79
4.4.1	True branching fraction: $\mathcal{B}(\text{in data})-\mathcal{B}(\text{in MC})$	79
4.4.2	Systematic errors	80

---

4.5	$D_s \rightarrow K_s l \nu$ fit in Data . . . . .	80
4.5.1	True branching fraction: $\mathcal{B}(\text{in data})-\mathcal{B}(\text{in MC})$ . . . . .	81
4.5.2	Systematic errors . . . . .	81
<b>5</b>	<b>Conclusion</b>	<b>82</b>
<b>A</b>	<b>Appendix.</b>	<b>83</b>
	<b>Bibliography</b>	<b>88</b>

# List of Figures

1.1	Standard Model of elementary particles . . . . .	2
1.2	Standard Model of elementary particles . . . . .	3
1.3	Interaction vertex between electron and neutrino . . . . .	5
1.4	the magnitudes of the interaction between six quarks: intensity of each line is represented by the the CKM matrix element. . . . .	9
1.5	Feynman diagrams of standard $D_s$ meson decay. . . . .	12
1.6	Feynman diagram of the leptonic decays of $D_s$ meson in Standard Model. . . . .	13
1.7	Feynman diagram of the leptonic decays of $D_s$ meson in Standard Model. . . . .	14
1.8	Semi-leptonic decays of $D_s$ meson: $D_s \rightarrow \pi^0/\rho l\nu$ . . . . .	15
1.9	Semi-leptonic decays of $D_s$ meson: $D_s \rightarrow K_s l\nu$ . . . . .	15
2.1	KEKB storage rings, LER and HER, Interaction Point located in Tsukuba Experimental Hall. . . . .	17
2.2	The cross section of the beam pipe at the IP. . . . .	18
2.3	Side view of the Belle detector. . . . .	19
2.4	The cross section of the beam pipe at the IP. . . . .	20
2.5	Structure of SVD1. Top one shows an r-z view and bottom one show r- $\phi$ views. . . . .	21
2.6	Double Sided Silicon Detector. . . . .	22
2.7	The graphic view of Central Drift Chamber (CDC): left-side view; right-end view. . . . .	23
2.8	View of the cross-section of the cell structure in CDC. . . . .	23
2.9	y axis: Truncated mean of dE/dx; x axis: momentum. The points in the figure are individual tracks, the bands are the distributions of particles of each type. p is measured in GeV/c. . . . .	24
2.10	Charged particle passing through CDC. When a charged particle crosses across CDC, the atoms of the gases get ionized and cluster in the high voltage sense wires. . . . .	25
2.11	lay out of the Aerogel Cherenkov Counter (ACC). . . . .	26
2.12	Cherenkov effect and Cherenkov angle. . . . .	27
2.13	Schematic diagram of TOF and TSC. . . . .	28
2.14	Schematic diagram of the ECL. . . . .	29
2.15	Cross-section of the KLM super-layer. . . . .	30
2.16	Illustration of the Belle Level-1 Trigger system. . . . .	31
2.17	schematics of Data Acquisition (DAQ). . . . .	32
2.18	Monte Carlo. . . . .	33

3.1	Generic MC: $M_0$ distribution in sky blue for correctly reconstructed ( <code>cate1</code> ) $D_s$ events and $M_0$ distributions for five other categories (color specifications given on the plot) . . . . .	42
3.2	$M_0$ fit in $D_s \rightarrow \pi^0 l \nu$ mode. . . . .	43
3.3	$M_0$ fit in $D_s \rightarrow \rho l \nu$ mode. . . . .	44
3.4	$M_0$ fit in $D_s \rightarrow K_s l \nu$ mode. . . . .	44
3.5	First row: $D_s \rightarrow \pi^0 e \nu$ , Second row: $D_s \rightarrow \pi^0 \mu \nu$ . First column: FOM versus $E_{ecl}$ cut for nominal branching ratios as described in the text. Second column: optimized FOM as a function of the assumed branching ratio. FOM for $E_{ecl}$ , "square" and "triangular" cuts are shown. . . . .	49
3.6	$MM^2$ for $D_s \rightarrow \pi^0 l \nu$ decay, category specific color code given. . . . .	49
3.7	$E_{ecl}$ distribution for $D_s \rightarrow \pi^0 l \nu$ decay . . . . .	50
3.8	$E_\nu$ distribution for $D_s \rightarrow \pi^0 l \nu$ decay . . . . .	51
3.9	$MM^2$ vs. $E_{ecl}$ for $D_s \rightarrow \pi^0 l \nu$ decay . . . . .	52
3.10	$MM^2$ vs. $E_\nu$ for $D_s \rightarrow \pi^0 l \nu$ decay . . . . .	53
3.11	$E_\nu$ vs. $E_{ecl}$ for $D_s \rightarrow \pi^0 l \nu$ decay, Blue Markers: for the events selected with Best ( $E_{ecl}, E_\nu$ ) Selection Criteria. . . . .	54
3.12	$MM^2$ distribution for $D_s \rightarrow \pi^0 \mu \nu$ decay. Blue line: optimal ( $E_{ecl}, E_\nu$ ) cuts. Red line: no ( $E_{ecl}, E_\nu$ ) cuts. . . . .	54
3.13	$MM^2$ distribution for $D_s \rightarrow \pi^0 e \nu$ decay. Blue line: optimal ( $E_{ecl}, E_\nu$ ) cuts. Red line: no ( $E_{ecl}, E_\nu$ ) cuts . . . . .	55
3.14	<code>dsdm</code> distributions in generic MC backgrounds for $D_s \rightarrow \pi^0 \mu \nu$ . Blue line: optimal ( $E_{ecl}, E_\nu$ ) cuts. Red line: no ( $E_{ecl}, E_\nu$ ) cuts. . . . .	55
3.15	Fit to the $MM^2$ distribution in the $\pi^0 \mu \nu$ channel. . . . .	55
3.16	Fit to $MM^2$ distribution for $\pi^0 e \nu$ candidates . . . . .	56
3.17	$MM^2$ for $D_s \rightarrow \rho l \nu$ decay, category specific color code given . . . . .	57
3.18	$E_{ecl}$ distribution for $D_s \rightarrow \rho l \nu$ decay . . . . .	58
3.19	$E_\nu$ distribution for $D_s \rightarrow \rho l \nu$ decay . . . . .	59
3.20	$MM^2$ vs. $E_{ecl}$ for $D_s \rightarrow \rho l \nu$ decay. . . . .	60
3.21	$MM^2$ vs. $E_\nu$ for $D_s \rightarrow \rho l \nu$ candidates . . . . .	61
3.22	$E_\nu$ vs. $E_{ecl}$ for $D_s \rightarrow \rho l \nu$ candidates. In $D_s \rightarrow \rho \mu \nu$ mode: Blue Markers: for the events selected with Best ( $E_{ecl}, E_\nu$ ) Selection Criteria . . . . .	62
3.23	$M_{\pi^+\pi^-\pi^0}$ for $D_s \rightarrow \rho l \nu$ decay. . . . .	62
3.24	$M_{\pi^+\pi^-\gamma}$ for $D_s \rightarrow \rho l \nu$ decay. . . . .	63
3.25	$MM^2$ distribution for $D_s \rightarrow \rho \mu \nu$ decay. Blue line: optimal ( $E_{ecl}, E_\nu$ ) cuts. Red line: no ( $E_{ecl}, E_\nu$ ) cuts . . . . .	63
3.26	$MM^2$ distribution of $D_s \rightarrow \rho e \nu$ decay. no optimal ( $E_{ecl}, E_\nu$ ) cut is applied. . . . .	64
3.27	First row: $D_s \rightarrow \rho e \nu$ , Second row: $D_s \rightarrow \rho \mu \nu$ . First column: FOM versus $E_{ecl}$ cut for nominal branching ratios as described in the text. Second column: optimized FOM as a function of the assumed branching ratio. FOM for $E_{ecl}$ , "square" and "triangular" cuts are shown. . . . .	64
3.28	<code>dsdm</code> distributions for $D_s \rightarrow \rho l \nu$ candidates in Generic MC. Blue line: optimal ( $E_{ecl}, E_\nu$ ) cuts. Red line: No optimal ( $E_{ecl}, E_\nu$ ) selection. . . . .	64
3.29	generic MC: <code>dsdm</code> distribution for $D_s \rightarrow \rho \mu \nu$ , with optimal ( $E_{ecl}, E_\nu$ ) for $-0.05 < MM^2 < 0.05$ . Blue line: optimal ( $E_{ecl}, E_\nu$ ) cuts. Red line: no ( $E_{ecl}, E_\nu$ ) cuts. . . . .	65
3.30	Fit to $MM^2$ distribution, $D_s \rightarrow \rho \mu \nu$ candidates. . . . .	65
3.31	Fit to $MM^2$ distribution, $D_s \rightarrow \rho \mu \nu$ candidates. . . . .	65



3.32	Fit to $MM^2$ distribution, $D_s \rightarrow \rho e \nu$ candidates. . . . .	66
3.33	$MM^2$ for $D_s \rightarrow K_s l \nu$ decay, category specific color code given . . . . .	67
3.34	$E_{ecl}$ distribution for $D_s \rightarrow K_s l \nu$ decay . . . . .	68
3.35	$E_\nu$ distribution for $D_s \rightarrow K_s l \nu$ decay . . . . .	69
3.36	$MM^2$ vs. $E_{ecl}$ for $D_s \rightarrow K_s l \nu$ decay. . . . .	70
3.37	$MM^2$ vs. $E_\nu$ for $D_s \rightarrow K_s l \nu$ decay. . . . .	71
3.38	$E_\nu$ vs. $E_{ecl}$ for $D_s \rightarrow K_s l \nu$ candidates. In $D_s \rightarrow K_s \mu \nu$ mode: Blue Markers: for the events selected with Best ( $E_{ecl}, E_\nu$ ) Selection Criteria . . . . .	72
3.39	$MM^2$ distribution for $D_s \rightarrow K_s \mu \nu$ decay. Blue line: optimal ( $E_{ecl}, E_\nu$ ) cuts. Red line: no ( $E_{ecl}, E_\nu$ ) selection. . . . .	72
3.40	$MM^2$ distribution of $D_s \rightarrow K_s e \nu$ . No ( $E_{ecl}, E_\nu$ ) selection is applied. . . . .	73
3.41	First row: $D_s \rightarrow K_s e \nu$ , Second row: $D_s \rightarrow K_s \mu \nu$ . First column: FOM versus $E_{ecl}$ cut for nominal branching ratios as described in the text. Second column: optimized FOM as a function of the assumed branching ratio. FOM for $E_{ecl}$ , “square” and “triangular” cuts are shown. . . . .	73
3.42	Generic MC <code>dsgm</code> distributions for $D_s \rightarrow K_s l \nu$ . . . . .	74
3.43	Fit to $MM^2$ distribution for $K_s \mu \nu$ candidates. . . . .	74
3.44	Fit to $MM^2$ distribution for $K_s e \nu$ candidates. . . . .	74
3.45	Fit to $MM^2$ distribution for $K_s l \nu$ background candidates only in Generic MC . . . . .	75
4.1	Fit to $M_0$ distribution background candidates only in Generic MC . . . . .	77
4.2	Data fit to $MM^2$ for $D_s \rightarrow \pi^0 \mu \nu$ decay. The signal function is obtained from the signal MC sample, plus a background shape of a quadratic polynomial. . . . .	77
4.3	Data fit to $MM^2$ for $D_s \rightarrow \pi^0 e \nu$ decay. The signal function is obtained from the signal MC sample, plus a background shape as described in the text. . . . .	78
4.4	Data fit to $MM^2$ for $D_s \rightarrow \rho e \nu$ decay. The signal function $f_s$ is from the signal MC sample, plus a quadratic background shape. . . . .	79
4.5	Data fit to $MM^2$ for $D_s \rightarrow K_s \mu \nu$ . The signal function $f_s$ is from the signal MC sample and a quadratic background shape. . . . .	80
4.6	Data fit to $MM^2$ for $D_s \rightarrow K_s e \nu$ . The signal function $f_s$ is from the signal MC sample, plus a quadratic background shape. . . . .	81
A.1	$\pi^0 \mu \nu$ muon probability distributions, for $-0.05 < MM^2 < 0.05$ . . . . .	86
A.2	$\pi^0 e \nu$ electron probability distributions, for $-0.05 < MM^2 < 0.05$ . . . . .	87
A.3	$\rho \mu \nu$ muon probability distributions, for $-0.05 < MM^2 < 0.05$ . . . . .	87
A.4	$\rho e \nu$ electron probability distributions, for $-0.05 < MM^2 < 0.05$ . . . . .	87

# List of Tables

1.1	Standard Model: quarks . . . . .	4
1.2	Standard Model: gauge bosons . . . . .	4
1.3	Coupling constants of fundamental forces (approximately) . . . . .	7
2.1	Real Data samples . . . . .	16
2.2	KEKB accelerator . . . . .	17
2.3	Geometrical parameters of the Electromagnetic Calorimeter. . . . .	27
2.4	Solenoid magnet . . . . .	30
3.1	Ground state $D_{tag}$ decay modes used in the measurement . . . . .	39
3.2	Excited $D_{tag}$ decay modes used in the measurement . . . . .	39
3.3	Signal MC samples . . . . .	41
3.4	Best $(E_{ecl}, E_\nu)$ Selection Criteria For each sub-analysis. The third column represents the optimized efficiency for signal events, and the fourth column the optimized efficiency for background events. . . . .	46
3.5	Best figures of merit $FOM_{best}$ for a type of cut and nominal branching ratio $\mathcal{B}_i$ . . . . .	48
5.1	Final branching fractions $\mathcal{B}$ . . . . .	82

# Chapter 1

## Introduction

### 1.1 Abstract

In Particle physics a quarkonium is defined as a flavor less meson whose components are a quark and an anti-quark. Mesons which are formed by a bound state of charm quark and anti-charm quark are known as charmonium states. Charmonium states are produced by  $e^+e^-$  annihilation. Exotic charmonium states have been investigated and interpreted as 4-quark states. In theoretical QCD, a new line of research during last 30 years has produced an alternate expression of the hadron wave function through a Fock states representation. According to Fock's development a  $D_s^*$  meson consists of c quark and  $\bar{s}$  anti-quark in the ground state can be represented as  $|D_s \rangle = c_0|(c\bar{s}) \rangle + c_1|(c\bar{s}q\bar{q}) \rangle + \dots$ (ignoring states with gluons), which is known as Fock's development. This equation represents the hadron as a superposition of states of different multiplicity. The coefficients should satisfy  $\sum c_i^2 = 1$ . So the only way  $D_s$  can make up hadrons without any s quark is to have those quarks already in the initial state of  $D_s$ . Assuming they are different than the initial valence quarks of  $D_s$ . The initial valence quarks of  $D_s$  annihilate to produce a lepton pair leaving behind the spectator quarks in the final state. At CLEO, a large sample of  $e^+e^-$  annihilates to produce:  $e^+e^- \rightarrow D_s^- D_s^{*+}$  and  $e^+e^- \rightarrow D_s^+ D_s^{*-}$ ,  $D_s^{*+} \rightarrow D_s \gamma$ . The analysis starts by examining an exclusively reconstructed hadronic  $D_s$  candidate, the tag candidate and a single photon candidate. We reconstruct a  $D_s$  meson; either the primary or the secondary  $D_s$  coming from  $D_s^*$  and we call this meson a single tag. About 95% of the  $D_s^*$  states decay to  $D_s \gamma$  and about 90% of events comprising of a  $D_s$  are originated in the exclusive reaction  $e^+e^- \rightarrow D_s D_s \gamma$ . We spot the  $\gamma$  from  $D_s^*$  decay. The tag can be reconstructed in 8 different high purity hadronic modes. Everything else is coming from the other  $D_s$  in the event. Then by looking for the exclusive decay of  $D_s \rightarrow \pi^0 e \nu_e$  assuming  $\pi^0$  to be a pure two quark state

( $u\bar{u}$ ) or ( $d\bar{d}$ ), its valence quarks different from those of the  $D_s$ , we can probe the 4 quark content of a  $D_s$  meson. The final analysis is a fit to the  $(MM^2 - M_{\pi^0})$  distribution, where  $MM^2$  is the missing mass squared (peaking at zero for neutrino candidates) and  $M_{\pi^0}$  is the reconstructed  $\pi^0$  mass. At BELLE we reconstruct  $e^+e^- \rightarrow c\bar{c} \rightarrow D_{tag}KX_{frag}D_s^*$  and  $D_s^* \rightarrow D_s\gamma$ , following the methods used by the BELLE collaboration previously. The full reconstruction of  $e^+e^- \rightarrow c\bar{c}$  containing  $D_s$  meson events is done in two steps. We first reconstruct the inclusive  $D_s$  events and in the second step look for the exclusive decays of  $D_s \rightarrow \pi^0 l\nu$ ,  $D_s \rightarrow K_s l\nu$ ,  $D_s \rightarrow \rho l\nu$  to extract the branching fraction of each of these rare  $D_s$  decays. This analysis probes the 4-quark content of  $D_s$  by looking for  $D_s \rightarrow \pi^0 l\nu$  and  $D_s \rightarrow \rho l\nu$ . We also search for Cabibbo suppressed decay  $D_s \rightarrow K_s l\nu$  because both  $\pi^0$  and  $K_s$  are narrow in resonance and both  $K_s$  and  $\rho$  share the same final state as  $\pi^+\pi^-$ . At BELLE we look for the electron as well the heavy electron counterpart muon as the leptons.

## 1.2 Standard Model

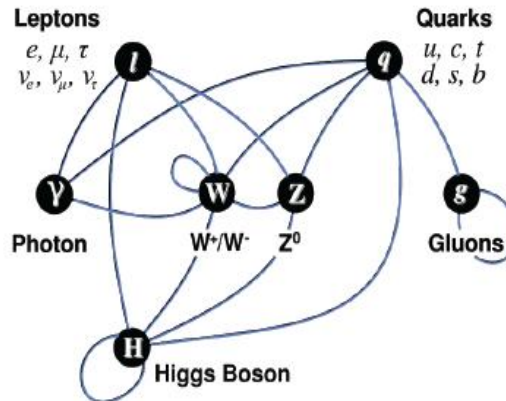


FIGURE 1.1: Standard Model of elementary particles

The Standard Model describes the behavior and construction of subatomic particles. There are three families of quarks and leptons and the gauge field quanta with which they interact. In nature there are 4 types of forces, gravitational, electromagnetic, strong and weak forces. The Standard model includes all forces except for gravity. The

constituent quarks of matter and the force carriers for the three types of interactions are shown in Figure 1. The quarks and leptons are fermions because they are spin  $1/2$  particles while the force carriers;  $\gamma$ ,  $Z^0$ ,  $W^\pm$  and gluons are bosons carrying spin 1. There are six different types of quarks carrying a “flavor” quantum numbers: up, down, charm, strange, top and bottom. The quarks are organized in three generations as follows:

$$\begin{pmatrix} u \\ d \end{pmatrix}, \begin{pmatrix} c \\ s \end{pmatrix}, \begin{pmatrix} t \\ b \end{pmatrix} \quad (1.1)$$

The “*up-type*” quarks  $u$ ,  $c$  and  $t$  have  $+\frac{2}{3}$  electric charge and the “*down-type*” quarks  $d$ ,  $s$  and  $b$  have  $-\frac{1}{3}$  electric charge. The quark mass, charge and spin have been listed in Table 1.1. Each quark flavor appear in three *colors*, commonly specified to as red, green, and blue, the naming convention being arbitrary. There are six types of leptons: the electron, muon, tau, electron neutrino, muon neutrino, and tau neutrino. They are arranged into three generations:

$$\begin{pmatrix} \nu_e \\ e \end{pmatrix}, \begin{pmatrix} \nu_\mu \\ \mu \end{pmatrix}, \begin{pmatrix} \nu_\tau \\ \tau \end{pmatrix} \quad (1.2)$$

Each of the electron, muon and tau have an electric charge  $-1$  while the neutrinos are charge-less. Fundamental bosons are gauge bosons and Higgs bosons which have integer spin.

	I	II	III	
mass →	2.4 MeV	1.27 GeV	171.2 GeV	0
charge →	$\frac{2}{3}$	$\frac{2}{3}$	$\frac{2}{3}$	0
spin →	$\frac{1}{2}$	$\frac{1}{2}$	$\frac{1}{2}$	1
name →	<b>u</b> up	<b>c</b> charm	<b>t</b> top	<b><math>\gamma</math></b> photon
Quarks	4.8 MeV $-\frac{1}{3}$ $\frac{1}{2}$ <b>d</b> down	104 MeV $-\frac{1}{3}$ $\frac{1}{2}$ <b>s</b> strange	4.2 GeV $-\frac{1}{3}$ $\frac{1}{2}$ <b>b</b> bottom	0 0 1 <b>g</b> gluon
	<2.2 eV 0 $\frac{1}{2}$ <b><math>\nu_e</math></b> electron neutrino	<0.17 MeV 0 $\frac{1}{2}$ <b><math>\nu_\mu</math></b> muon neutrino	<15.5 MeV 0 $\frac{1}{2}$ <b><math>\nu_\tau</math></b> tau neutrino	91.2 GeV 0 1 <b><math>Z^0</math></b> weak force
	0.511 MeV -1 $\frac{1}{2}$ <b>e</b> electron	105.7 MeV -1 $\frac{1}{2}$ <b><math>\mu</math></b> muon	1.777 GeV -1 $\frac{1}{2}$ <b><math>\tau</math></b> tau	80.4 GeV $\pm 1$ 1 <b><math>W^\pm</math></b> weak force
Leptons				Bosons (Forces)

FIGURE 1.2: Standard Model of elementary particles

TABLE 1.1: Standard Model: quarks

Family	Name	Charge	Mass	Spin
I	u	$+\frac{2}{3}$	1-4 MeV	$+\frac{1}{2}$
	d	$-\frac{1}{3}$	4-8 MeV	$+\frac{1}{2}$
II	c	$+\frac{2}{3}$	1.15-1.35GeV	$+\frac{1}{2}$
	s	$-\frac{1}{3}$	80 - 130MeV	$+\frac{1}{2}$
III	t	$+\frac{2}{3}$	174GeV	$+\frac{1}{2}$
	b	$-\frac{1}{3}$	4.1 - 4.4GeV	$+\frac{1}{2}$

### 1.2.0.1 Fundamental bosons

There exist two types of fundamental bosons known as gauge bosons and Higgs bosons. The photons which transmit electromagnetic interactions, W and Z bosons which transmit the weak interaction and gluons which transmit the strong interaction are the gauge bosons. The gauge bosons have spin 1. On the other hand the Higgs boson is a spin zero particle. The Higgs boson should be present in the Model to prevent assigning infinite values for some scattering amplitudes, for example the large energy scattering of  $W_L - W_L$ . The boson mass, charge and type of interaction have been listed in Table 1.2.

TABLE 1.2: Standard Model: gauge bosons

Force	Name	Charge	Mass
Electromagnetic	photon ( $\gamma$ )	0	0
Weak	$W^\pm$	$\pm 1$	80.40 GeV
	$Z^0$	0	91.188 GeV
Strong	gluons (g)	0	0

### 1.2.0.2 Fundamental fermions

Quarks, leptons and the associated neutrinos fall under the fundamental fermion group in the Standard Model. All fundamental fermions have anti-particles which have the same mass and opposite electric charge as that of the particles (neutrinos have zero electric charge). Quarks are used in the configuration of the extensive bulk of subatomic particles, known as hadrons interacting strongly with other hadrons. Only zero color quark states can be considered as meta-stable with respect to the strong interaction. There can not be any free quark because the potential energy required to disjoin the quarks in a

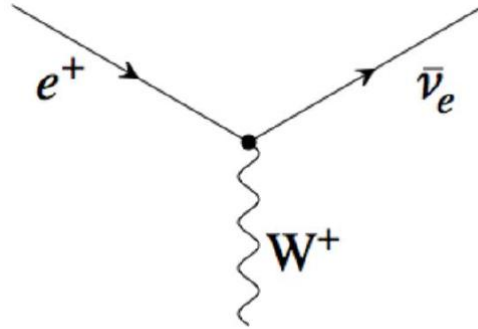


FIGURE 1.3: Interaction vertex between electron and neutrino

hadron by macroscopic distances is much greater than the rest mass energy of the quarks expressed as:  $2m_q c^2$ . The mass and charge of fundamental particles are mentioned in Fig. 1.2. A quark can transform from one generation to the other generation by emitting or absorbing a  $W^\pm$ , Fig. 1.3. The up and down quarks are lighter than others.

Hadrons are generated in two different ways: 1. by combining a quark (e.g. blue) with an anti-quark (e.g. anti-blue). So the net color is zero, and the particles formed so are known as mesons with integer spin. Mesons are comparatively less known in the day-to-day experience because even for the longest lived mesons the lifetimes are of  $\mathcal{O}(10^{-8}s)$  only. For example the wave functions of Kaons and pions are expressed as  $|u\bar{s}\rangle$  and  $|d\bar{u}\rangle$  respectively (each of the wave functions refers the quark contents). A baryon is obtained by combining three quarks (red, green and blue), having half-integer spin. Anti-baryons are produced by combining three anti-quarks. An example of a baryon is a proton which is represented as  $|uud\rangle$ .

### 1.2.0.3 Symmetries

The physical or mathematical characteristic (observed or inherent) which is conserved under alterations is known as the symmetry of a physical system. Noether's (first) theorem states that any distinguishable symmetry of the action of a physical system is associated with the conservation of a physical quantity [8]. From Noether's theorem

we get a definite description of the relation between symmetry and conservation. The theorem presents that the each of the continuous symmetry of a physical system suggests the conservation of some physical properties of that system. Conversely, each conserved quantity has a corresponding symmetry. For example, with the translation in space, the laws of physics remaining invariant, gives rise to conservation of linear momentum, and over time, when the laws of nature remains invariant, that gives rise to the conservation of energy. Although it is a discrete symmetry, parity also obeys Noether's Theorem. Parity transformation or reversal is known as the change in the sign of one or three spatial coordinates, for example

$$P : \begin{pmatrix} x \\ y \\ z \end{pmatrix} \mapsto \begin{pmatrix} -x \\ -y \\ -z \end{pmatrix}$$

Parity has only two values  $\pm 1$ . The value  $+1$  is called the even parity and the value  $-1$  is called the odd parity. A system with even parity can be conserved to a system with even parity and a system with odd parity will be conserved to a system with odd parity. Intrinsic parity of a particle makes up the wave function of the particle. The parity of a state consisting of particles a and b:  $(-1)^L P_a P_b$ , where  $L$  is the relative orbital momentum and  $P_a$  and  $P_b$  are the intrinsic parity of the two particles. The parity operator acting on a wave function gives:

$$P\psi(x, y, z) = \psi(-x, -y, -z) \quad P^2\psi(x, y, z) = P\psi(-x, -y, -z) = \psi(x, y, z) \quad (1.3)$$

The parity operator is unitary.  $P = 1$  refers to even parity and  $P = -1$  refers to odd. If a process is parity invariant then it remains the same in its mirror image. For scalars parity has a value of 1 ( $P = 1$ ) and for pseudo scalars it is  $-1$  ( $P = -1$ ). Scalars and pseudo scalars are rotationally invariant. Vectors ( $P = -1$ ) and axial vectors (also called pseudo vectors) ( $P = 1$ ) both change as vectors under rotation. Parity is conserved in electromagnetism, strong interactions and gravity, but is broken in weak interactions. The Standard Model includes parity violation in terms of the weak interaction as a chiral gauge interaction. Only the left-handed components of particles and right-handed components of antiparticles participate in weak interactions in the Standard Model. The analysis by theoretical physicists Tsung Dao Lee and Chen Ning Yang probed that although parity conservation had been verified in the strong or electromagnetic



interactions, it was not tested in the weak interaction. C. S. Wu, E. Ambler, R. W. Hayward, D. D. Hoppes, and R. P. Hudson, in 1957 discovered an explicit parity violation in the beta decay of cobalt-60 [11]. In 2010, it was announced that the physicists who were working with the Relativistic Heavy Ion Collider (RHIC) had generated a short-lived parity symmetry-breaking bubble in quark-gluon plasmas. An experiment performed by various physicists from the STAR collaboration, proposed that parity can also be broken in the strong interaction [12].

#### 1.2.0.4 Standard Model Interactions

The three interactions integrated into the SM are, in order of decreasing strength, the strong force, the electromagnetic force, and the weak force. Each of the forces have a specific coupling constant which are shown in Table 1.3. These forces are natural results of the application of a gauge-symmetry into the quantum theoretical framework of the SM.

Force	Coupling constant	Values
Strong	$\alpha_s$	$\leq 1$
Electromagnetic	$\alpha = \frac{e^2}{4\pi\hbar c}$	$\approx \frac{1}{137} = 7.3 \times 10^{-3}$
Weak	$\frac{G(Mc^2)^2}{(\hbar c)^3}$	$1.17 \times 10^{-5}$
Gravity	$\frac{G_N M^2}{4\pi\hbar c}$	$5 \times 10^{-40}$

TABLE 1.3: Coupling constants of fundamental forces (approximately) [3]

#### 1.2.0.5 The Strong Force

Eight gauge bosons known as the gluons transmit the strong force. The gluons are massless and they pair only with those particles with color charge (i.e., with the quarks and other gluons). Quantum chromodynamics (QCD) explains the strong interaction, and is based on the symmetry group SU(3). From Table 1.3, the coupling constant for the strong force is shown to be a large number compared to the electromagnetic and weak forces. Due to this large coupling constant some difficulties may arise in the theoretical calculations dependent on perturbation theory. QCD is a non-Abelian gauge theory and it states that only quarks and gluons can take part in strong interaction by carrying color charges. The strong interaction holds nuclei together and it requires that the hadronic states be colorless. QCD has Asymptotic freedom [1], [2]. The strong interaction coupling constant decreases at short distances.

### 1.2.0.6 The Electromagnetic Force

A single massless gauge boson known as photon transfer the electromagnetic force. Photons interact with particles with electric charge: the quarks, the electron, muon, and tau leptons, and the  $W^+$  and  $W^-$ . The field theory which describes the interaction of the photon with charged particles is called quantum electrodynamics (QED), and is based on the  $U(1)$  symmetry group.

### 1.2.0.7 The Weak Force

Three gauge bosons, the  $W^+$ , the  $W^-$ , and the  $Z^0$  carry the weak force. The weak force is the weakest of the three forces in the Standard Model. Only weak force can change the flavor of a lepton or quark. For example, radio active decay of the neutron is caused by the weak interaction:

$$n \rightarrow pe\bar{\nu}_e \quad (1.4)$$

In this process the flavor of one of the neutrons constituent quarks changes from down to up quark:

$$d \rightarrow ue\bar{\nu}_e \quad (1.5)$$

All fundamental fermions are coupled by the weak forces and only weak force can couple to the neutrinos, which makes the neutrinos very distinct in character and infamously difficult to detect by experiments. The combined description of the electromagnetic and weak forces is called the electroweak theory, or the Glashow, Weinberg, and Salam (GSW) theory [4], [5], [6], and it is based on a broken  $SU(2) \times U(1)$  symmetry. The weak force couples the up-type quarks to the down-type quarks via the W boson. Different from the gauge bosons from the electromagnetic and strong forces, the W and Z bosons gain masses of order  $100 \text{ MeV}/c^2$  via the Higgs mechanism. In 1963 Cabibbo [9] postulated that the weak interaction transitions for quarks could be explained same as the weak interaction transitions for electrons and neutrinos, the only difference being an additional factor  $\cos \theta_C$  in the amplitude for particles with a d to u interaction and  $\sin \theta_C$  for particles with a s to u quark interaction. The angle  $\theta_C$  is called the Cabibbo angle and is about  $13.1^\circ$ . The magnitudes of the weak interaction between six quarks are shown in Fig. 1.4.

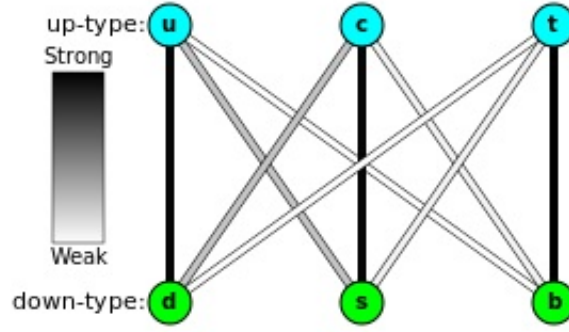


FIGURE 1.4: the magnitudes of the interaction between six quarks: intensity of each line is represented by the the CKM matrix element.

The eigenstates of quarks of the weak interaction are related to the mass eigenstates of the quarks by a matrix transformation.

$$\begin{pmatrix} d' \\ s' \\ b' \end{pmatrix} = \begin{pmatrix} V_{ud}V_{us}V_{ub} \\ V_{cd}V_{cs}V_{cb} \\ V_{td}V_{ts}V_{tb} \end{pmatrix} \begin{pmatrix} d \\ s \\ b \end{pmatrix} \quad (1.6)$$

This matrix  $V$  is known as the Cabibbo, Kobayashi, and Maskawa (CKM) matrix. The standard parameterization [10]

$$V_{CKM} = \begin{pmatrix} c_{12}c_{13}s_{12}c_{13}s_{13}e^{i\delta} \\ -s_{12}c_{23} - c_{12}s_{23}s_{13}e^{i\delta} & c_{12}c_{23} - s_{13}s_{23}s_{13}e^{i\delta} & s_{23}c_{13} \\ s_{12}s_{23} - c_{12}c_{23}s_{13}e^{i\delta} & -s_{23}c_{12} & -s_{12}c_{23}s_{13}e^{i\delta} & c_{23}c_{13} \end{pmatrix} \quad (1.7)$$

here  $s_{ij} = \sin \theta_{ij}$  and  $c_{ij} = \cos \theta_{ij}$  where  $i, j = 1, 2, 3$  representing the three Euler angles.  $\delta$  is a CP violating phase. These  $c_{ij}$  and  $s_{ij}$  can be positive and  $\delta$  ranges between 0 and  $2\pi$ . Quark-quark interactions that proceed through a larger amplitude  $\cos \theta_C$  are known as Cabibbo favored interactions. Those quark-quark interactions advancing through the smaller amplitude  $\sin \theta_C$  are known as the Cabibbo suppressed interactions. The experimental magnitudes of the CKM matrix elements are established to be:

$$\begin{pmatrix} |V_{ud}| \approx 0.974 & |V_{us}| \approx 0.225 & |V_{ub}| \approx 0.004 \\ |V_{cd}| \approx 0.225 & |V_{cs}| \approx 0.973 & |V_{cb}| \approx 0.041 \\ |V_{td}| \approx 0.009 & |V_{ts}| \approx 0.041 & |V_{tb}| \approx 0.999 \end{pmatrix} \quad (1.8)$$

These values of the components of the CKM matrix have been obtained by incorporating various experimental observations and those observations have been listed in [7]. These values show that the conversions within a family of quarks (i.e.,  $t \rightarrow b$ ,  $c \rightarrow s$ ,  $d \rightarrow u$ ) are preferred over transitions between two different families. In summary the CKM matrix:  $V_{CKM}$  is a  $3 \times 3$  complex matrix with, in principle, nine magnitudes and nine irreducible phases. The matrix must be unitary to conserve probability;  $V_{CKM}V_{CKM}^\dagger = I$ , so it gives the following equation:

$$\sum_i V_{ij}V_{ik}^* = \delta_{jk} \quad (1.9)$$

The matrix elements of  $V_{CKM}$  are complex generally and the unitarity requirements for different rows ( $j \neq k$ ) are demonstrated as triangles in the complex plane. The relation that describes a Unitary triangle is given as follows:

$$V_{ud}V_{ub}^* + V_{cd}V_{cb}^* + V_{td}V_{tb}^* = 0 \quad (1.10)$$

For convenience, we normalize one of the sides by dividing the relation in Equation. 1.10. The unitarity of the CKM matrix reduces the degrees of freedom to three rotation angles and six complex phases. Five of these phases can be assimilated in re-conceiving the quark fields. That leaves one essential complex phase. So a CKM matrix is essentially expressed in terms of three angles and one phase. The complex phase has observable consequences of violating the CP-symmetry. This is a violation of symmetry obtained by applying first the charge (electron to positron) then the parity (spin up to spin down) operations.

In 1973, Kobayashi and Maskawa (KM) suggested that CP violation takes place when there are three or more than three families of quarks present, even though by then only two families of quarks were discovered. After the experimental discovery of the third quark family it confirmed the postulate of KM mechanism of CP violation and in 2008 they received the Nobel prize in Physics.

### 1.2.0.8 Higgs boson

The elementary particles in the Standard Model can gain mass by getting coupled with the Higgs fields, after the spontaneous symmetry breaking (SSB). The Higgs particle is the only remaining unobserved particle in the SM which has just been discovered on July 4, 2012. The existence of the Higgs field would explain the reason of some elementary particles having mass while the symmetries governing their interactions demand them

to be massless, and the reason of the weak force having a shorter range compared to the electromagnetic force. The particulars of the Higgs mechanism are beyond the scope of this Thesis, because Higgs mechanism is not essential to investigate the  $D_s$  meson decays of our interest.

### 1.2.0.9 Standard Model operations

We have so far discussed the fundamental fields and interactions included in the Standard Model. We are now going to discuss about the Standard Model Lagrangian density. The interaction of particles are described by a Lagrangian:

$$L_{int} = \int (L_{int} + L_{int}^\dagger) d^3x \quad (1.11)$$

Here  $L_{int}$  and  $L_{int}^\dagger$  are the Lagrangian density and Hermitian conjugate [3]. For a particular process, the interaction Lagrangian connects initial and final states  $i$  and  $f$  and represents the matrix element,  $M_{if}$ :

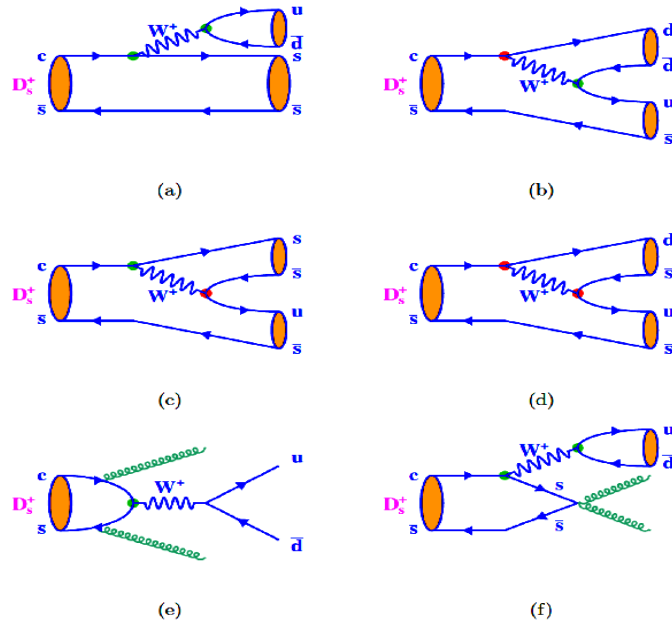
$$M_{if} = \langle f | (L_{int} + L_{int}^\dagger) | i \rangle + \frac{(-i)^2}{2!} \int d^4x \langle f | ((L_{int} + L_{int}^\dagger))^2 | i \rangle + \dots \quad (1.12)$$

### 1.2.0.10 Decays: Inclusive and Exclusive

The interactions involving quarks as illustrated in the Standard Model are not precisely detectable in nature. The theoretical calculations of the rates of exclusive decays of mesons are very hard to calculate because of the substantial uncertainties due to fundamental dynamics of the hadrons. Nevertheless, we can search for these decays experimentally with a comparably good accuracy, as they go through a specific primary and a final state. But theoretical uncertainties can be reduced by restricting the calculations of the processes to the quark level. So all possible comprehensions of an inclusive process must be measured to compare such a theoretical conjecture to experiment.

### 1.2.0.11 D ( $D_s$ ) meson

The  $J/\psi$  meson is a subatomic particle and a flavor-neutral meson which is made up of a charm quark and an anti-charm quark. Mesons which are created by a bound state of a charm and a anti-charm quark are known as charmonium. The  $J/\psi$  is the first excited state of charmonium (i.e. charmonium state with the second-lowest rest mass). The  $J/\psi$  has a rest mass of  $3.0969 \text{ GeV}/c^2$ , and a mean lifetime of  $7.2 \times 10^{-21}$

FIGURE 1.5: Feynman diagrams of standard  $D_s$  meson decay.

s. Two independent research groups found out the existence of  $J/\psi$ , one group from the Stanford Linear Accelerator Center [13] and the second at the Brookhaven National Laboratory at MIT [14]. Both the discoveries were announced on 11 November 1974. With this discovery, there opened a new field of the charm spectroscopy, where new hadrons corresponding to the charmonium states can be generated using the quarks of lower mass. The D mesons are the charmed mesons which are the lowest mass particles containing charm quarks. where a  $D^+$  contains a  $c$  quark and a  $\bar{u}$  anti-quark, a  $D^0$  contains  $\bar{c}$  and  $u$ , and  $D^-$  contains  $\bar{c}$  and  $d$ . The  $D_s$  meson contains a  $c$  quark and a  $\bar{s}$  anti-quark. Fig. 1.5 represents the standard Feynman diagrams of a  $D_s$  decaying as a(a) Cabibbo-favored decay, (b) and (c): Cabibbo-suppressed decay, (d): double Cabibbo-suppressed decay and (e) and (f): annihilation decay. The D mesons have a rest lifetime of order 1psec. They fly over a distance of about hundreds of microns to centimetres from the interaction point before they decay through the weak interaction at higher energy accelerators. It is possible to detect those secondary sources of particles or the detached vertex points by means of vertex detectors. D mesons have various excited states with higher orbital quantum number and higher mass. The excited D mesons just above the ground states are  $D^{*0}$ ,  $D^{*\pm}$ ,  $D_s^*$  respectively. These excited states have spin one and decay to the ground state releasing a pion or photon. Charmed D and  $D_s$  mesons leptonic and semi-leptonic decay take place in terms of a charged W-boson interchange, and we can study the  $c \rightarrow d$  and  $c \rightarrow s$  quark flavour-changing conversions. With the experimental measurements of the branching fractions of the charmed D and

$D_s$  mesons (integrated with theoretical calculations of the hadron matrix elements), we can find the CKM matrix elements  $|V_{cd}|$  and  $|V_{cs}|$  (in the Standard Model) and we can study the unitarity of the second row of the CKM matrix.

### 1.2.0.12 Idea behind this Thesis

The leptonic decay of  $D_s$  meson follows as Fig. 1.6.

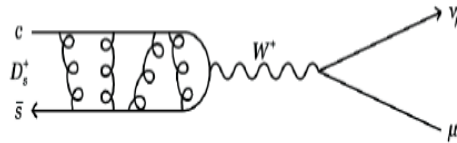


FIGURE 1.6: Feynman diagram of the leptonic decays of  $D_s$  meson in Standard Model.

According to Standard Model, only hadron that can be generated in the final state of the  $D_s$  decay will consist of s and a  $\bar{s}$  quarks, because c decays to s quark 95% of the time (Cabibbo favored) as shown in Fig. 1.7. So there will be no way that a hadron without any strangeness can be obtained as the daughter of a  $D_s$  decay. Brodsky and collaborators had introduced another expression of the hadron wave function [15], [16]. If we disregard states which carry a gluon, for examples  $|\bar{c}sg\rangle$  and  $|\bar{c}sq\bar{q}\rangle$ , Fock's development states that a  $D_s^*$  meson consisting of c quark and  $\bar{s}$  quark in the ground state can be stated as

$$|D_s\rangle = c_0|(c\bar{s})\rangle + c_1|(c\bar{s}q\bar{q})\rangle + \dots \quad (1.13)$$

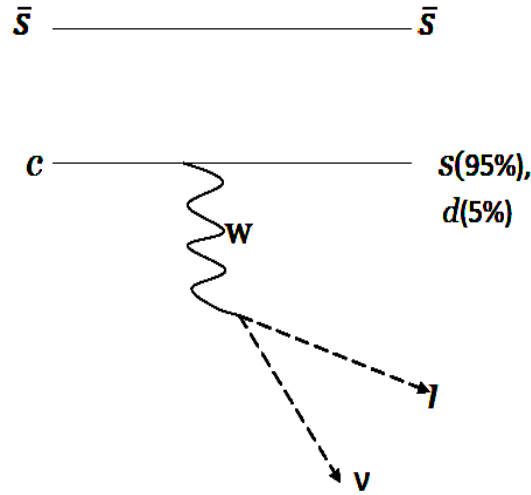


FIGURE 1.7: Feynman diagram of the leptonic decays of  $D_s$  meson in Standard Model.

The coefficients should satisfy  $\sum c_i^2 = 1$ . The physical explanation of the Fock's development is that a hadron is a superposition of states of different multiplicity. This presentation of hadron wave functions have a larger number of degrees of freedom and hence can afford an expanding body of exotic QCD phenomena. After the findings of new charmonium states [17], [18], [19], [20], Fock's development has gained extensive confirmation. Some other models as "Hadron molecule" or pure 4-quark states [21], [22], [23], [24], [25], [26], [27], [28], [29] are also being followed. So if we believe in Fock's development, we can get a  $\pi^0$  or a  $\rho$  meson as the final state of a  $D_s$  decay as shown in Fig. 1.8. Therefore looking for a  $D_s \rightarrow \pi^0/\rho l\nu$  decay can probe the 4-quark content of  $D_s$ , actually the component  $c_1$  in Eqn. 1.2.0.12.

At Cleo-c, we look for the exclusive decay of  $D_s \rightarrow \pi^0 e\nu$  assuming  $\pi^0$  to be a pure two quark state  $u\bar{u}$  or  $d\bar{d}$ , its valence quarks different from those of the  $D_s$ . At CLEO, we only look for electron as the lepton candidate, because cosmic ray (high energy muons) hampers the analysis of electron-positron collisions at CLEO and these high energy muons (cosmic rays) are considered as backgrounds. At BELLE, we look for a  $D_s \rightarrow \pi^0/\rho l\nu$  decay using data collected at the KEKB asymmetric-energy  $e^+e^-$  collider operating near  $\Upsilon(4S)$  and  $\Upsilon(5S)$  resonances

At BELLE, we also search for a  $D_s \rightarrow K_s l\nu$  as shown in Fig. 1.9, because it is a Cabibbo suppressed decay and it shares the same final state as  $\rho l\nu$  and both  $\pi^0$  and  $K_s$  have narrow resonances.



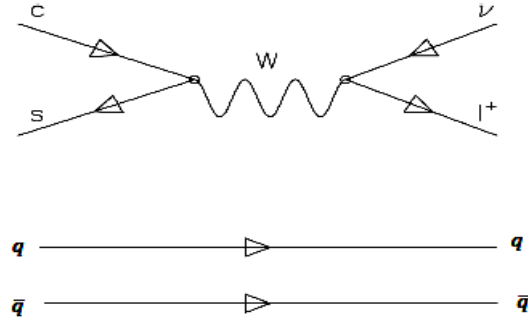


FIGURE 1.8: Semi-leptonic decays of  $D_s$  meson:  $D_s \rightarrow \pi^0 / \rho l \nu$ .

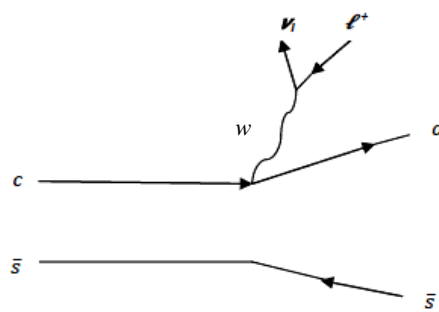


FIGURE 1.9: Semi-leptonic decays of  $D_s$  meson:  $D_s \rightarrow K_s l \nu$ .

## Chapter 2

# Belle Experiment

### 2.1 Belle Experiment

This analysis uses the data collected at the KEKB asymmetric energy  $e^+e^-$  collider, the total luminosity of the data samples used in the analysis is  $913 \text{ fb}^{-1}$  as shown in Table 2.1. Two inner detector configurations have been used; a beam pipe of diameter 2.00 cm and a silicon vertex detector with 3 layers were used for the first sample of luminosity  $\sim 156 \text{ fb}^{-1}$ , and a beam pipe of a diameter of 1.5 cm and a 4-layer silicon vertex detector and a small-cell inner drift chamber were used to document the remaining data sample of luminosity  $\sim 757 \text{ fb}^{-1}$ .

TABLE 2.1: Real Data samples

sample	$\Upsilon(4S)$	$\Upsilon(4S)$ -Off	$\Upsilon(5S)$	Total
Luminosity( $\text{fb}^{-1}$ )	<b>702.623</b>	<b>89.434</b>	<b>121.061</b>	913.318

The initial objective of the Belle experiment is to discover CP violation in the decays of B meson and analyse the CKM model of CP violation. Studies of CP violation and rare B meson decays require a data sample of many millions of B mesons. The B mesons are generated in collisions of electrons and positrons at KEKB, at the center-of-mass energy of the  $\Upsilon(4S)$  resonance. The  $\Upsilon(4S)$  resonance can be represented as a vector meson  $b\bar{b}$  state.

### 2.1.1 KEKB Accelerator

The KEKB is a particle accelerator which collides electron and positron beams with high luminosity. The design of KEKB is presented in Fig. 2.1.

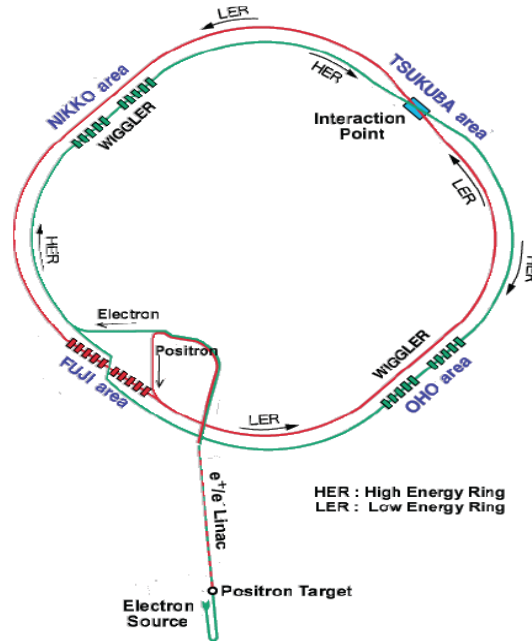


FIGURE 2.1: KEKB storage rings, LER and HER, Interaction Point located in Tsukuba Experimental Hall.

The KEKB  $e^+e^-$  collider is based on two independent rings, one for electron (8 GeV) and another for positron (3.5 GeV) located in a tunnel of a circumference of about 3 km. The relevant parameters of the KEKB accelerator are in Table 2.2.

TABLE 2.2: KEKB accelerator

Circumference of the Ring	3 Km
RF frequency	508 MHz
Energy of the electron beam	8 GeV
Energy of the positron beam	3.5 GeV
Luminosity	$10^{34} \text{ cm}^{-2} \text{ s}^{-1}$

An electron gun produces the electron beam, which gets accelerated inside a LINAC (Linear Accelerator) and when the electron beam achieves a centre of mass energy of 8 GeV, it gets injected into the HER (High Energy Ring). The positron beam of energy of 3.5 GeV gets accelerated inside the LINAC and then is gets injected into the LER

(Lower Energy Ring). The two rings cross each other at the IP (Interaction Point) where the two beams collide. The Interaction Point is situated in Tsukuba Experimental Hall.

At the Interaction Point when the electron and the positron beams collide with each other, they produce physics processes as tau, muon, quark pair production, events with two photons, Bhabha scattering processes etc. The rate of production  $R$  is defined as

$$R = \sigma \mathcal{L} \quad (2.1)$$

Here,  $\sigma$  is the cross section for a particular process and  $\mathcal{L}$  is the luminosity. At the  $\Upsilon(4S)$  resonance, with center-of-mass energy of 10.58 GeV, the interaction cross section can be estimated from Fig. 2.2.

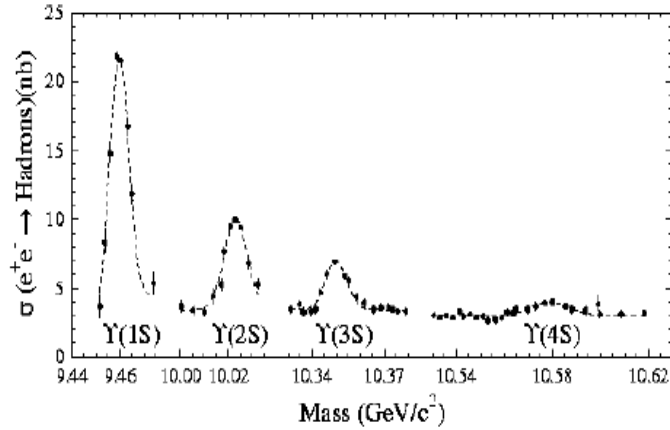


FIGURE 2.2: The cross section of the beam pipe at the IP.

$$\sigma(e^+e^- \rightarrow \Upsilon(4S)) = 1.1nb \quad (2.2)$$

Luminosity is an accelerator parameter. For collinear, equal beams it can be expressed as:

$$\mathcal{L} = fn \frac{N_1 N_2}{A} \quad (2.3)$$

here  $n$  is the number of bunches,  $N_1$  and  $N_2$  are the particle population in each beam,  $f$  is the revolution frequency, and  $A$  is the overlapping beam transverse area. A maximum luminosity of  $2.11 \times 10^{34} \text{ cm}^2 \text{ s}^{-1}$  has been obtained, which is the current highest luminosity in the world. The integrated luminosity has dimension of inverse cross section

and is defined as:

$$\mathcal{L}_{int} = \int \mathcal{L} dt \quad (2.4)$$

### 2.1.2 Belle Detector

The Belle detector is a large solid angle magnetic spectrometer [?]. It is contained within a 1.5 T superconductor solenoid and iron return yoke, and it surrounds the KEKB IP. The detector is slightly asymmetric due to the asymmetry in the beam energies. It covers about 97 % of the total solid angle and the detector schematic is depicted in Fig. 2.11. The coordinate system is defined as follows: the origin of the coordinate

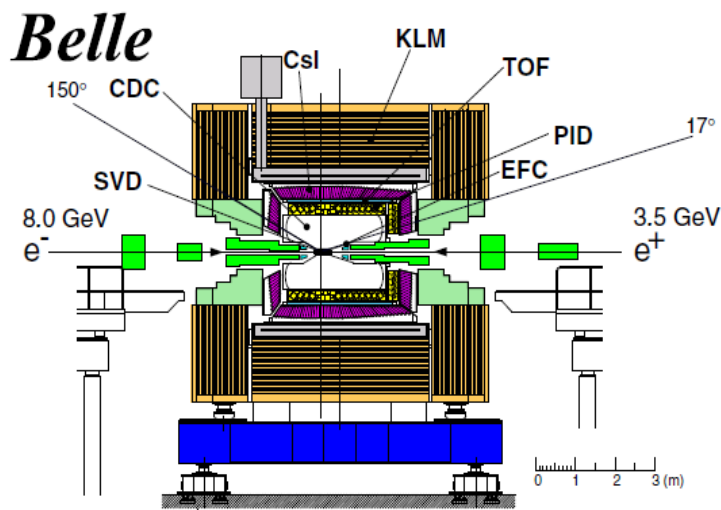


FIGURE 2.3: Side view of the Belle detector.

system lies at the IP. The  $z$  axis passes along the direction of the electron beam and also coincides with the direction of the magnetic field inside the solenoid. The  $x$  and  $y$  axes are along the horizontal and vertical direction respectively. The polar angle  $\theta$  is measured with respect to the positive  $z$  axis. The azimuthal angle  $\phi$  is defined in the  $x$ - $y$  plane and is measured with respect to the positive  $x$  axis. In the cylindrical coordinate system, the radius  $r$  is expressed as:

$$r = \sqrt{x^2 + y^2}. \quad (2.5)$$

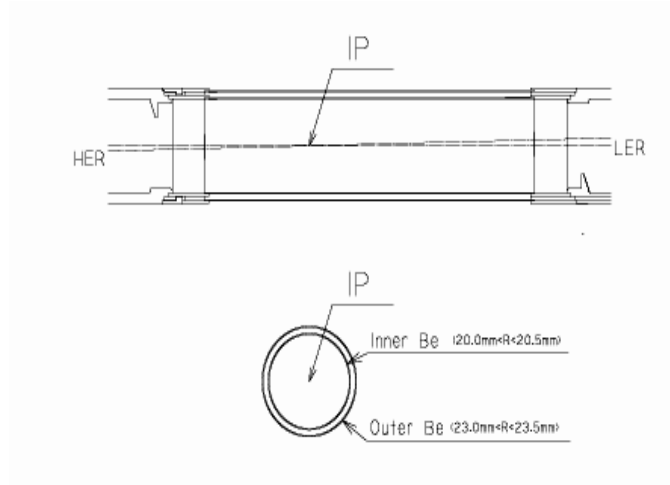


FIGURE 2.4: The cross section of the beam pipe at the IP.

### 2.1.2.1 Beam Pipe

The beam pipe encases the interaction point and inside the beam pipe the accelerator vacuum is preserved. The decay vertices can be determined very accurately by placing the Silicon Vertex Detector (SVD) as close to the IP as possible. Due to the heating of the beam pipe and the high backgrounds coming from the hits by multiple Coulomb scattering on the wall of the beam pipe, the SVD needs to be detached from the Beam Pipe. To dissipate heat, there is a double-wall beryllium cylinder in the central part ( $-4.6 \text{ cm} \leq z \leq 10.1 \text{ cm}$ ) of the beam pipe. Helium gas flows in the gap between the inner and outer walls of the beam pipe and provides cooling and the low  $Z$  of Helium decreases Coulomb interactions. The cross section of the beam pipe is shown in Fig. 2.4.

### 2.1.3 Silicon Vertex Detector (SVD)

A silicon vertex detector (SVD) measures the B-meson decay vertices and the SVD is placed right in the exterior of the beam pipe. Its center is located, with respect to the interaction point (IP), about 1.5 cm along the beam direction ( $z$  axis) and less than 0.5 cm in the transverse ( $r$ - $\phi$ ) plane [?] outside of the Beam Pipe.

SVD consists of three layers of double sided strip detectors (DSSD). These DSSDs can detect particles while the particles pass through them, by detecting the accumulated

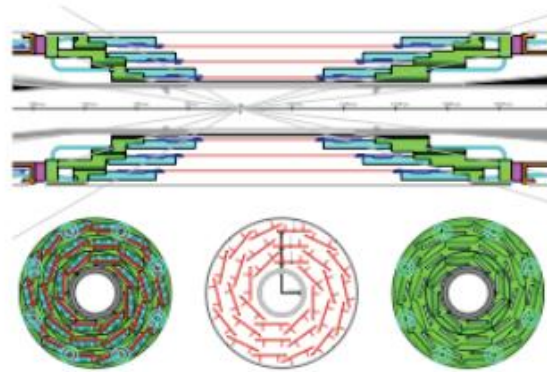


FIGURE 2.5: Structure of SVD1. Top one shows an  $r$ - $z$  view and bottom one show  $r$ - $\phi$  views.

charge on both sides of DSSD. The SVD uses S6936 type DSSDs, constructed by Hamamatsu Photonics. The DSSD is a pn junction semiconductor powered with reverse bias so that it can reach full depletion. A charged particle which passes through a p-n junction frees electrons from the valence band into the conduction band. This process creates electron-hole pairs. A current starts flowing as a result of the electron-hole pairs in the  $p^+$  and  $n^+$  strips along the surface on opposing sides of the DSSD. The DSSD is illustrated in Fig. 2.6.

### 2.1.3.1 Central Drift Chamber

The Central Drift Chamber (CDC) [31] is located outside the SVD and the CDC can measure the charged particle trajectory and momenta in three dimensions. The CDC consists of 50 layers of wire drift chamber. Particle identification is done in the CDC by measuring the specific energy loss, or  $dE/dx$ .

Fig. 2.7 illustrates the view of the CDC detector from the side and from the beam axis. The CDC ranges from 77 mm to 880 mm radially. It contains 32 axial layers, 18 small angle stereo layers and 3 cathode strip layers. The measurements in the  $r$ - $\phi$  plane is done by the axial layers of the CDC and the measurements in  $z$  direction is measured by the axial layers in combination with the stereo layers. The CDC has 8400 drift cells and each

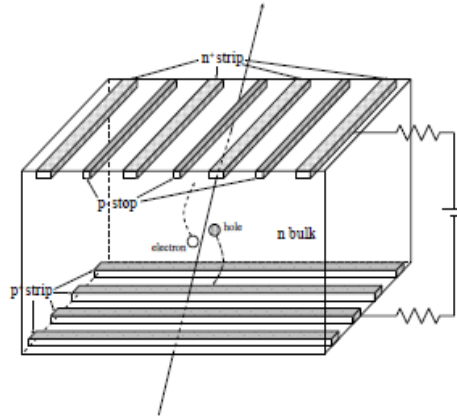


FIGURE 2.6: Double Sided Silicon Detector.

drift cell encloses one positively biased sense wire surrounded by six negatively biased field wires strung along the direction of the sense wire. The gas mixture is helium-ethane in the ratio of 1:1 by volume.

Drift chambers work as follows. A charged particle moves through the cell and ionizes the gas along its path. The anode attracts the ionized electrons and the cathode attracts the positive ions. When the electrons drift near the high electromagnetic field near the wire, they initiate more ionization and as a result an electron avalanche strikes the wire. When the sense wire gets the avalanches, an induced current flows through the sense wires. When the signal produced by the current is more than the threshold a CDC hit is detected.

A track segment finder classifies these hits into spatially related strings, or “tracks”. The trajectory of a charged particle in a constant magnetic field can be described by a helix. Such helices are fitted to the tracks to obtain the helix parameters. These helix parameters combined with the magnitude of the magnetic field gives momentum of the charged particles. The transverse momentum resolution, measured with respect to the beam axis, using cosmic ray data can be written as,

$$\frac{\sigma_{P_T}}{P_T} = \sqrt{(0.20P_T)^2 + (0.29/\beta)^2}\%, \quad (2.6)$$

Here  $P_T$  is the transverse momentum of the charged particles in GeV/c and  $\beta = \frac{v}{c}$ .



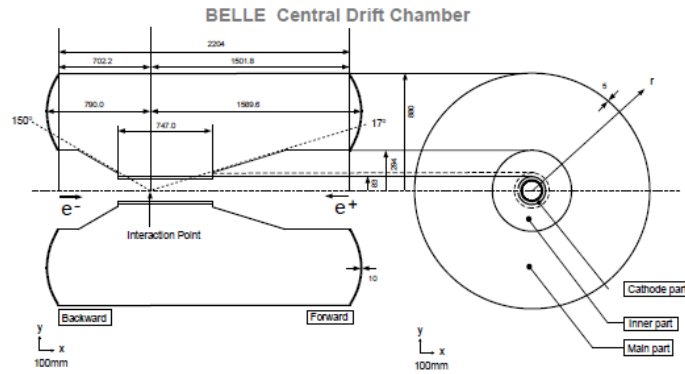


FIGURE 2.7: The graphic view of Central Drift Chamber (CDC): left-side view; right-end view.

FIGURE 2.8: View of the cross-section of the cell structure in CDC.

Inside a drift cell, the energy loss of the charged particles  $dE/dx$  can be calculated from the pulse height associated with the hit.  $dE/dx$  is a function of the velocity of the particle for a given particle momentum. The distribution of  $dE/dx$  varies for different particles as shown in fig. 2.9. For each hit in the CDC we calculate  $dE/dx$  along the path of the charged particles and we calculate a truncated mean for several such measurements. A truncated mean is defined as  $\langle dE/dx \rangle$  for a track, when the highest 20% of pulse heights is discarded. Truncation helps minimize the variance of the measurement. The combined measurement of  $dE/dx$  and momentum allows for particle identification.

### 2.1.3.2 Aerogel Cherenkov Counter (ACC)

An array of aerogel threshold Cherenkov counters (ACC) are placed radially outside the CDC. If a particle velocity  $v$  is greater than the speed of light in a medium then the charged particle emits a characteristic electromagnetic radiation known as the Cherenkov radiation [32], [33]. If the medium has an index of refraction  $n$ , then the speed of light in the medium can be written as:

$$v = \frac{c}{n} \quad (2.7)$$

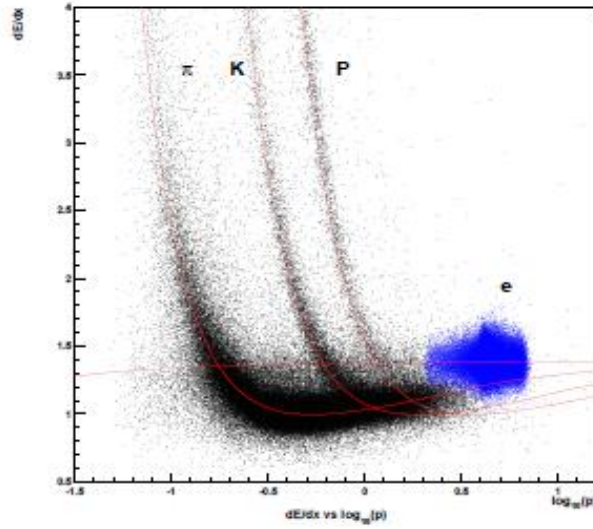


FIGURE 2.9: y axis: Truncated mean of  $dE/dx$ ; x axis: momentum. The points in the figure are individual tracks, the bands are the distributions of particles of each type.  $p$  is measured in  $\text{GeV}/c$ .

where  $c$  is the speed of light in the vacuum. Cherenkov radiation is emitted when the charged particle exceeds that speed. As the particle passes, it polarises the atoms of the medium while passing through it. The atoms in turn become electric dipoles. An electromagnetic radiation is started when the dipole field changes with time. So long as the speed of the charged particle in the medium  $v < \frac{c}{n}$  the dipoles are positioned symmetrically around the path of the particle. So when we integrate the dipole field over all dipoles, the integration produces a zero and the radiation vanishes (Fig. 2.12).

But for particles moving with  $v > \frac{c}{n}$ , there is no symmetry of the dipoles around the direction of the particle movement, as a result there is a non-zero dipole moment after integrating over all dipoles which results in a Cherenkov radiation. Fig. 2.12 demonstrates the difference in the particle polarisations for the cases of  $v > \frac{c}{n}$  and  $v < \frac{c}{n}$  [34, 35]. Then an electromagnetic shock wave is created known as the Cherenkov radiation, the ACC detects. ACC can differentiate between kaons and pions when the momentum of those charged particles vary between  $1.5\text{GeV}$   $3.5\text{GeV}$ , which is a momentum range where  $dE/dx$  does not differentiate between particles (Fig. 2.9).

Aerogel can not detect charged kaons with momentum less than  $3.5\text{ GeV}$ . On the other hand pions can generate Cherenkov radiation in an ACC with refractive index between  $1.01$  and  $1.03$ . In an ACC system there are  $5$  aerogel cubic tiles with size  $12\text{ cm}$ . There

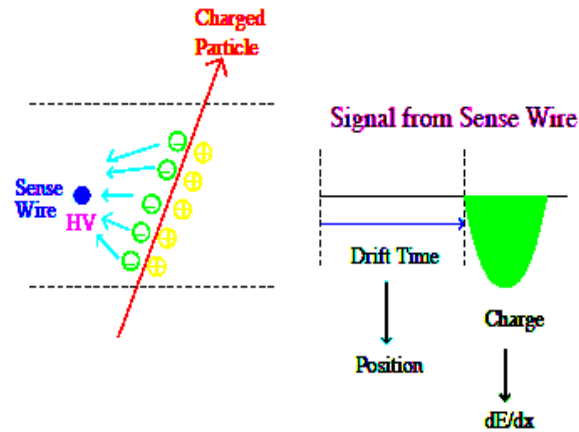


FIGURE 2.10: Charged particle passing through CDC. When a charged particle crosses across CDC, the atoms of the gases get ionized and cluster in the high voltage sense wires.

are 960 ACCs in the barrel region and 228 ACCs in the end-cap of the detector. Fine-mesh photomultiplier (FM-PMT) detect Cherenkov light in a strong magnetic field of 1.5 T.

### 2.1.3.3 Time of Flight

Time of flight counters (TOF) are placed radially outside the CDC. A TOF system contains two TOF counters and one Trigger Scintillation Counter (TSC). There are 128 TOF counters at both ends of the detector and 68 TSC counters at the backward end of the detector. The TOF spans over a region of about  $33^\circ < \theta < 121^\circ$ . The transverse momentum of the charged particles must be greater than 0.28 GeV/c in order for it to be detected by the TOF.

### 2.1.3.4 Electromagnetic Calorimeter

There is an electromagnetic calorimeter (ECL) [36] which consists of thallium-doped caesium-iodide crystal counters and this calorimeter detects electromagnetic showers.

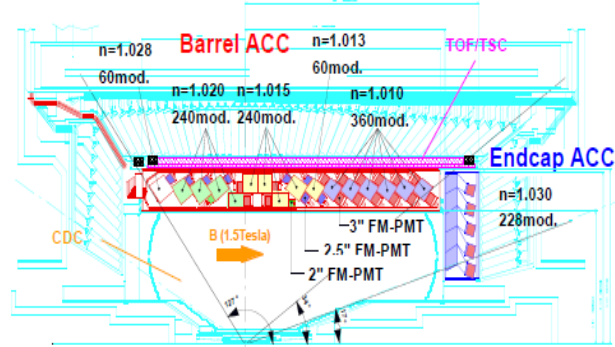


FIGURE 2.11: lay out of the Aerogel Cherenkov Counter (ACC).

The Electromagnetic Calorimeter (ECL) determines the energies of photons and electrons generated in the Belle detector. The ECL is essential to identify the electrons and to detect photons.

The ECL has fine-grained segmentation which provides high resolution of two close photons to detect high momentum  $\pi^0$  and to determine the opening angle between two photons coming from the decay  $\pi^0 \rightarrow \gamma\gamma$ . The ECL contains 8736 cesium iodide crystals. The excitation light generated by ionizing radiation is shifted to the visible spectra by thallium and the is detected by a pair of PIN photodiodes at the back end of each crystal.

Each crystal has three sections: the barrel, the backward end-cap, the forward end-cap. The ECL barrel is 3.0 m long and has an inner radius of 1.25 m and covers the polar angle between  $32^\circ \leq \theta \leq 128.7^\circ$ . The forward end cap section is located at  $z = 2.0$  m and covers  $12^\circ \leq \theta \leq 31.4^\circ$  and the backward end-cap region is located at  $z = -1.0$  m and spans over the region  $7^\circ \leq \theta \leq 155.7^\circ$  as shown in Fig. 2.14. The geometrical parameters of the ECL are given in Table. 2.3.

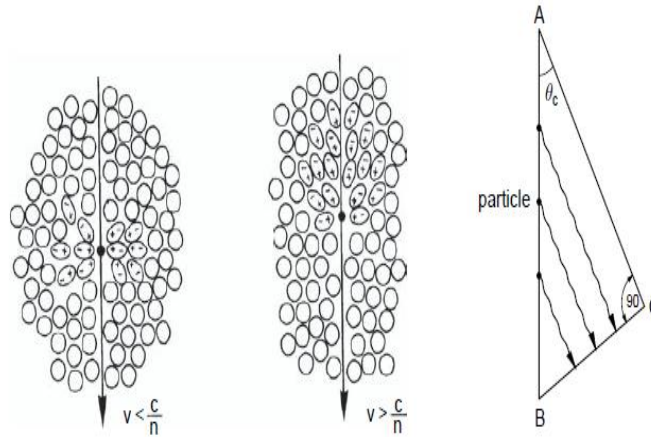


FIGURE 2.12: Cherenkov effect and Cherenkov angle.

TABLE 2.3: Geometrical parameters of the Electromagnetic Calorimeter.

	$\theta$ coverage	$\theta$ seg.	$\phi$ seg.	No. of crystals
Forward End cap	11.7° - 31.5°	13	48-128	1168
Barrel	32.2° - 128.7°	46	144	6624
Backward End cap	130.8° - 158.3°	10	64-144	1024

### 2.1.3.5 $K_L/\mu$ Detector

The  $K_L$  and  $\mu$  detection system is known as KLM and it is made up of an array of resistive-plate counters interspersed in the iron magnetic return yoke.

The detector covers an angle  $\theta$  ranging from 17° to 150°. The detector is located at the outermost region of the Belle detector after all other sub-detectors. It can detect muons with momenta greater than 600 MeV/c. A  $K_L$  or neutron will typically travel one interaction length before interacting. One interaction length is defined as the mean free path before an inelastic collision takes place. If a charged track pierces through different layers of material in the KLM, then the charged track is most probably a muon.

Muons usually undergoes smaller deflections in material and thus can be sorted out from charged pions and kaons. The KLM contains repeated layers of charged-particle detectors and iron plates with the thickness of 4.7 cm. In the barrel region of the

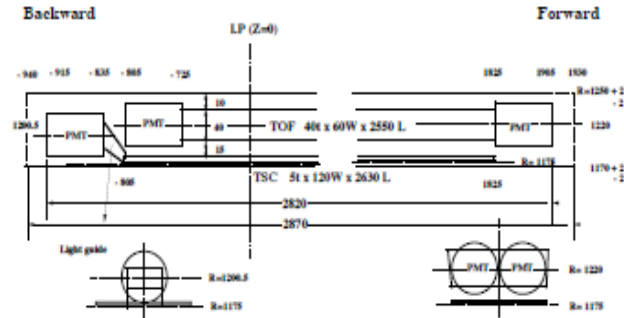


FIGURE 2.13: Schematic diagram of TOF and TSC.

detector, the KLM has an octagonal shape and it consists of 15 layers of detector and 14 layers of iron. In the forward and backward end-caps of the detector the KLM has 14 detector layers in each.

### 2.1.3.6 Particle identification

All particles are identified through combining information from the various sub-detectors, combined into a likelihood for the track or shower to be a certain particle.

A charged track is determined to be a pion or kaon by the likelihood ratio  $\mathcal{L}_\kappa$ , and the likelihood ratio combines the  $dE/dx$  information, the light yield measurements from the ACC and the time of flight information from TOF. The same can be done to discriminate between the pion and proton hypotheses and kaon and proton hypotheses.

Electrons are identified using the same information plus the ECL information. Muons are identified using the same information as the electrons plus the hadronic calorimeter information. Photons are identified from the shower shape in the ECL.

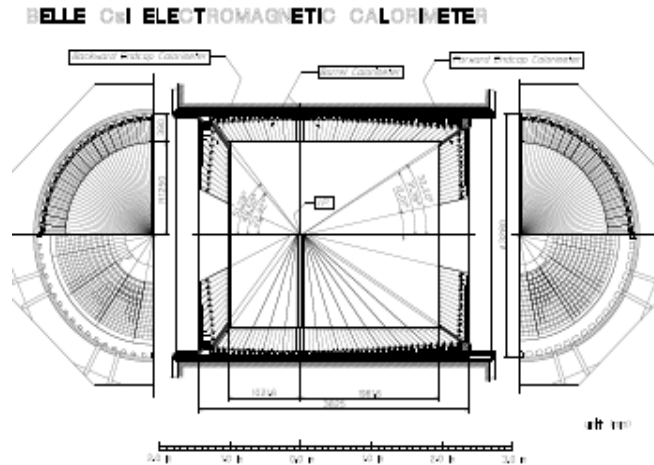


FIGURE 2.14: Schematic diagram of the ECL.

### 2.1.3.7 Solenoid Magnet

All of these above specified sub detectors except for the KLM detector are placed inside a superconducting solenoid (of diameter 3.4 m) which supplies an axial magnetic field of 1.5 T. The external iron construction of the Belle detector acts as the path of the magnetic flux to return and it also absorbs material for the KLM detector. The specifications of the solenoid are shown in Table 2.4.

## 2.2 Triggering and Data Collection

In order to acquire data from events there is a trigger system which determines when an interesting event happened, and orders the Data Acquisition system to record the event.

### 2.2.1 Trigger system

The trigger system selects events to document and store them permanently. At Belle, the essential events that we are interested in to study and analyse are :  $e^+e^- \rightarrow B\bar{B}$  ,  $e^+e^- \rightarrow q\bar{q}$ , ( $q = u, d, s, c$ ),  $e^+e^- \rightarrow \tau^+\tau^-$  and  $e^+e^- \rightarrow \gamma\gamma$ . A fraction of the total Bhabha scattering  $e^+e^- \rightarrow e^+e^-$  and muon pairs  $e^+e^- \rightarrow \mu^+\mu^-$  is also recorded by the trigger system to help monitor the luminosity and calibrate the detector. The

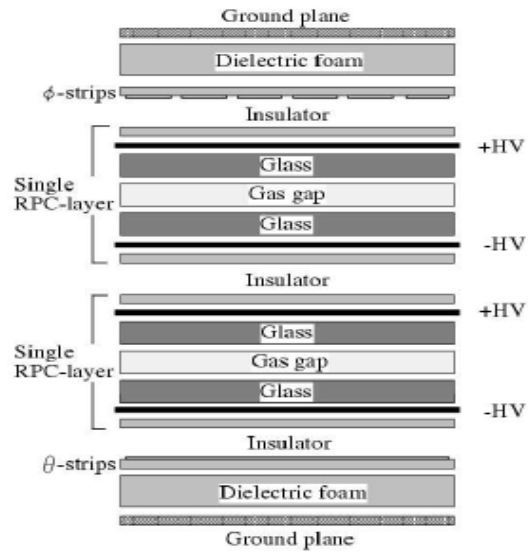


FIGURE 2.15: Cross-section of the KLM super-layer.

TABLE 2.4: Solenoid magnet

General	Central field	1.5 T
	length	4.41 m
	Weight	23 t
	Cool down time	6 days
	Quench recovery time	$\leq 1$ day
Cryostat	Inner/Outer radius	1.70/2.00 m
Coil	effective radius	1.8 m
	length	3.92 m
	Superconductor	NbTi/Cu
	Nominal Current	4400 A
	Inductance	3.6 H
	Stored energy	35 MJ
	Typical charging time	0.5 h

initial Level-1 (L1) trigger combines different information collected from each of the sub-detectors and feed it into the global decision logic (GDL) as shown in Fig. 2.16. The GDL can be applied to logic devices and it yields a trigger decision  $2.2 \mu\text{s}$  after the bunches of  $e^+$  and  $e^-$  cross each other.



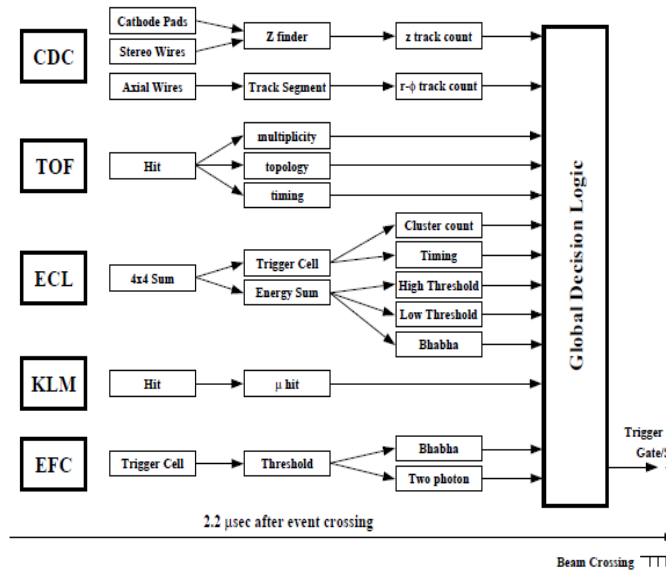


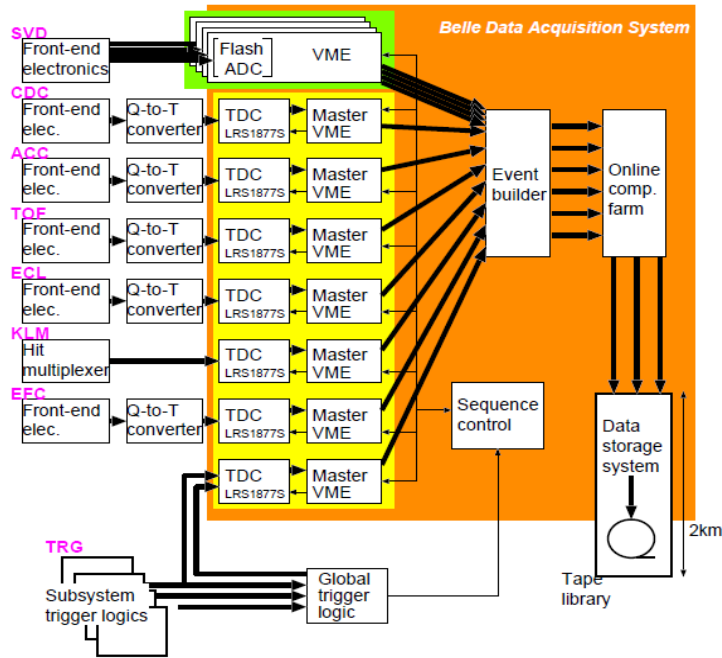
FIGURE 2.16: Illustration of the Belle Level-1 Trigger system.

## 2.3 Data Acquisition (DAQ)

The Belle DAQ system in Fig. 2.17, obtains data from the Belle subsystems (SVD, CDC, ACC, TOF, ECL, KLM, EFC) after a L1 trigger occurs. An event builder gathers data from the sub-detectors and then group them into events. The data at this point are just raw TDC and ADC (time and analog to digital converters) data. After the events are constructed they are sent to the on-line system where another trigger, Level-3 (L3) is applied to them. After the application of this trigger, the events can be written into the off-line storage. The schematic is shown in Fig. [? ].

## 2.4 Software and Simulation

An unprocessed event contains the values obtained from the TDC and ADC as described in the above section. Belle collaborators have developed a collection of software which turns those data into energy and momentum measurements of the particles detected. Three-momenta and associated information related to particle identification is stored in data files suitable for final analysis by collaborators. Monte Carlo (MC) simulation is very important in optimization of the signal events and studying and reducing background in physics analyses.

FIGURE 2.17: schematics of Data Acquisition (*DAQ*).

## 2.4.1 Monte Carlo Simulation

In order to analyse data and then to explain the results, we need to understand the performance of the detector and different possible background candidates present in the analysis. We generate a large sample of Monte Carlo (MC) data, with larger statistics than the collected data. With this simulated MC data we can estimate the reconstruction efficiency and detector resolution for the decay of interest. We follow two steps to simulate the MC. One step generates the underlying event (event generator) and the second step incorporates the interaction between the detector and the particles.

### 2.4.1.1 Event Generators

Event generators yield all the physics processes and subprocesses of the decay chain, resulting in a list of particle momenta and identities. The event generator **EvtGen** has been used to generate Monte Carlo data samples for this analysis. **EvtGen** is a generator adapted to include both continuum events and B events and it can reproduce an entire decay tree. **EvtGen** depends on a detailed description of the decays of our interest. It can simulate different models important for B physics, especially detailed models for semi-leptonic decays. **EvtGen** interfaces to JetSet [38], [39] to generate continuum such as  $e^+e^- \rightarrow q\bar{q}$  interactions ( $q = (u,d,s,c)$ ) at  $\Upsilon(4S)$  resonance and for generic hadronic decays of B mesons that are not implemented in the generator.

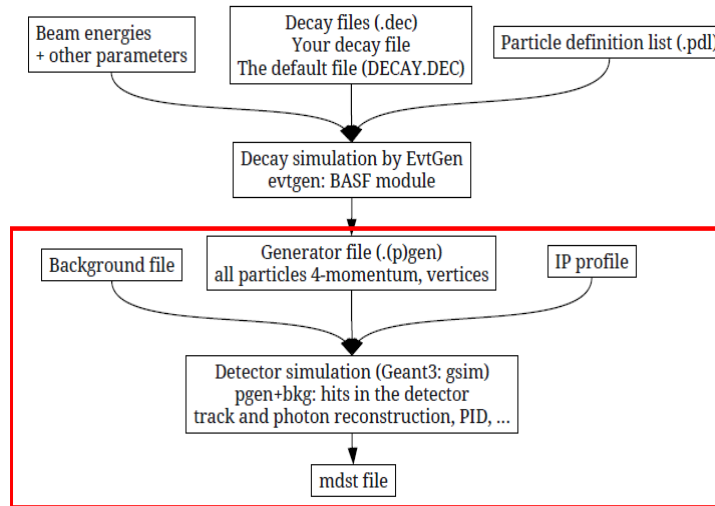


FIGURE 2.18: Monte Carlo.

#### 2.4.1.2 Simulation of the Detector Response

The generated decay chains are given to the modules which will take each particle through the detector. GEANT [40] simulates the detector geometry and materials distributions. It then simulates the passage of particles through matter. A group of GEANT based modules form a GSIM to simulate the detector configurations. The detector parameters are frequently upgraded based on real data information.

## Chapter 3

# Experimental methods and results in Monte Carlo

At Belle, we are interested in reconstructing  $e^+e^- \rightarrow c\bar{c} \rightarrow D_{tag}KX_{frag}D_s^*$  and  $D_s^* \rightarrow D_s\gamma$  [42]. The full reconstruction of  $e^+e^- \rightarrow c\bar{c}$  with a  $D_s$  meson event in it, goes through two stages; first reconstruction of the inclusive  $D_s$  events and second reconstruction of the exclusive decays of  $D_s \rightarrow \pi^0 l\nu$ ,  $D_s \rightarrow K_s l\nu$ ,  $D_s \rightarrow \rho l\nu$  to estimate the branching fraction of each of these three rare decay modes. The processes through which the data for analysing a desired event is collected, are described below. In this chapter, we also discuss the Monte Carlo simulation which plays an important role in providing us with a way to optimize our physics analyses.

### 3.1 Outline of the analysis method

We follow the same method of exclusive reconstruction of signal, tag, and fragmentation products previously used in the past by the Belle collaboration [51] and the Babar collaboration [52]. In particular we follow closely the analysis described in Ref. [42].

The method completely reconstructs the reaction

$$e^+e^- \rightarrow c\bar{c} \rightarrow D_{tag} K X_{frag} D_s^* \quad D_s^* \rightarrow D_s\gamma, \quad (3.1)$$

where  $D_{tag}$  is one of the charmed states listed in Section 3.1.2, which decays to a high purity hadronic state. The  $D_s^*$  meson decays through its dominant decay mode to a  $D_s$  which is searched for rare decay modes. Reconstructing all particles allows determination of the neutrino 4-momentum by applying kinematic constraints. Charge and flavor conservation cuts are applied to the final state. Eq. 3.1 implies charge conjugate states.

We are interested in the full reconstruction of  $e^+e^- \rightarrow c\bar{c}$  events which contains  $D_s$  mesons in two stages. One of these two  $c$  quarks forms a  $D_s$  meson and the other charm quark forms a charm hadron  $D_{tag}$  which is used for the tagging purpose.

The tagging candidate  $D_{tag}$  can be a  $D^0$ ,  $D^+$ ,  $\Lambda_c^+$ ,  $D^{*+}$  or  $D^{*0}$ . We demand an extra kaon  $K$  ( $K^+$  or  $K_s$ ) to preserve the strangeness of the event. In the case of  $\Lambda_c^+$  we demand a proton of the opposite charge to conserve the baryon number. During the hadronization process, some additional particles, indicated as  $X_{frag}$  are produced and also reconstructed individually. We use only low-background combinations of light hadrons. The signal  $D_s$  is required to come from a  $D_s^*$  which decays to  $D_s^* \rightarrow D_s\gamma$ , again to reduce backgrounds.

In the first stage of the analysis, we obtain entirely inclusively reconstructed sample of  $D_s$  events. The number of fully reconstructed  $D_s$  events is a useful quantity to normalize the branching ratio calculation and can be obtained from the distribution of events in  $M_0(D_{tag} K X_{frag}\gamma)$ , the mass recoiling against the  $D_{tag} K X_{frag}\gamma$  system.

$$M_0(D_{tag} K X_{frag}\gamma) = \sqrt{p_0(D_{tag} K X_{frag}\gamma)^2} \quad (3.2)$$

where  $p_0$  is the momentum of the recoiling event and is defined as:

$$p_0(D_{tag} K X_{frag}\gamma) = p_{e^+} + p_{e^-} - p_{D_{tag}} - p_K - p_{X_{frag}} - p_\gamma \quad (3.3)$$

$p_{e^+}$  and  $p_{e^-}$  are respectively the momenta of the electron and positron beams.  $p_{D_{tag}}$ ,  $p_K$ ,  $p_{X_{frag}}$ ,  $p_\gamma$  are the momenta of the candidates  $D_{tag}$ , kaon,  $X_{frag}$  and the daughter photon from  $D_s^* \rightarrow D_s\gamma$ . If the events in Eq. 3.1 are correctly reconstructed, then  $M_0$  will peak at the nominal  $D_s$  mass. Once the inclusive sample of  $D_s$  is selected, in the second stage we use this sample to reconstruct the fraction of events where the  $D_s$  decays into  $D_s \rightarrow \pi^0 l\nu, \rho l\nu, K_s l\nu$ . The stable particles of these decays are reconstructed exclusively: one extra charged track recognised as an electron or muon. The cuts for  $\pi^0$ ,  $\rho$  or  $K_s$  are described in each dedicated Section.

Before we describe the reconstruction procedure of each of the candidates, we shall briefly describe the final state particles reconstruction and the cuts applied on them.

### 3.1.1 Reconstruction of the final state particles and selection criteria applied on them

A charged track in a constant magnetic field is described by a helix. In a constant magnetic field a helix can be represented along z-axis by five parameters:  $d_r$ ,  $\phi_0$ ,  $\mathcal{K}$ ,

$d_z$  and  $\tan\lambda$ . The impact parameters  $|d_r|$  and  $|d_z|$  are the radial and the z positions subsequently of the point of closest approach of the helix to the interaction point. The reconstructed charged tracks must fulfil a loose selection criteria on impact parameters,  $|d_r| < 0.5$  cm and  $|d_z| < 3$  cm. These cuts help cutting off background tracks that do not come from the IP. Particle identification (PID) is done based on the likelihood ratios which can be calculated using the information from CDC (from dE/dx measurements), ACC and TOF. A charged track identity is estimated by the likelihood ratio  $\mathcal{L}_{\mathcal{K},\pi}$ , where  $\mathcal{L}_{\mathcal{K}}$  or  $\mathcal{L}_{\pi}$  are the likelihood that a particle is a K or a  $\pi$ .

Charged tracks with  $\mathcal{L}_{\mathcal{K},\pi} > 0.6$  are more likely to be kaons [53]. When taking data with the Silicon vertex detectors, the likelihood ratio appears to be 86.3% efficient for kaons while a 9.8% chance of misidentification for pions exist. Moreover, we have applied other veto cuts on the kaons to minimize electron and proton contamination. The similarly defined electron and proton likelihoods are required to be  $\mathcal{L}_e = < 0.9$  and  $\mathcal{L}_{\mathcal{K}/p} > 0.1$ .

The electrons are identified by using the information of the position, shower shape and cluster energy in ECL, joined with the information of track momentum and dE/dx in CDC and the hits in the CDC. The muons are identified by extrapolating the CDC tracks to the KLM and comparing the measured ranges and transverse fluctuation in the expected value in the KLM.

The electromagnetic calorimeter (ECL) contains the energy of an electro-magnetic shower generated by a photon. The crystal which contains the largest amount of energy in the cluster is known as a seed crystal. The energies in the 3X3 and 5X5 counters around this "seed crystal" are added up to measure the total cluster energy. Photons detected in the ECL must have minimum 50(100) MeV in the barrel( end-caps ) region in the laboratory frame. Neutral  $\pi^0$  candidates are reconstructed with pair of photons with invariant mass between 120 and 150 MeV/ $c^2$ , which selects candidates within  $\pm 3.2\sigma$  around the nominal  $\pi^0$  mass ( $\sigma$  being the nominal  $\pi^0$  mass) [37].

Neutral kaon candidates can be reconstructed using pair of charged pions with invariant mass within  $\pm 5\sigma$ , which is  $\pm 20\text{MeV}/c^2$  of the nominal kaon mass. The neutral  $K_s$  candidates are reconstructed using pairs of tracks with opposite charges, with assumed pion hypothesis. The  $\Lambda$  baryons are reconstructed by pairing a proton and a charged pion candidate with opposite charges.

We first perform a process known as "Skimming" for the charm events. The point of skimming is to remove events in which we don't reconstruct a good candidate and hence save on disk space. We restrict our analysis to events which can pass these skims, so that we can concentrate on a smaller set of data, decreasing the processing time and difficulties that can occur from operating the full Belle data. So skimming reduces the

total size of the data. The skim uses cuts depending on the charged track multiplicity, the calorimeter cluster multiplicity, the total visible energy, the energy deposited in the calorimeter, the overall momentum balance in the z-direction, and the average ECL cluster energy. It also demands that the event vertex is true to the known IP to remove events caused by beam particles hitting on the beam pipe or the remaining gas molecules.

The following criteria to select  $\pi^\pm$ ,  $K^\pm$ , leptons, p,  $\gamma$ ,  $\pi^0$ ,  $K_S$ ,  $\Lambda$  are given as follows:

1. All charged tracks will be selected with:
  - $|d_r| < 0.5$  cm for all tracks (The impact parameter w.r.t the IP of each charged particle in  $r - \phi$  plane.)
  - $|d_z| < 0.15$  cm for all tracks (The impact parameter w.r.t the IP of each charged particle along the beam direction.)
2.  $\pi^\pm$ :
  - $\mathcal{L}_{K,\pi} < 0.9$
  - $\mathcal{L}_e < 0.9$  (electron veto)
  - $\mathcal{L}_\mu < 0.9$  (muon veto)
  - $\mathcal{L}_{\pi,p} > 0.1$  (proton veto)
3.  $K^\pm$ :
  - $\mathcal{L}_{K,\pi} > 0.6$
  - $\mathcal{L}_e < 0.9$  (electron veto)
  - $\mathcal{L}_\mu < 0.9$  (muon veto)
  - $\mathcal{L}_{K,p} > 0.1$  (proton veto)
4. Leptons:
  - $\mathcal{L}_e > 0.9$  for electron candidates
  - $\mathcal{L}_\mu > 0.9$  for muon candidates
5. p:
  - $\mathcal{L}_{K,p} < 0.9$
  - $\mathcal{L}_{\pi,p} < 0.9$
6.  $\gamma$ :
  - $E_\gamma > 50$  MeV if  $\gamma$  has been found in the barrel ECL region
  - $E_\gamma > 100$  MeV if  $\gamma$  has been found in the forward ECL region

- $E_\gamma > 150$  MeV if  $\gamma$  has been found in the ECL region

7.  $\pi^0$ :

- $117.8 \text{ MeV} < M_{\gamma\gamma} < 150.2 \text{ MeV}$  fit is performed

8.  $K_s$ :

- $|M_{\pi\pi} - M_{K_s^0}| < 20 \text{ MeV}$
- Vertex fit is performed

9.  $\Lambda$ :

- $|M_{p\pi^-} - M_\Lambda| < 5 \text{ MeV}$
- vertex fit is performed

### 3.1.2 $D_{tag}$ reconstruction

Table 3.1 lists all tags which include a charmed hadron reconstructed in hadronic decay modes.

The center of mass momentum of the  $D_{tag}$  candidate  $p_{D_{tag}} > 2.3 \text{ GeV}$  to reject  $B$  decay backgrounds. If  $D_{tag}$  is an excited state, we request  $p_{D_{tag}} > 2.5 \text{ GeV}$ .

$D$  candidates are combined with pions and photons to form  $D^{*+} \rightarrow D^0\pi^+, D^+\pi^0$  and  $D^{*0} \rightarrow D^0\pi^0, D^0\gamma$  candidates.

Table 3.2 lists all the excited states considered. This reconstruction is useful to lower the combinatorics of the subsequent  $KX_{frag}\gamma$  reconstruction. The absorption of one more particle to  $D_{tag}$  reduces the combinatoric background, and the reconstruction of  $D^{*+} \rightarrow D^0\pi^+$  determines the quark content of  $D^0$  which decays to a  $K_s$ .

### 3.1.3 Primary kaon reconstruction

After the reconstruction of the tagging  $D$  candidate, a kaon candidate is demanded. The primary kaon candidate can be  $K^\pm$  and  $K_s^0$ , which do not coincide with the  $D_{tag}$  daughters. If the kaon is charged, it is requested that its charge be the same sign as the charm quantum number of the tag. The  $K^\pm$  and  $K_s^0$  should pass the following selection criteria:

1.  $K^\pm$ : -  $p > 0.1 \text{ GeV}$  - other selection criterion are same as described in subsection 3.1.1.



2.  $K_s$ : -selection criterion are same as described in subsection 3.1.1.

ID	$D^0$	$\mathcal{B}$	ID	$D^+$	$\mathcal{B}$	ID	$\Lambda_c^+$	$\mathcal{B}$
1	$K^-\pi^+$	3.9	21	$K^-\pi^+\pi^+$	9.4	31	$pK^-\pi^+$	5.0
2	$K^-\pi^+\pi^0$	13.9	22	$K^-\pi^+\pi^+\pi^0$	6.1	32	$pK^-\pi^+\pi^0$	3.4
3	$K^-\pi^+\pi^+\pi^-$	8.1	23	$K_s^0\pi^+$	1.5	33	$pK_s^0$	1.1
4	$K^-\pi^+\pi^+\pi^-\pi^0$	4.2	24	$K_s^0\pi^+pi^0$	6.9	34	$\Lambda\pi^+$	1.1
5	$K_s^0\pi^+\pi^-$	2.9	25	$K_s^0\pi^+\pi^+\pi^-$	3.1	35	$\Lambda\pi^+\pi^0$	3.6
6	$K_s^0\pi^+\pi^-\pi^0$	5.4	26	$K^+K^-\pi^+$	1.0	36	$\Lambda\pi^+\pi^+\pi^-$	2.6
	Sum	38.4		Sum	28		Sum	16.8

TABLE 3.1: Ground state  $D_{tag}$  decay modes used in the measurement

ID	$D^{*+}$	$\mathcal{B}$	ID	$D^{*0}$	$\mathcal{B}$
100	$D^0\pi^+$	67.7	200	$D^0\pi^0$	61.9
120	$D^+\pi^0$	30.7	300	$D^+\gamma$	38.1
	Sum	98.4		Sum	100

TABLE 3.2: Excited  $D_{tag}$  decay modes used in the measurement

### 3.1.4 $X_{frag}$ reconstruction

The tracks and  $\pi^0$  candidates left in the event, not overlapping with the  $D_{tag}$  K system can be used to reconstruct the  $X_{frag}$  candidates in the following modes:

- nothing
- $\pi^\pm$
- $\pi^0$
- $\pi^0\pi^\pm$
- $\pi^+\pi^-$
- $\pi^+\pi^-\pi^\pm$
- $\pi^+\pi^-\pi^0$

We also require that the total charge of the  $D_{tag}KX_{frag}$  system be  $\pm 1$ . The modes which contain only one  $\pi^0$  and only up to 3 charged pions are allowed to form the  $X_{frag}$  system. Higher multiplicity modes have unfavourable combinatoric background.

### 3.1.5 Reconstruction of inclusive $D_s^*$ candidates

The inclusive  $D_s^*$  candidates with a missing mass  $M_1 = M_{miss}(D_{tag}KX_{frag})$  between 2.0 GeV and 2.25 GeV are selected. This cut corresponds to approximately a  $\pm 3\sigma$  cut.

### 3.1.6 Reconstruction of Inclusive $D_s$ candidates

The inclusive  $D_s$  candidate is identified by looking for the decay of  $D_s^* \rightarrow D_s\gamma$  where the photon candidate does not overlap with the  $D_{tag}KX_{frag}$  system. The correctly reconstructed photon candidate must be selected with

- $E_\gamma > 120MeV$
- $E_9/E_{25} > 0.75$  ( This is the ratio of total energies in 3X3 and in 5X5 ECL crystals in the transverse plane around the crystal with a largest amount of energy deposited. )
- $\cos\theta$  must be negative, where  $\theta$  is the angle between the direction of the tagging  $D$  hadron and the direction of the photon candidate coming from  $D_s^* \rightarrow D_s\gamma$  [42]. This ensures that the signal photon must be in the signal hemisphere of the event.

The  $D_{tag}KX_{frag}\gamma$  systems will be selected only with

- $p_0(D_{tag}KX_{frag}\gamma) > 2.8GeV$
- $M_0(D_{tag}KX_{frag}\gamma) > 1.83GeV$

## 3.2 Monte Carlo samples

### 3.2.1 Signal MC samples

In order to study the characteristics of signal events, signal MC samples have been generated for each of our three decay modes with a  $4 \times 10^7$  total events according to ISGW2 [41] distribution. ISGW2 is a model used for the semi-leptonic decays of B, D,  $D_s$  mesons.

We assume that  $D_s^* \rightarrow D_s\gamma$  decay is 100%, and the decay  $D_s \rightarrow \pi^0/\rho/K_s e\nu$  is 50% and  $D_s \rightarrow \pi^0/\rho/K_s \mu\nu$  is 50%. Table 3.3 lists all the Signal MC datasets.

TABLE 3.3: Signal MC samples

Mode	Number of events	Model
$D_s \rightarrow \pi^0 l \nu$	$4 \times 10^7$	ISGW2
$D_s \rightarrow \rho l \nu$	$4 \times 10^7$	ISGW2
$D_s \rightarrow K_s l \nu$	$4 \times 10^7$	ISGW2

### 3.2.2 Generic MC samples

For the purpose of the study of the background and also to calculate the reconstruction efficiency, 6 streams having about six times the number of the data events and all 4 types (charged, mixed, charm, uds) of generic Monte Carlo samples have been used.

## 3.3 Monte Carlo background categories characterization

The inclusive  $D_s$  candidates are divided into 6 categories based on the source of the signal photon originated from  $D_s^* \rightarrow D_s \gamma$  decay [42]. Correctly reconstructed inclusive  $D_s$  samples can be obtained by using the selection category 1: true signal which states:

- $D_s^* \rightarrow D_s \gamma$  obtained in the event
- $\gamma$  comes from  $D_s^*$
- Primary kaon is accurately selected out and is not originated in  $D_s$  decay chain
- Pions in the  $X_{frag}$  system are not originated in  $D_s$  decay chain and accurately selected out.

The five other categories based on the background sources of the signal photon coming from  $D_s^* \rightarrow D_s \gamma$  are described below [42]:

1. category 2: Peaking  $D^*$ 
  - $\gamma$  is obtained from  $D^{*0} \rightarrow D^0 \gamma$  (97%) or  $D^{*+} \rightarrow D^0 \pi^+ \gamma_{FSR}$  (3%) decays
2. category 3:  $D_s^* \rightarrow \pi^0 \rightarrow \gamma$ 
  - $\gamma$  is coming from  $\pi^0 \rightarrow \gamma \gamma$  decay
  - $\pi^0$  generated from  $D^{*+} \rightarrow D^+ \pi^0$  (28%),  $D^{*0} \rightarrow D^0 \pi^0$  (67%),  $D_s^* \rightarrow D_s \pi^0$  (5%) decays

3. category 4: wrong  $\gamma$ 
  - not included in the other categories
  - The ECL cluster generating the  $\gamma$  candidate was produced by the wrong  $\gamma$  (addbg, charged tracks, ...)
4. category 5:  $\gamma$  from  $\pi^0$ 
  - $\gamma$  is generated in the  $\pi^0 \rightarrow \gamma\gamma$  decay
  - $\pi^0$  does not come from  $D^{*+} \rightarrow D^+\pi^0$ ,  $D^{*0}D^0\pi^0$  or  $D_s^* \rightarrow D_s\pi^0$  decays
5. category 6: Mis-reconstructed signal
  - Produced  $D_s^* \rightarrow D_s\gamma$  decay originated in an event
  - $\gamma$  is coming from  $D_s^*$
  - Primary kaon or one of the pions from fragmentation system  $X_{frag}$  are produced in  $D_s$  decay chain or misidentified

The  $M_0$  distribution of the fully reconstructed  $D_s$  events is shown in Fig. 3.1 in generic MC data and it is color coded to show the contribution of each of the six categories mentioned above. The distribution in blue is due to category 1 which is the correctly reconstructed inclusive sample of  $D_s$  with category 1: true signal. The largest background contribution comes from the green region in the distribution which is due to category 5:  $\gamma$  from  $\pi^0$ .

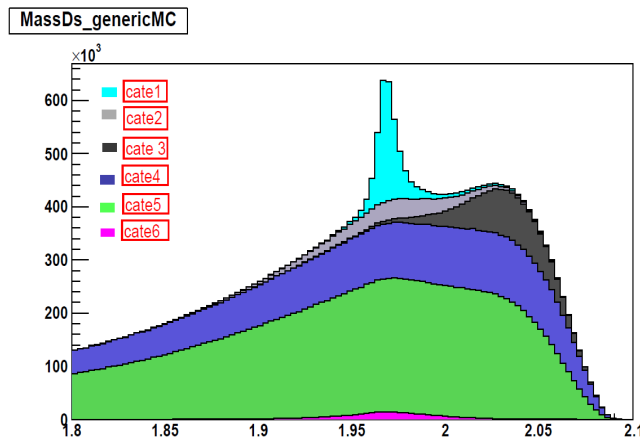


FIGURE 3.1: Generic MC:  $M_0$  distribution in sky blue for correctly reconstructed (cate1)  $D_s$  events and  $M_0$  distributions for five other categories (color specifications given on the plot)

### 3.4 Fit to $M_0$ in Monte Carlo data.

A binned maximum likelihood fit to the  $M_0$  distributions for  $\pi^0 l \nu$ ,  $\rho l \nu$  and  $K_s l \nu$  modes have been performed using a signal peak comprising of two Gaussian functions  $\mathbf{G}$  added to a Crystal ball function  $\mathbf{C}$ , a Breit Weigner function  $\mathbf{BW}$  and a Landau function  $\mathbf{L}$ . All these functions are unitary, that is they integrate to one.

The binned  $M_0$  histogram in the signal MC sample is used to obtain the probability density function (PDF) of the signal peak after applying all the cuts established so far. The fit PDF in signal MC sample is described as

$$f_{sig}(M_0) = N f_3 (f_1 C(M_0; m_0, \sigma, \alpha, n) + f_2 G_1(M_0; \mu_1, \sigma_1) + (1 - f_1 - f_2) BW(M_0; m_{bw}, \sigma_{bw})) + f_4 G_2(M_0; \mu_2, \sigma_2) + (1 - f_3 - f_4) L(M_0; m_l, s_l). \quad (3.4)$$

This  $M_0$  distribution in each of the  $\pi^0 l \nu$  and  $\rho l \nu$  mode in generic MC, is fitted with the signal peak fixed with the obtained parameter values from the signal MC fit plus a background comprised of a cubic polynomial added to a crystal ball with non-zero variable peak. The Crystal Ball function is used to fit a bump in the upper part of the  $M_0$  spectrum. The  $K_s l \nu$  mode is fitted with the fixed signal peak from the signal MC fit and a quadratic polynomial added to a Crystal Ball with non-zero peak. The background PDF is:

$$f_{bkg}(M_0) = \sum_i a_i (M_0)^i + (1 - f_5) C(M_0; m_{bkg}, \sigma_{bkg}, \alpha, n). \quad (3.5)$$

These fits are shown in Fig. 3.2 through Fig. 3.4.

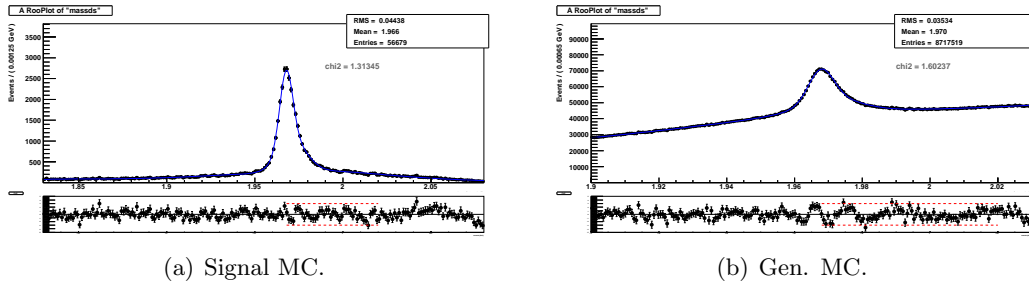
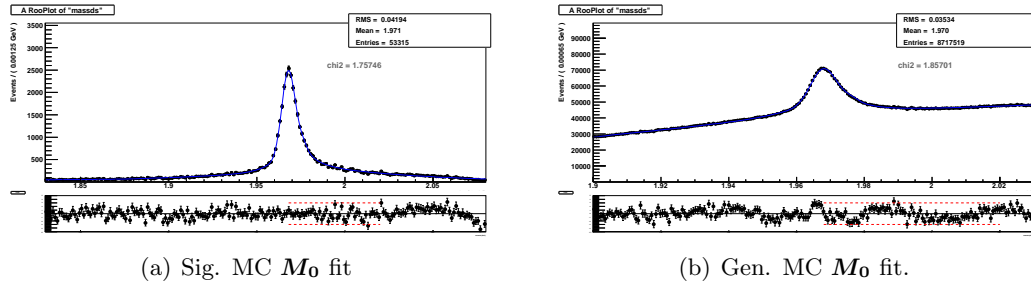
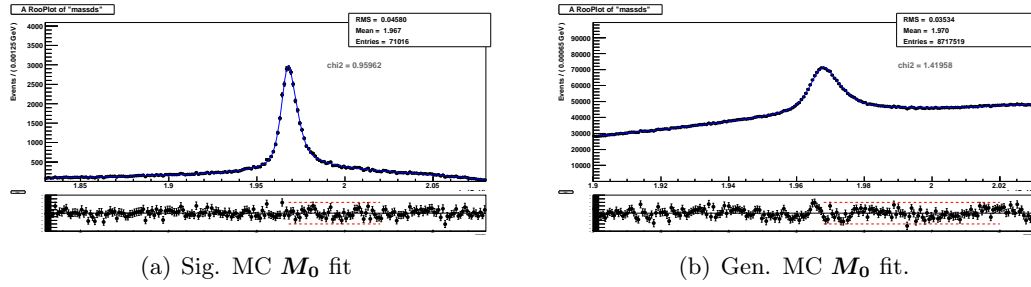


FIGURE 3.2:  $M_0$  fit in  $D_s \rightarrow \pi^0 l \nu$  mode.

#### 3.4.1 Summary of MC analysis.

The fit result for each of the decay mode will provide us with the number of correctly reconstructed inclusive  $D_s$  which is a necessary quantity to calculate the reconstruction

FIGURE 3.3:  $M_0$  fit in  $D_s \rightarrow \rho l \nu$  mode.FIGURE 3.4:  $M_0$  fit in  $D_s \rightarrow K_s l \nu$  mode.

efficiency in signal MC. We fit the  $M_0$  distribution in generic MC, in order to extract the number of correctly reconstructed inclusive  $D_s$ . With this number in generic MC, we'll be able to estimate an approximate branching fraction for each of our decay modes. The numbers of correctly reconstructed inclusive  $D_s$  in signal MC samples are:

- $D_s \rightarrow \pi^0 l \nu$  :  $N_{incl} = 56679 \pm 236.25$ .
- $D_s \rightarrow \rho l \nu$  :  $N_{incl} = 53315 \pm 230.90$ .
- $D_s \rightarrow K_s l \nu$  :  $N_{incl} = 71016 \pm 265.87$ .

The number of correctly reconstructed inclusive  $D_s$  in generic MC sample is:

- $N_{incl} = 1200969 \pm 5048.58$  in  $D_s \rightarrow \pi^0 l \nu$ .
- $N_{incl} = 1248112 \pm 230.90$  in  $D_s \rightarrow \rho l \nu$ .
- $N_{incl} = 1335079 \pm 265.87$  in  $D_s \rightarrow K_s l \nu$ .

### 3.5 Reconstruction of exclusive $D_s \rightarrow \pi^0/\rho/K_s l \nu$ decays

With the correctly reconstructed sample of inclusive  $D_s$  mesons, we look for the exclusive  $D_s$  decays:

- $D_s \rightarrow \pi^0 l \nu$
- $D_s \rightarrow \rho l \nu$
- $D_s \rightarrow K_s l \nu$

Our aim is to measure the branching fraction  $\mathcal{B}$  of the above rare semi-leptonic  $D_s$  decays.

The signal branching fractions of  $D_s$  to a random final state  $f$  reconstructed in the final stage of the analysis is given as follows:

$$\mathcal{B}(D_s \rightarrow f) = \frac{N_{excl}(D_s \rightarrow f)}{N_{incl}^{D_s} \epsilon(D_s \rightarrow f)} \quad (3.6)$$

Here  $N_{incl}^{D_s}$  is the number of inclusively reconstructed  $D_s$  mesons in the first stage of the analysis  $N_{excl}(D_s \rightarrow f)$  is the number of exclusively reconstructed  $D_s \rightarrow f$  decays in the second stage of the analysis.  $\epsilon(D_s \rightarrow f)$  represents the reconstruction efficiency of the exclusive  $D_s \rightarrow f$  decays in tagged events in signal MC.

For each  $D_{tag} K X_{frag} \gamma$  system, the lists of remaining charged tracks and  $\pi^0$  or  $\rho$  or  $K_s$  candidates which are not associated to the  $D_{tag} K X_{frag}$  system are filled. Before we start the reconstruction of these exclusive decays, we need to identify each of the charged and neutral particles and then measure their four momenta. We require exactly one lepton and one  $h = \pi^0/\rho/K_s$  candidate left in the rest of the event. We require that there is no remaining track left after reconstructing the signal side events.

Selection criteria common to all sub-analyses:

1. Inclusive  $D_s$  signal region mass selection:  $1.95 \text{ GeV} < M_0 < 1.99 \text{ GeV}$ .
2. For each  $D_{tag} K X_{frag} \gamma$  system we require exactly one hadron  $h = \pi^0/\rho/K_s$  in the rest of the event. In the case of  $\pi^0$  we require only one  $\pi^0$ . In case of  $\rho/K_s$  extra  $\pi^0$ s are allowed.
3. For each  $D_{tag} K X_{frag} \gamma h$  system there is exactly one lepton left in the event.
4. The lepton charge must be opposite the charm quantum number of the tag, if it can be determined. The charged tracks are selected as mentioned in subsection 3.1.1.

Mode specific cuts will be discussed in each sub-analysis.

### 3.5.1 $E_{ecl}$ , $E_\nu$ and $MM^2$

We use three more variables for further background rejection:  $E_{ecl}$ ,  $E_\nu$  and  $MM^2$ .  $E_{ecl}$  is defined as the total electromagnetic energy, in the signal hemisphere, which is not associated with signal or tag objects. ECL clusters with energy  $> 50$  MeV in barrel,  $> 100$  MeV in forward and  $> 150$  MeV in the backward end cap are used to calculate  $E_{ecl}$ . For signal events  $E_{ecl} = 0$  or a small value arising from beam background hits, so signal events peak at low  $E_{ecl}$  and background events are distributed towards higher  $E_{ecl}$  due to the contribution from additional neutral clusters.

Neutrino energy  $E_\nu$  in the  $D_s$  rest frame is defined as:

$$E_\nu = \frac{(M_{D_s}^2 - M_{\pi^0/\rho, K_s, l}^2)}{2M_{D_s}} \quad (3.7)$$

$MM^2$  is the invariant mass squared of the neutrino candidate and is defined as:

$$MM^2 = |p_\nu(D_{tag} K X_{frag} \gamma l \pi^0 / \rho / K_s)|^2 = |p_{e^+} + p_{e^-} - p_{D_{tag}} - p_K - p_{X_{frag}} - p_\gamma - p_l - p_h|^2 \quad (3.8)$$

For well reconstructed neutrino candidates,  $MM^2$  will peak at zero. The quantities ( $E_{ecl}$ ,  $E_\nu$ ) are used to reduce the backgrounds and  $MM^2$  is used in the final analysis. The method is summarized in the next Section, and Table 3.4 summarizes the best cuts in the ( $E_{ecl}$ ,  $E_\nu$ ) space for each sub-analysis.

Modes	Selection	No. of Signal Evt	No. of Bkg Evt	$\epsilon_{sig}$	$\epsilon_{bkg}$
$\pi^0 \mu \nu$	$E_{ecl} < -0.8 * E_\nu + 1.68$	2460 (out of 2518)	377(out of 442)	<b>97.7%</b>	<b>85.3%</b>
$\pi^0 e \nu$	$E_{ecl} < -1.4 * E_\nu + 1.68$	2331(out of 2512)	238(out of 338)	<b>92.8%</b>	<b>70.4%</b>
$\rho \mu \nu$	$E_{ecl} < -0.8 * E_\nu + 1.04$	2725 (out of 3120)	1019(out of 1622)	<b>87.3%</b>	<b>62.8%</b>
$\rho e \nu$	$E_{ecl} < -0.2 * E_\nu + 1.04$	3333 (out of 3554)	902 (out of 1154)	<b>93.8%</b>	<b>78.1%</b>
$K_s \mu \nu$	$E_{ecl} < 10 * E_\nu - 2.16$	3573 (out of 3880)	57 (out of 202)	<b>92.1%</b>	<b>28.2%</b>
$K_s e \nu$	$E_{ecl} < -16.4 * E_\nu + 15$ (No Cuts)	4509 (out of 4510)	21 (out of 23)	<b>99.9%</b>	<b>91.3%</b>

TABLE 3.4: Best ( $E_{ecl}$ ,  $E_\nu$ ) Selection Criteria For each sub-analysis. The third column represents the optimized efficiency for signal events, and the fourth column the optimized efficiency for background events.

### 3.5.2 Yield determination procedure

Each final stage candidate in the exclusive decay mode of  $D_s$  is specifically reconstructed except for the neutrino candidate. The signal yield is obtained by fitting the  $MM^2$  distribution.



The selection criteria to optimize signal over background are obtained from optimized  $(\mathbf{E}_{ecl}, \mathbf{E}_\nu)$  cuts, but also by studying the main background modes. The optimizing variable

$$FOM = \frac{\sigma S}{\sqrt{\sigma S + \beta B}}$$

is used to decide which cuts should be implemented in the  $(\mathbf{E}_{ecl}, \mathbf{E}_\nu)$  space.  $S$  and  $B$  are the number of events in the signal and generic MC respectively, which pass all cuts so far, and have  $-0.05 < MM^2 < +0.05$ .  $\sigma$  and  $\beta$  are variables which normalize the denominator quantities to expected data rates. For the six streams of Generic MC we estimate  $\beta = 0.182$ .  $\sigma$  is computed as

$$\sigma = \frac{2N_{data}f_{c \rightarrow D_s}\mathcal{B}}{4 \times 10^7}.$$

The first factor of two is due to having two charm decays for each charm annihilation event.  $4 \times 10^7$  is likewise the number of charm decays in signal MC, with factors of two cancelling out (number of charm decays and number of  $c \rightarrow \mu$  decays). Assuming  $N_{data} = 10^9 e^+e^- \rightarrow c\bar{c}$  events in the data, a  $f_{c \rightarrow D_s} = 0.08$  probability of the c-quark hadronizing into a  $D_s$ ,  $\sigma = 4\mathcal{B}$ .

It is noted that the FOM is zero for zero branching ratio. Its value represents the projected statistical significance of the analysis, under an assumed branching ratio. For presentation purposes, we also consider nominal branching ratios  $\mathcal{B}_0$  of  $(1.25 \times 10^{-4}, 1.25 \times 10^{-4}, 3.7 \times 10^{-3})$  for  $(\pi^0, \rho, K_s)e\nu$ . The muon nominal branching ratios are the same values as for the electron channels.

Three types of cuts are considered:

- $\mathbf{E}_{ecl}$  cuts only,  $\mathbf{E}_{ecl} < \mathbf{E}_1$ ;
- “square” cuts,  $(\mathbf{E}_{ecl} < \mathbf{E}_1, \mathbf{E}_\nu > \mathbf{E}_2)$ ;
- “triangular” cuts  $(\mathbf{E}_{ecl} < a_1\mathbf{E}_\nu + b_1, \mathbf{E}_{ecl} < a_2\mathbf{E}_\nu + b_2)$ , with the linear coefficients being both positive and negative.

In the case of triangular cuts, in all cases we find that only one of the cuts contributes to optimal selection, so only two coefficients are quoted below. Both triangular and square cuts are optimized with a raster scan in parameter space. The optimal  $(\mathbf{E}_{ecl}, \mathbf{E}_\nu)$  cuts for this analysis are reported in Table 3.4. The best figures of merit  $FOM_{best}$  obtained for each set of cuts at the nominal branching ratios are shown in Table 3.5. Because the  $K_s l \nu$  events are vastly improved by a triangular cut, we adopt triangular cuts in all modes.

TABLE 3.5: Best figures of merit  $FOM_{best}$  for a type of cut and nominal branching ratio  $\mathcal{B}$ ,

Mode	Nominal B.R.	FOM(best) $_{E_{ecl}only}$	FOM(best) $_{Squarecut}$	FOM(best) $_{Triangularcut}$
$D_s \rightarrow \pi^0 \mu \nu$	$1.25 \times 10^{-4}$	0.151	0.152	0.150
$D_s \rightarrow \pi^0 e \nu$	$1.25 \times 10^{-4}$	0.177	0.177	0.179
$D_s \rightarrow \rho \mu \nu$	$1.25 \times 10^{-4}$	0.101	0.102	0.100
$D_s \rightarrow \rho e \nu$	$1.25 \times 10^{-4}$	0.131	0.131	0.130
$D_s \rightarrow K_s \mu \nu$	$3.7 \times 10^{-3}$	5.67	6.45	6.57
$D_s \rightarrow K_s e \nu$	$3.7 \times 10^{-3}$	7.66	7.66	7.85

### 3.6 $D_s \rightarrow \pi^0 l \nu$ analysis

The  $\pi^0$  signal selection is done with mode specific hadron cuts, described as follows:

1.  $117.8 \text{ MeV} < M_{\gamma\gamma} < 150.2 \text{ MeV}$
2. The daughter photons from  $\pi^0$  must not be used in the reconstruction of  $D_{tag} K X_{frag} \gamma$  candidates

The daughter photons from  $\pi^0$  undergo the cuts mentioned in subsection 3.1.1.

The FOM main characteristics for the  $\pi^0 l \nu$  mode are shown in Fig. 3.5. In the first column, the dependence of FOM on the  $E_{ecl}$  cut is shown, for the nominal  $\mathcal{B}$ . The curve rises and flattens out at high values of the cut. The second column shows the dependence of the optimal FOM on the branching ratio  $\mathcal{B}$  for  $E_{ecl}$  cuts alone, square and slanted ( $E_{ecl}, E_\nu$ ) cuts. The cuts are all very similar for this mode.

#### 3.6.1 MC analysis.

Figure 3.6 shows the  $MM^2$  distributions for  $D_s \rightarrow \pi^0 \mu \nu$  and  $D_s \rightarrow \pi^0 e \nu$  decays in Generic MC before cuts in the  $(E_{ecl}, E_\nu)$  space. Background sources are color coded coming from correctly reconstructed inclusive  $D_s$  selected with category 1: true signal and the background events coming from other five categories as described in section 3.3.

The one dimensional  $E_{ecl}$  distributions for  $D_s \rightarrow \pi^0 l \nu$  decays are shown in Fig. 3.7, and the  $E_\nu$  distributions are in Fig. 3.8.

The two dimensional scatter plots for  $D_s \rightarrow \pi^0 \mu \nu$  and  $D_s \rightarrow \pi^0 e \nu$  decays are shown in Fig. 3.9 through Fig. 3.11. The  $(E_{ecl}, E_\nu)$  variables are not used in the final analysis, and their scatter plot is used to reduce backgrounds.

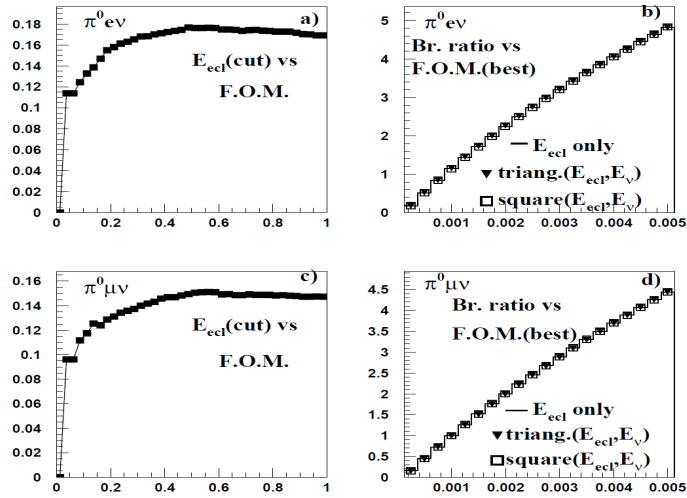
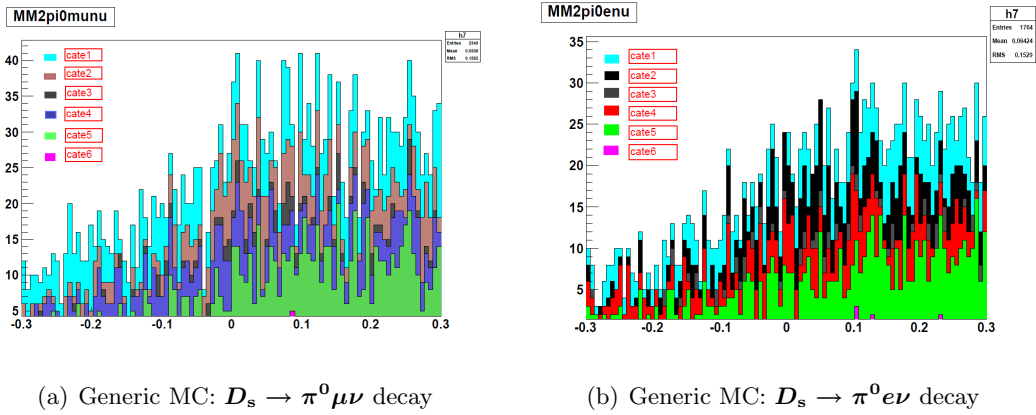


FIGURE 3.5: First row:  $D_s \rightarrow \pi^0 e \nu$ , Second row:  $D_s \rightarrow \pi^0 \mu \nu$ . First column: FOM versus  $E_{ecl}$  cut for nominal branching ratios as described in the text. Second column: optimized FOM as a function of the assumed branching ratio. FOM for  $E_{ecl}$ , "square" and "triangular" cuts are shown.



(a) Generic MC:  $D_s \rightarrow \pi^0 \mu \nu$  decay

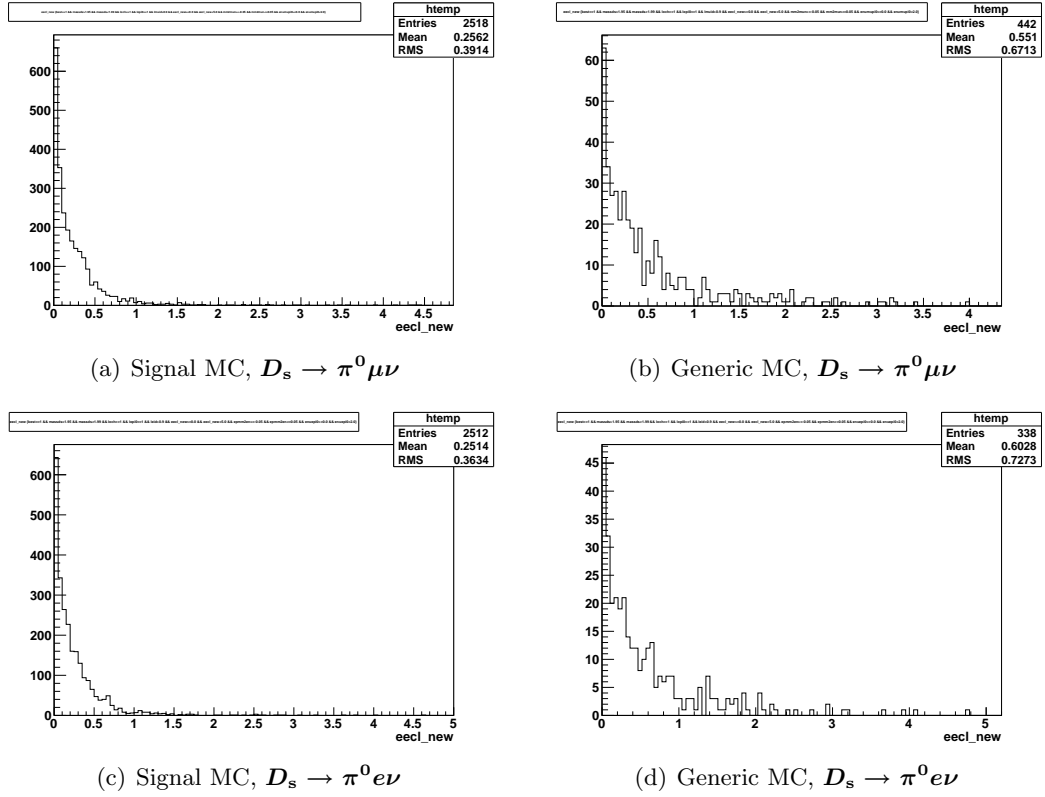
(b) Generic MC:  $D_s \rightarrow \pi^0 e \nu$  decay

FIGURE 3.6:  $MM^2$  for  $D_s \rightarrow \pi^0 l \nu$  decay, category specific color code given.

The  $MM^2$  distributions of  $D_s \rightarrow \pi^0 \mu \nu$  and for  $D_s \rightarrow \pi^0 e \nu$  decay with the best selection criteria are shown in Figs. 3.12 and 3.13.

The sources of background in  $D_s \rightarrow \pi^0 l \nu$  decay mode are obtained from the `dsdm` variable which stores different values for different  $D_s$  decay modes. For  $D_s \rightarrow \pi^0 \mu \nu$  decay mode, the dominant backgrounds come from:

- mode 2:  $\tau^+ \nu_\tau$
- mode 12:  $\eta \mu^+ \nu_\mu$ .
- mode 18:  $\bar{K}^0 K^+$

FIGURE 3.7:  $E_{ecl}$  distribution for  $D_s \rightarrow \pi^0 l \nu$  decay

The dominant background modes in  $D_s \rightarrow \pi^0 e \nu$  are:

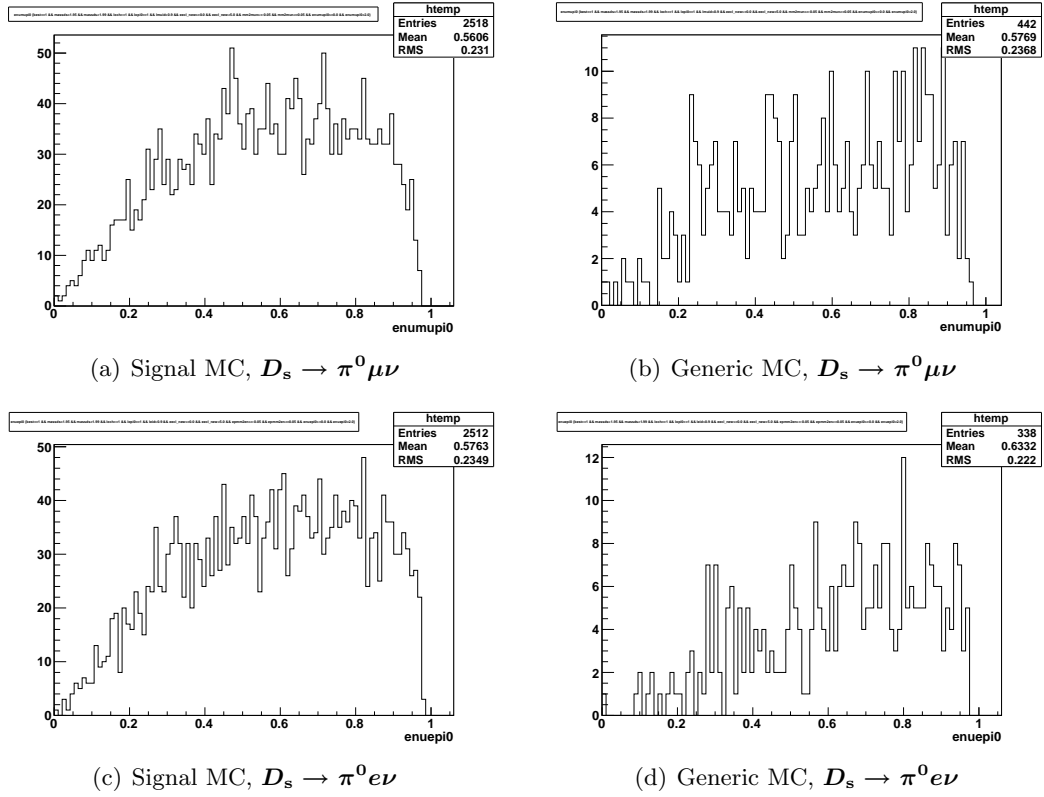
- mode 2:  $\tau^+ \nu_\tau$
- mode 5:  $D_s \rightarrow \eta e^+ \nu_e$

The distributions of the  $d_{sdm}$  variables for  $\pi^0 l \nu$  decays are shown in Fig. 3.14. The effect of the  $(E_{ecl}, E_\nu)$  cuts is shown on the  $d_{sdm}$  distributions.

### 3.6.2 Fit procedure.

A binned maximum likelihood fit to the  $MM^2$  distribution is performed. The signal fitting function used in signal MC sample is the sum of a Crystal Ball function and two Gaussian functions,

$$f_s(MM^2) = N(f_1 C(MM^2; m_0, \sigma, \alpha, n) + f_2 G_1(MM^2; \mu_1, \sigma_1) + (1 - f_1 - f_2) G_2(MM^2; \mu_2, \sigma_2)) \quad (3.9)$$

FIGURE 3.8:  $E_\nu$  distribution for  $D_s \rightarrow \pi^0 l \nu$  decay

The parameter  $N$  determines the signal yield. The background for the  $\pi^0$  channel is polynomial

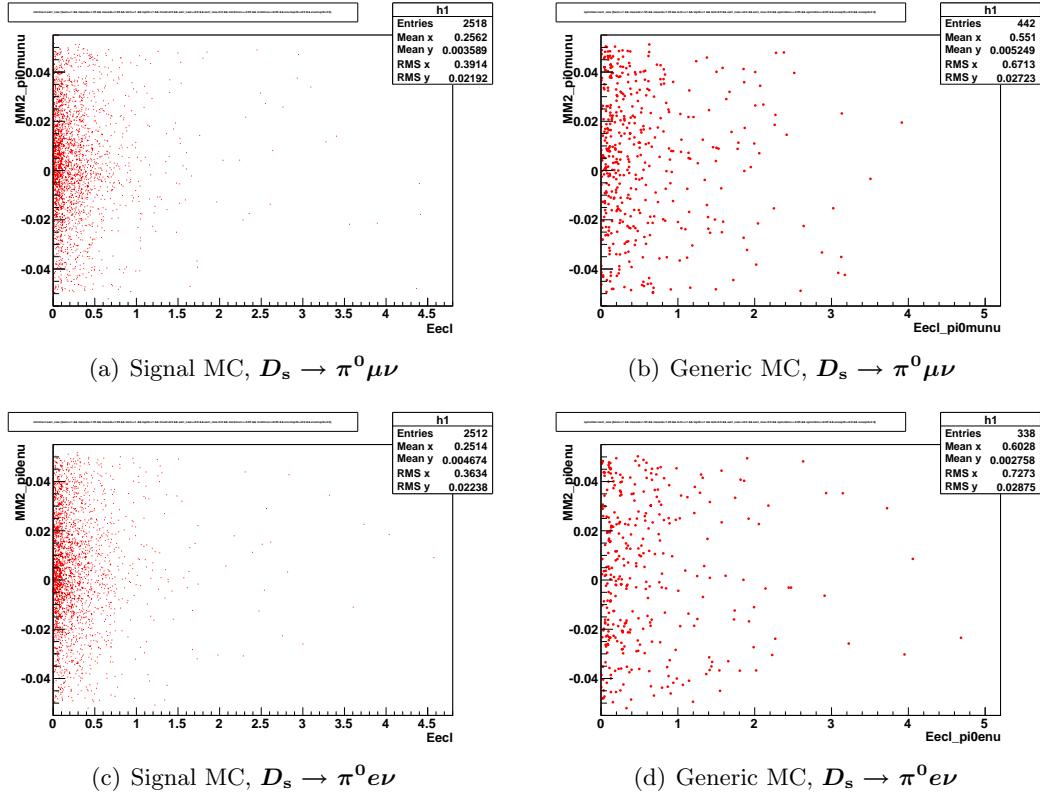
$$f_B(MM^2) = \sum_i a_i (MM^2)^i \quad (3.10)$$

### Muon mode:

The fit result with signal MC sample and  $f_s$  only is shown in Fig. 3.15, left. The fit result of the  $MM^2$  distribution with the Generic MC samples, obtained using the fixed  $f_s(MM^2)$  from the signal MC and a linear background, is shown in Fig. 3.15, right.

### Electron mode:

In this case, the background shape did not fit well with a polynomial. While  $f_s$  was used as before, the PDF of the background is represented by the sum of a Crystal ball (not centered at zero) and a Landau function. The fit results are shown in Fig. 3.16.

FIGURE 3.9:  $MM^2$  vs.  $E_{ecl}$  for  $D_s \rightarrow \pi^0 l \nu$  decay

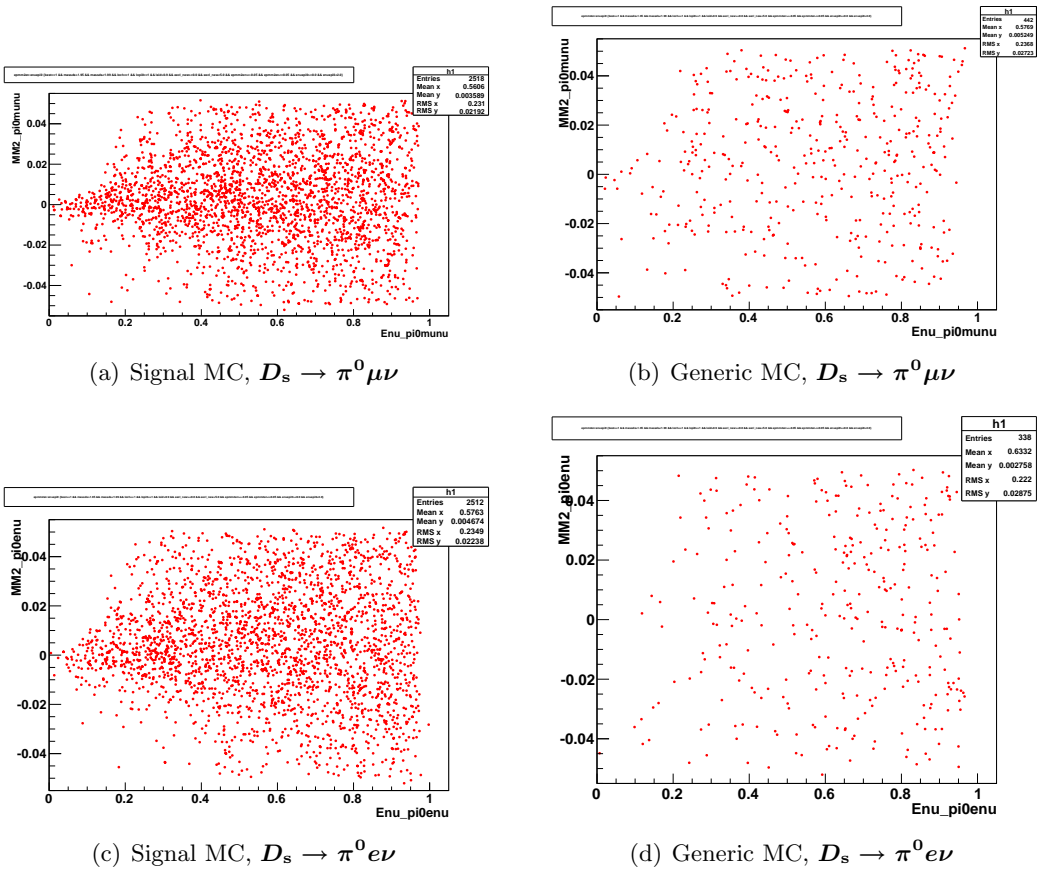
### Summary of MC analysis.

From the binned maximum likelihood fit to  $MM^2$  in six streams of Generic MC samples, we obtain a signal yield as:  $N_s = 115.38 \pm 29.67$  in the muon channel.

The number of inclusive  $D_s$  candidates in six streams of Generic Monte Carlo is  $1200969 \pm 5048.58$  as mentioned in subsection 3.4.1 and the efficiency of the exclusive decay of  $D_s \rightarrow \pi^0 \mu \nu$  in Signal MC defined as  $\epsilon_{sigMC}$  is 0.0575. Using these numbers we estimate that the irreducible backgrounds correspond to a branching ratio of  $1.67 \pm 0.43 \times 10^{-3}$ .

We do a similar estimation of the upper limit on the branching ratio of  $D_s \rightarrow \pi^0 e \nu$  channel and in that case the signal yield in six streams of Generic MC is  $N_s = 78.96 \pm 27.49$  and the  $\epsilon_{sigMC} = 0.0615$  produce a branching ratio in Monte Carlo to be  $0.97 \pm 0.34 \times 10^{-3}$ .

The quoted statistical error in the MC produces a source of systematics through background subtraction in the data, which is of the order of  $0.4 \times 10^{-3}$ . It is noted that the major sources of background are known [55] to 6% ( $\tau \nu$ ) and 11% ( $\eta l \nu$ ), and variation of the branching ratios will produce further systematics.

FIGURE 3.10:  $MM^2$  vs.  $E_\nu$  for  $D_s \rightarrow \pi^0 l \nu$  decay

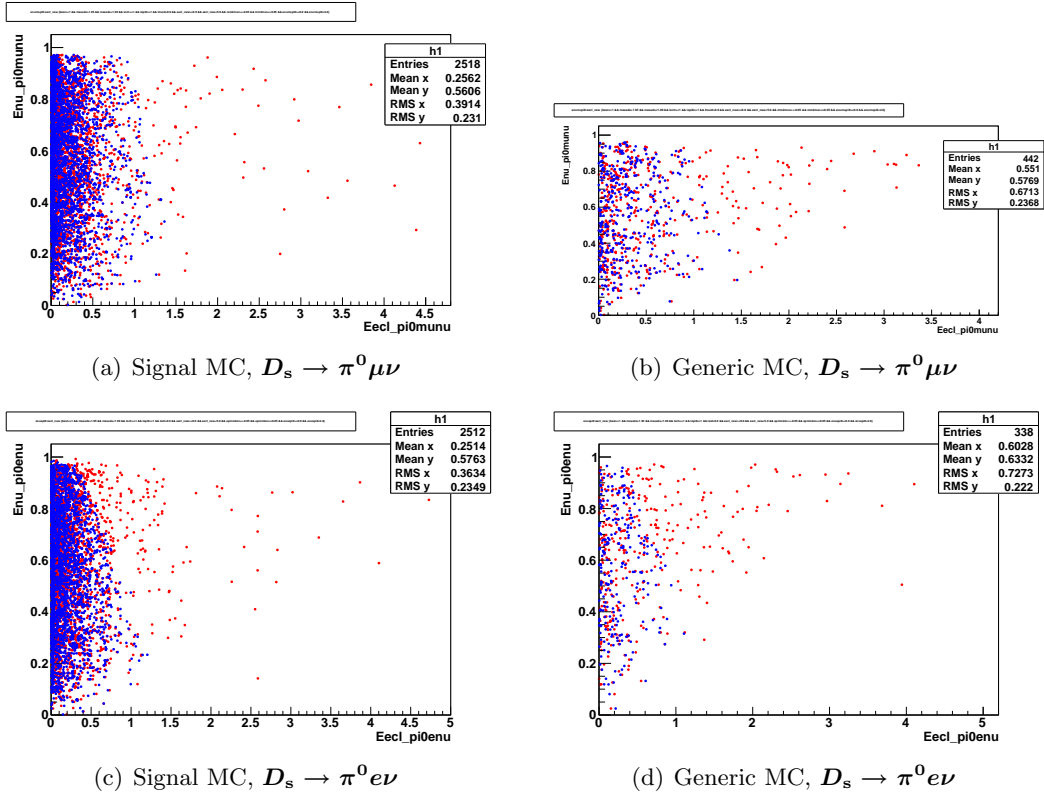


FIGURE 3.11:  $E_\nu$  vs.  $E_{ecl}$  for  $D_s \rightarrow \pi^0 l \nu$  decay, Blue Markers: for the events selected with Best ( $E_{ecl}, E_\nu$ ) Selection Criteria.

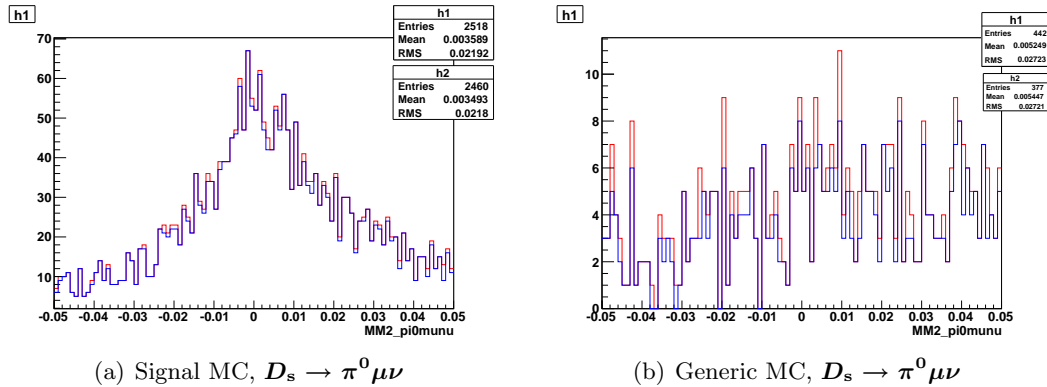


FIGURE 3.12:  $MM^2$  distribution for  $D_s \rightarrow \pi^0 l \nu$  decay. Blue line: optimal ( $E_{ecl}, E_\nu$ ) cuts. Red line: no ( $E_{ecl}, E_\nu$ ) cuts.



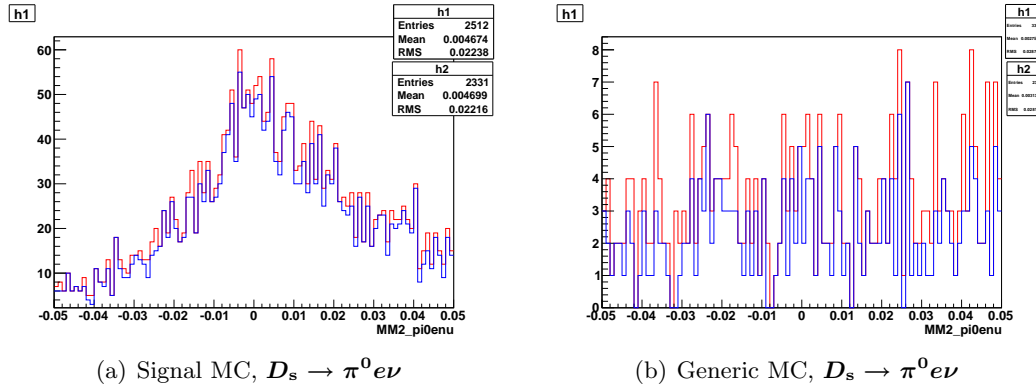


FIGURE 3.13:  $MM^2$  distribution for  $D_s \rightarrow \pi^0 e \nu$  decay. Blue line: optimal  $(E_{ecl}, E_\nu)$  cuts. Red line: no  $(E_{ecl}, E_\nu)$  cuts

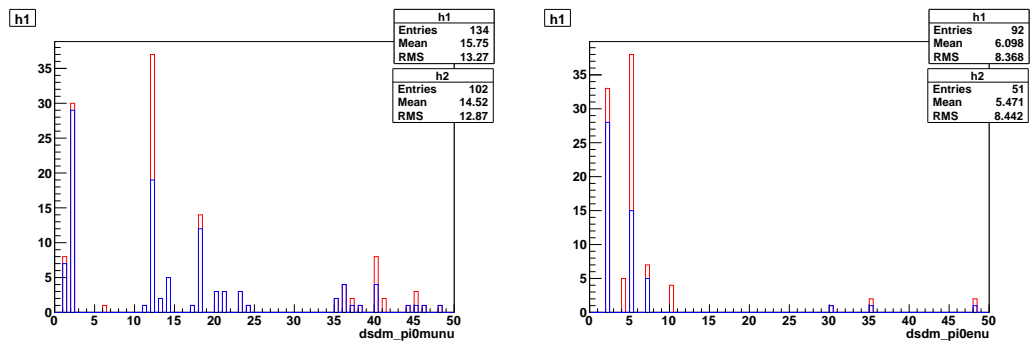


FIGURE 3.14:  $dsdm$  distributions in generic MC backgrounds for  $D_s \rightarrow \pi^0 \mu \nu$ . Blue line: optimal  $(E_{ecl}, E_\nu)$  cuts. Red line: no  $(E_{ecl}, E_\nu)$  cuts.

FIGURE 3.14:  $dsdm$  distributions in generic MC backgrounds for  $D_s \rightarrow \pi^0 \mu \nu$ . Blue line: optimal  $(E_{ecl}, E_\nu)$  cuts. Red line: no  $(E_{ecl}, E_\nu)$  cuts.

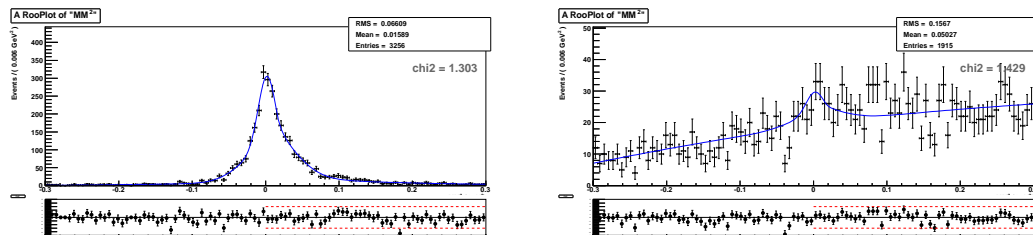
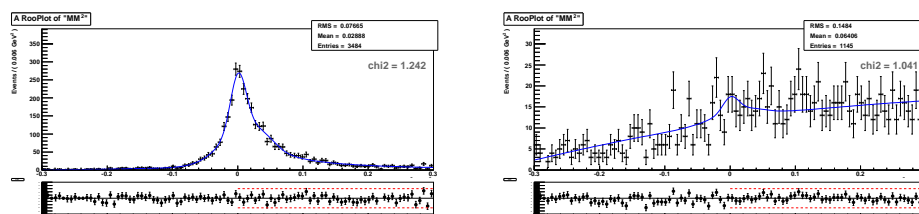


FIGURE 3.15: Fit to the  $MM^2$  distribution in the  $\pi^0 \mu \nu$  channel.

(a) Signal MC fit to  $MM^2$ , using only  $f_s$ .(b) Gen. MC fit to  $MM^2$ . The signal function is obtained from the signal MC sample, plus a background shape as described in the text.FIGURE 3.16: Fit to  $MM^2$  distribution for  $\pi^0 e \nu$  candidates

### 3.7 $D_s \rightarrow \rho l \nu$ analysis.

Further  $\rho l \nu$  signal selection is as follows:

1.  $|M_{\pi\pi} - M_\rho| < 150$  MeV, where  $M_\rho$  is the nominal mass [55].

The selections of the  $\pi^\pm$  candidates which are the daughters of the  $\rho$  are the same as mentioned in subsection 3.1.1.

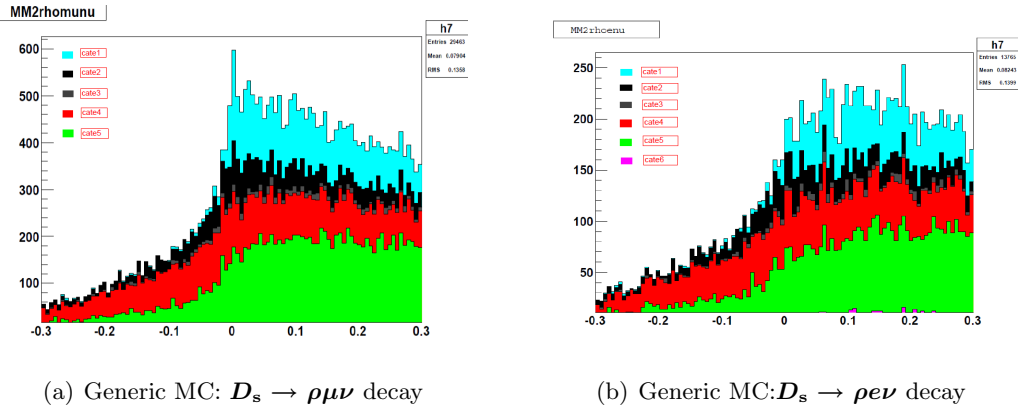


FIGURE 3.17:  $MM^2$  for  $D_s \rightarrow \rho l \nu$  decay, category specific color code given

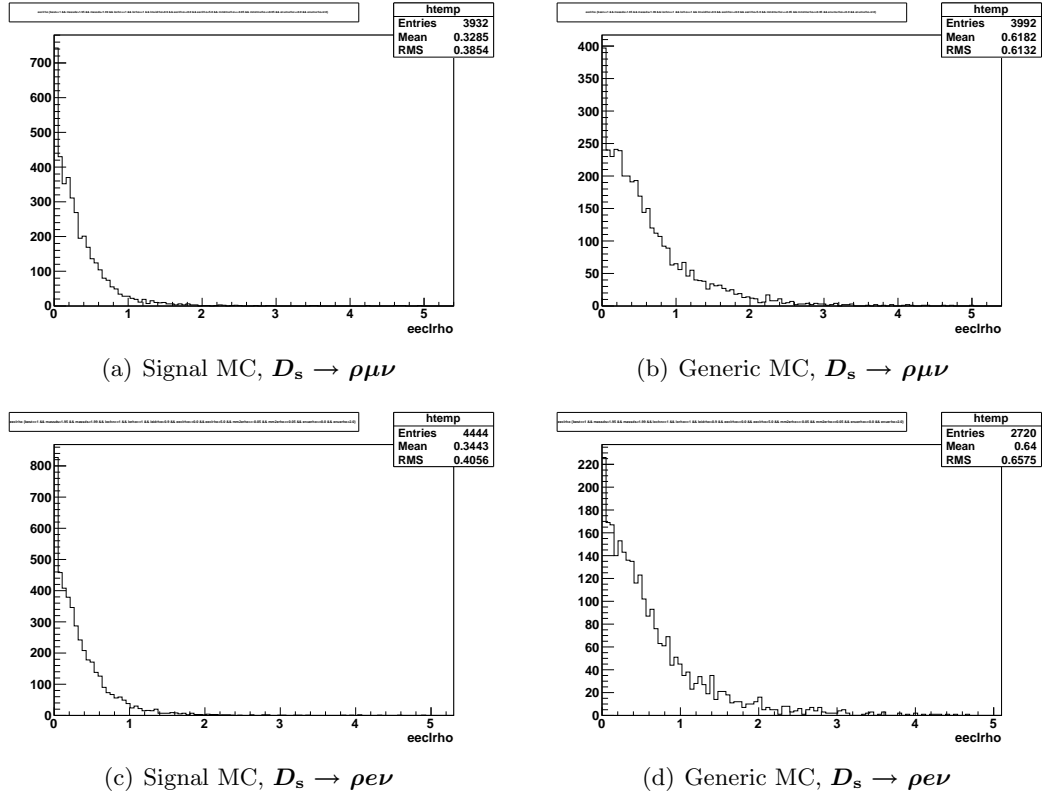
#### 3.7.1 MC analysis.

The  $MM^2$  distributions for  $D_s \rightarrow \rho \mu \nu$  and  $D_s \rightarrow \rho e \nu$  decays in Generic MC represent in Fig. 3.17 the background which are generated from correctly reconstructed inclusive  $D_s$  using category 1: true signal and the background events for each of the other five categories (described in section 3.3).

The one dimensional  $E_{ecl}$  distributions for  $D_s \rightarrow \rho \mu \nu$  decays are shown in Fig. 3.18, and the  $E_\nu$  distributions are in Fig. 3.19.

Fig. 3.20 through Fig. 3.22 illustrate the two dimensional scatter plots for  $D_s \rightarrow \rho \mu \nu$  and  $D_s \rightarrow \rho e \nu$  decays. The best  $(E_{ecl}, E_\nu)$  cuts for this analysis are mentioned in Table 3.4.

Along with the best  $(E_{ecl}, E_\nu)$  cuts, in the  $\rho$  modes, we observed in the Gen MC large backgrounds coming from  $D_s \rightarrow \phi l \nu$  and  $D_s \rightarrow \eta' l \nu$ . The former background decays into  $\pi^+ \pi^- \pi^0$  15.5% of the time, and the latter decays into  $\rho^0 \gamma$  29.1% of the time [55]. We sought to reduce these backgrounds, and we look for extra  $\pi^0$  and  $\gamma$  in the signal hemisphere, which have not been used in the event reconstruction. Then we reconstruct

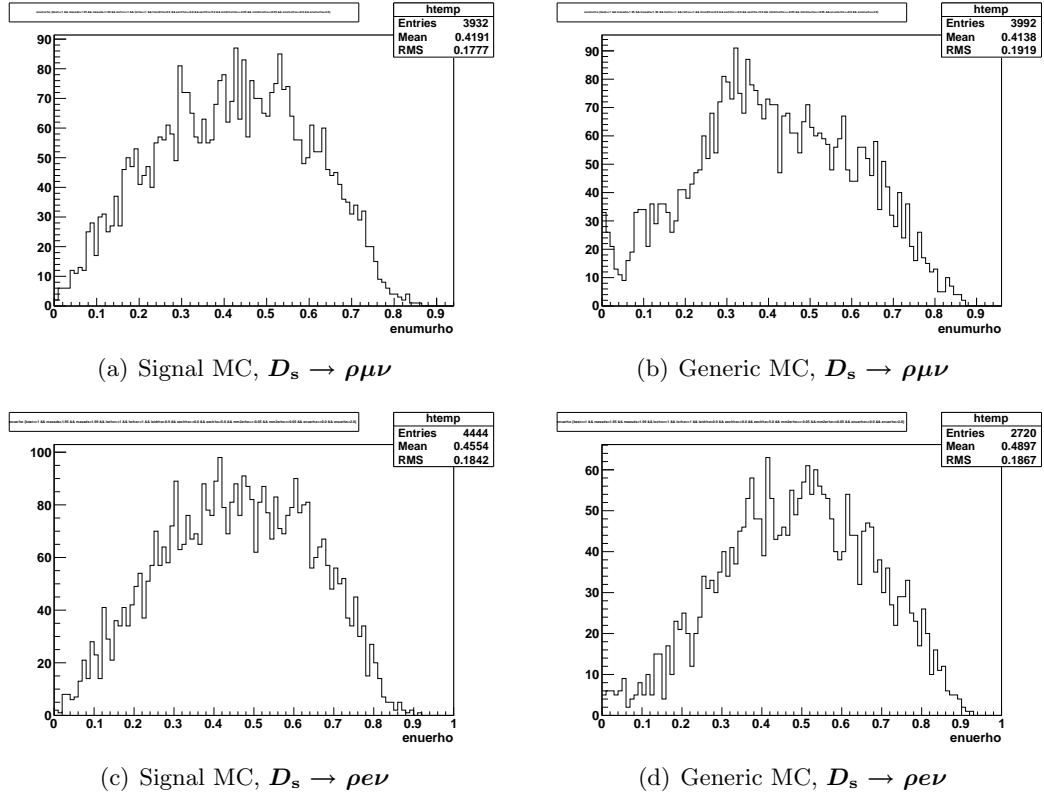
FIGURE 3.18:  $E_{ecl}$  distribution for  $D_s \rightarrow \rho l \nu$  decay

the invariant mass distribution of  $M_{\pi^+\pi^-\pi^0}$ . But we do not find a significant peak in the  $M_{\pi^+\pi^-\pi^0}$  distribution in signal and generic MC. So we have decided not to use  $M_{\pi^+\pi^-\pi^0}$  in the calculation of the FOM in the  $D_s \rightarrow \rho l \nu$  modes. We also reconstruct an invariant mass of  $M_{\pi^+\pi^-\gamma}$  and veto events with  $0.938 < M_{\pi^+\pi^-\gamma} < 0.978$  GeV. The invariant mass distributions of  $M_{\pi^+\pi^-\pi^0}$  and  $M_{\pi^+\pi^-\gamma}$  are shown in Fig. 3.23 and Fig. 3.24.

The  $MM^2$  distributions of exclusive  $D_s \rightarrow \rho \mu \nu$  decay and for  $D_s \rightarrow \rho e \nu$  decay within the inclusive sample of  $D_s$  are plotted in signal MC and six streams of generic MC in Figs. 3.25 and 3.26 using the best selection criteria listed above.

Fig. ?? shows the FOM main characteristics. In the first column, the dependence of FOM on the  $E_{ecl}$  cut is shown, for the nominal  $\mathcal{B}_l$ . The second column shows the dependence of the optimal FOM on the branching ratio  $\mathcal{B}$  for  $E_{ecl}$  cuts alone, square and slanted ( $E_{ecl}, E_\nu$ ) cuts. There is a significant improvement for  $\rho \mu \nu$ , but there is only modest improvement for  $\rho e \nu$ . Since the  $\rho e \nu$  GEN MC sample is low statistics, we chose not to apply this cut in the electron channel.

The backgrounds in  $D_s \rightarrow \rho l \nu$  decay mode are obtained by looking at the  $dsdm$ . Most of the background events for  $D_s \rightarrow \rho \mu \nu$  decay are coming from:

FIGURE 3.19:  $E_\nu$  distribution for  $D_s \rightarrow \rho l \nu$  decay

- mode 13:  $\eta' \mu^+ \nu_\mu$ ,
- mode 45:  $\eta' \pi^+$ ,

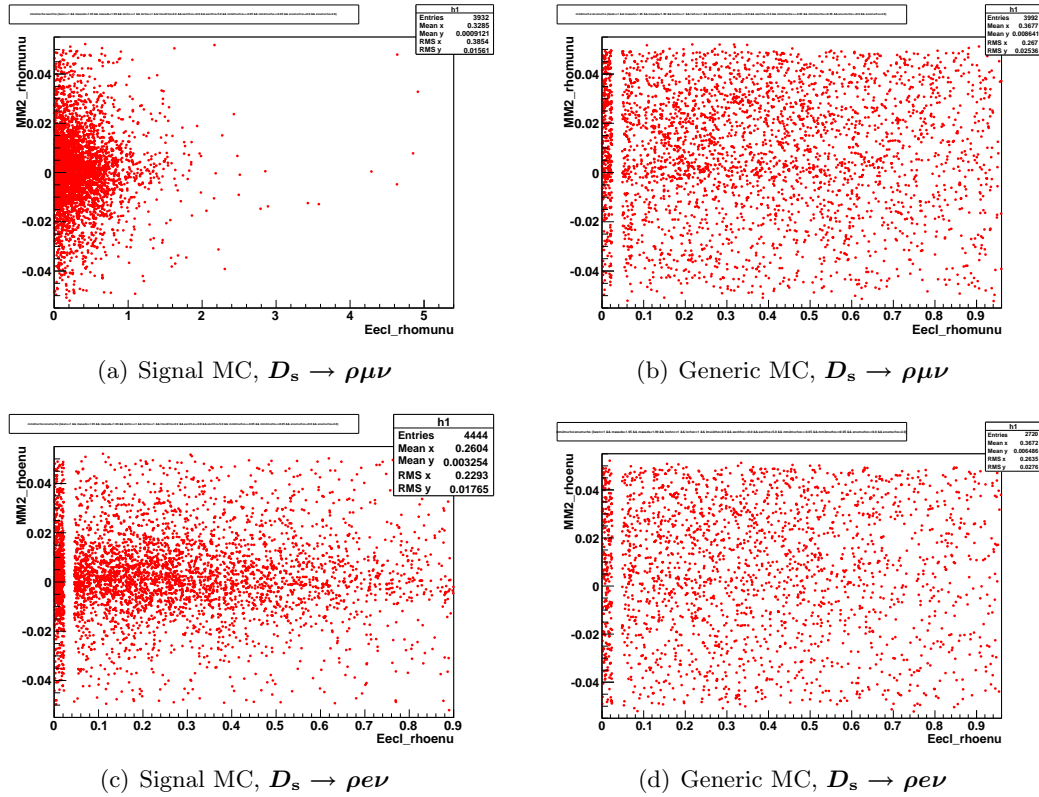
In Fig. 3.25, we identify the peak in  $D_s \rightarrow \rho\mu\nu$  (in blue: with the optimal  $(E_{ecl}, E_\nu)$  cuts) near  $MM^2 = 0$  to be coming from mode 13 and mode 45. The  $d_{sdm}$  distribution for  $-0.05 < MM^2 < 0.05$  is shown in Fig. 3.28. The effect of  $(E_{ecl}, E_\nu)$  cut is shown on the  $D_s \rightarrow \rho\mu\nu$  decay mode.

The dominant background mode in  $D_s \rightarrow \rho e\nu$  is

- mode 6:  $\eta' e^+ \nu_e$ .

For  $D_s \rightarrow \rho e\nu$  decay mode we don't apply any signal side cut.

The signal fitting function to fit the  $MM^2$  distributions for  $D_s \rightarrow \rho l \nu$  in signal MC is done using  $f_s$  [Subsect. 3.6.2] and the background is a sum of a Crystal ball function and a Landau function.

FIGURE 3.20:  $MM^2$  vs.  $E_{ecl}$  for  $D_s \rightarrow \rho l\nu$  decay.**Muon mode:**

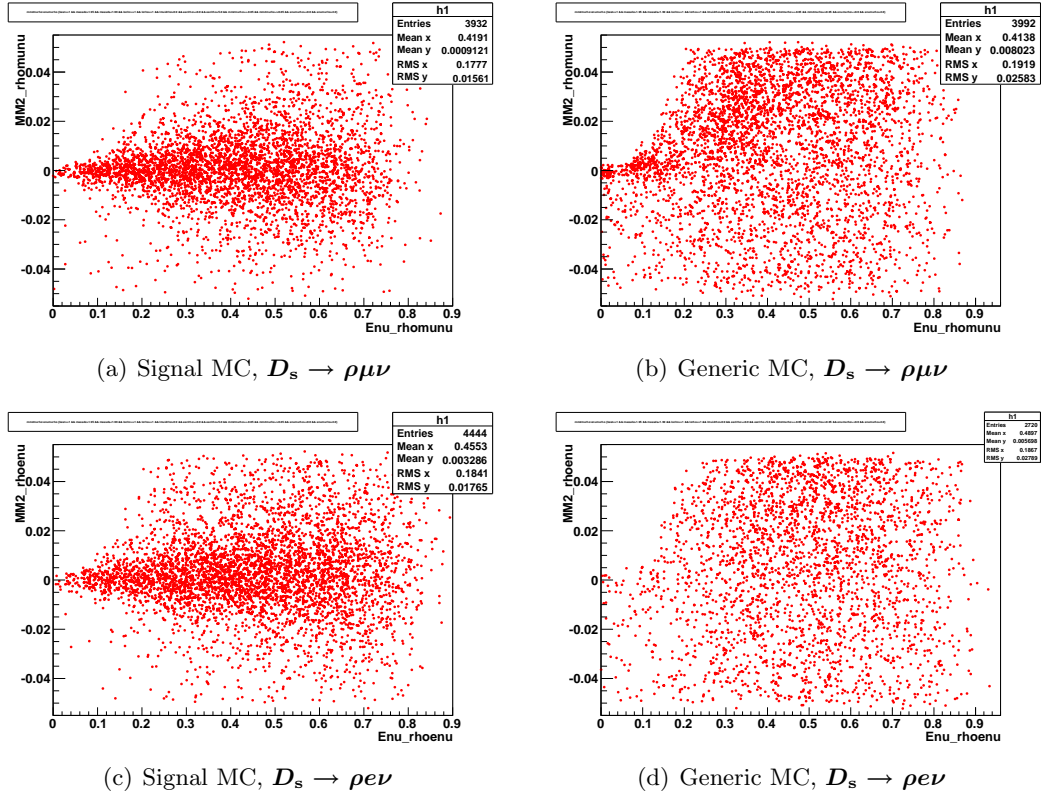
The fit is shown in Fig. 3.31 and 3.32. A peaking structure remains, which is an irreducible background.

**Electron mode:**

The fits is shown in Fig. 3.31 and 3.32.

**Summary of MC analysis.**

In  $D_s \rightarrow \rho\mu\nu$  mode we find a Signal MC efficiency of 0.0559 and number of exclusively reconstructed  $D_s \rightarrow \rho\mu\nu$  events in six streams of Generic MC to be  $397.97 \pm 31.37$ . Using these numbers we calculate a branching ratio of  $D_s \rightarrow \rho\mu\nu$  decay in Monte Carlo:  $5.67 \pm 0.45 \times 10^{-3}$ . Similarly for  $D_s \rightarrow \rho e\nu$  decay, the signal efficiency is 0.0762 and the number of exclusively reconstructed  $D_s \rightarrow \rho e\nu$  events in six streams of Generic MC is  $189 \pm 34.17$ , which provide us with an estimation of the branching ratio in Monte Carlo:  $1.99 \pm 0.36 \times 10^{-3}$ .

FIGURE 3.21:  $MM^2$  vs.  $E_\nu$  for  $D_s \rightarrow \rho l\nu$  candidates

The quoted statistical error in the MC produces a source of systematics through background subtraction in the data, which is of the order of  $0.4 \times 10^{-3}$ . It is noted that the major sources of background are known [55] to 6% ( $\tau\nu$ ) and 23% ( $\eta l\nu$ ), and variation of the branching ratios will produce further systematics. The  $f_0 l\nu$  background, which is absent in the generic MC and is currently measured at  $(2.00 \pm 0.32) \times 10^{-3}$ , will also need to be subtracted and its error convoluted with other errors. Looking at these estimated results we have decided to discard the  $\rho\mu\nu$  mode statistics, due to the strongly peaking background.

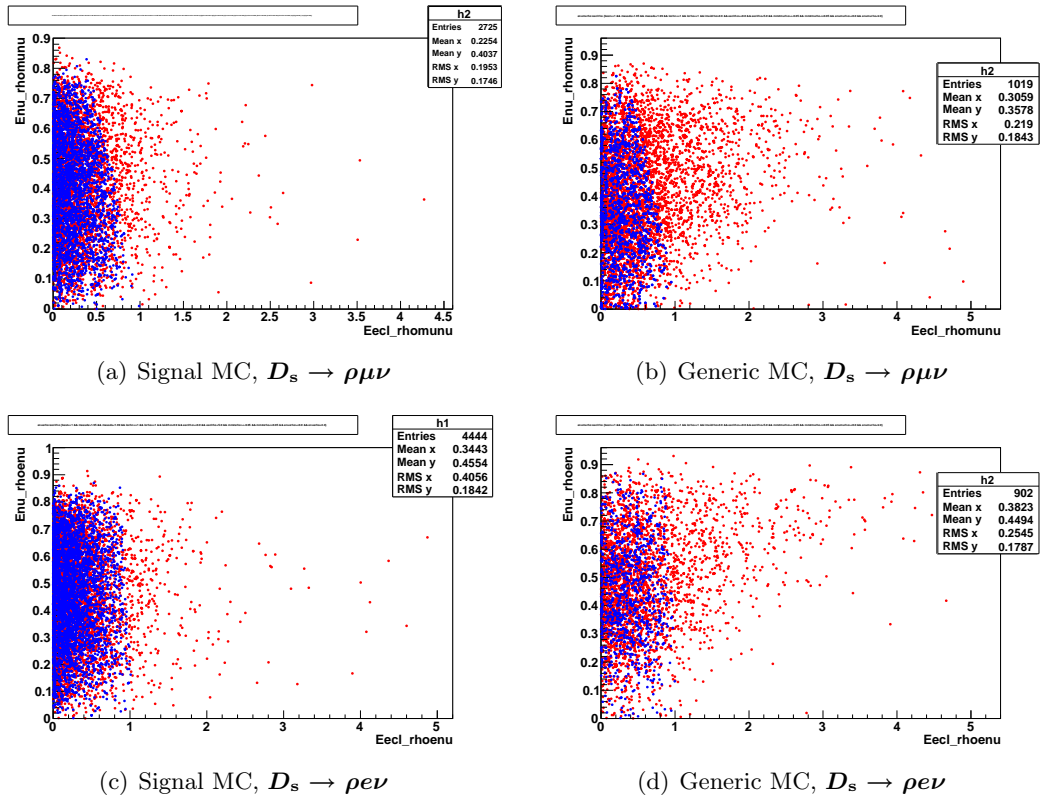


FIGURE 3.22:  $E_\nu$  vs.  $E_{ecl}$  for  $D_s \rightarrow \rho l \nu$  candidates. In  $D_s \rightarrow \rho\mu\nu$  mode: Blue Markers: for the events selected with Best  $(E_{ecl}, E_\nu)$  Selection Criteria

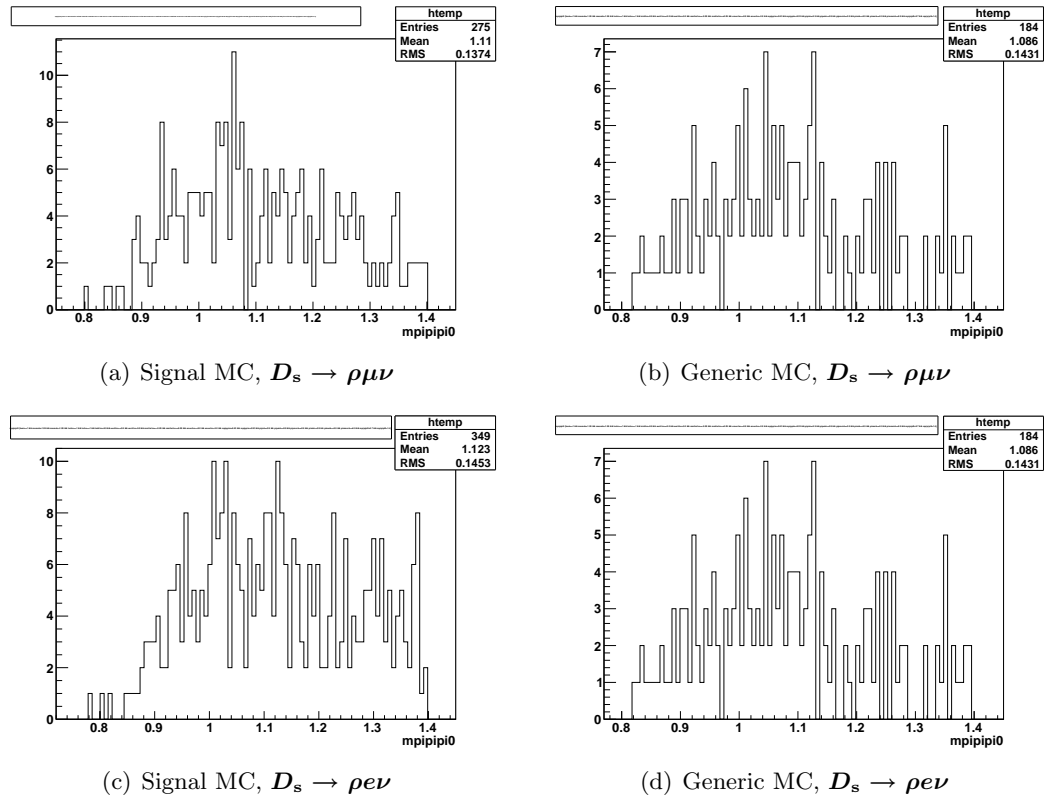
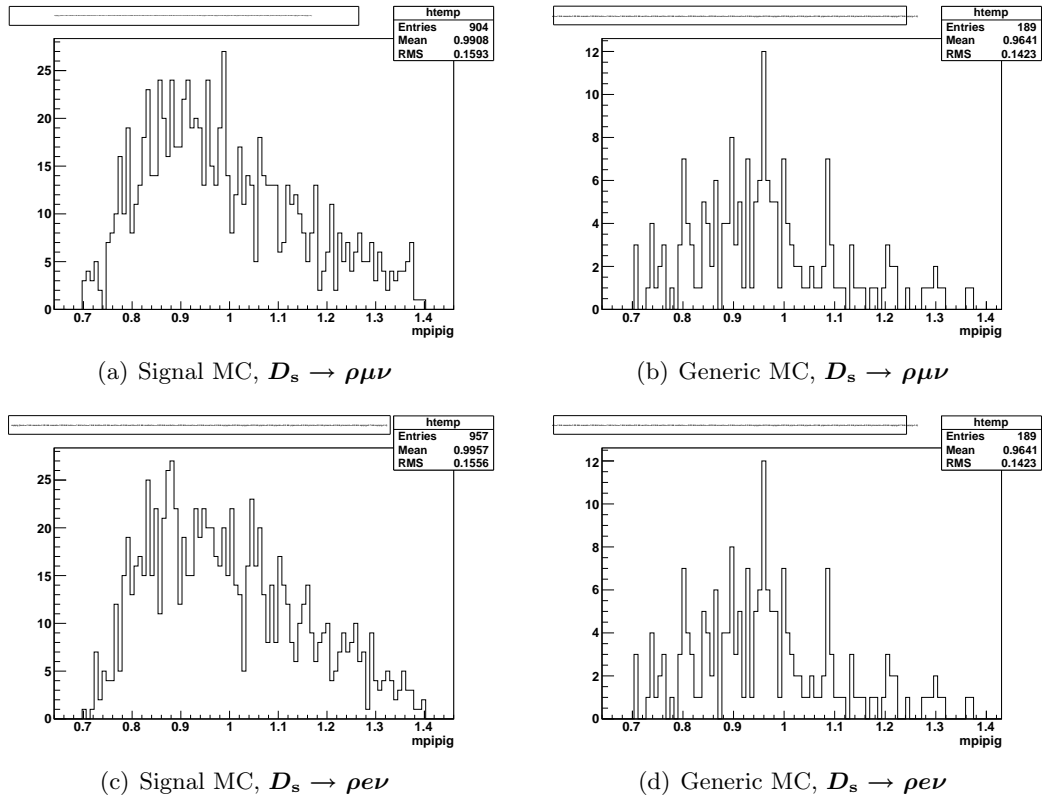
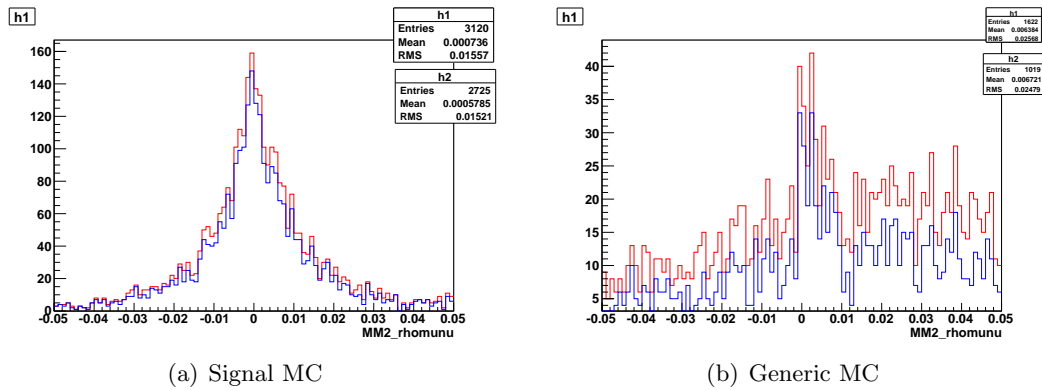


FIGURE 3.23:  $M_{\pi^+\pi^-\pi^0}$  for  $D_s \rightarrow \rho l \nu$  decay.



FIGURE 3.24:  $M_{\pi^+\pi^-\gamma}$  for  $D_s \rightarrow \rho\mu\nu$  decay.FIGURE 3.25:  $MM^2$  distribution for  $D_s \rightarrow \rho\mu\nu$  decay. Blue line: optimal  $(E_{ecl}, E_\nu)$  cuts. Red line: no  $(E_{ecl}, E_\nu)$  cuts

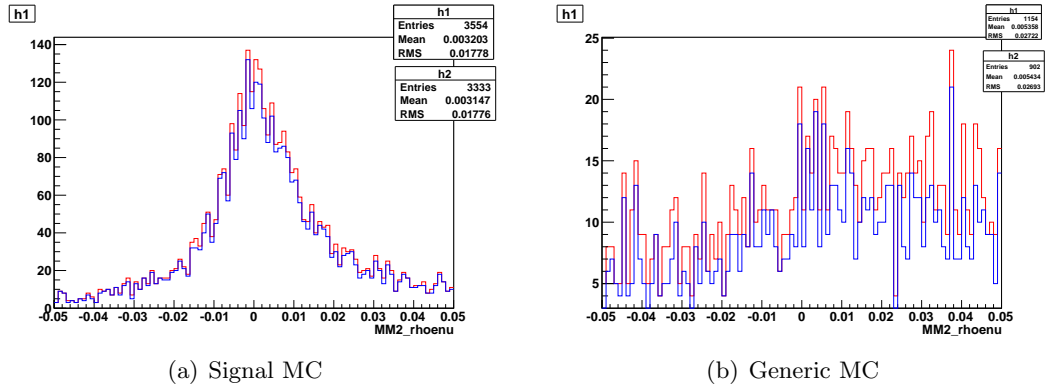


FIGURE 3.26:  $MM^2$  distribution of  $D_s \rightarrow \rho e \nu$  decay. no optimal  $(E_{ecl}, E_\nu)$  cut is applied.

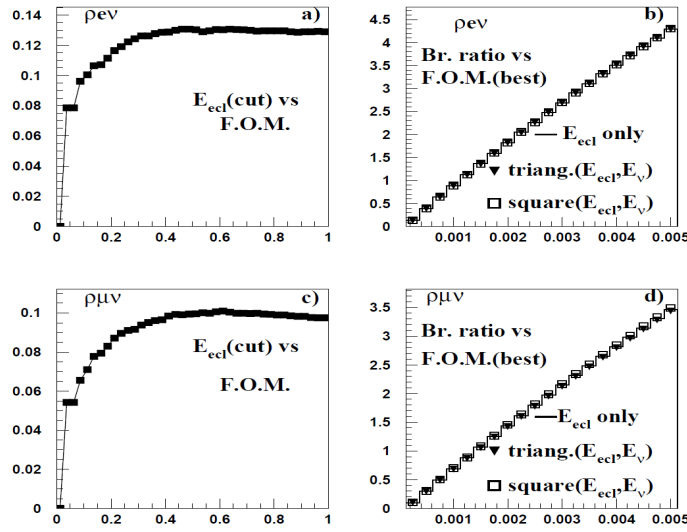


FIGURE 3.27: First row:  $D_s \rightarrow \rho e \nu$ , Second row:  $D_s \rightarrow \rho \mu \nu$ . First column: FOM versus  $E_{ecl}$  cut for nominal branching ratios as described in the text. Second column: optimized FOM as a function of the assumed branching ratio. FOM for  $E_{ecl}$ , “square” and “triangular” cuts are shown.

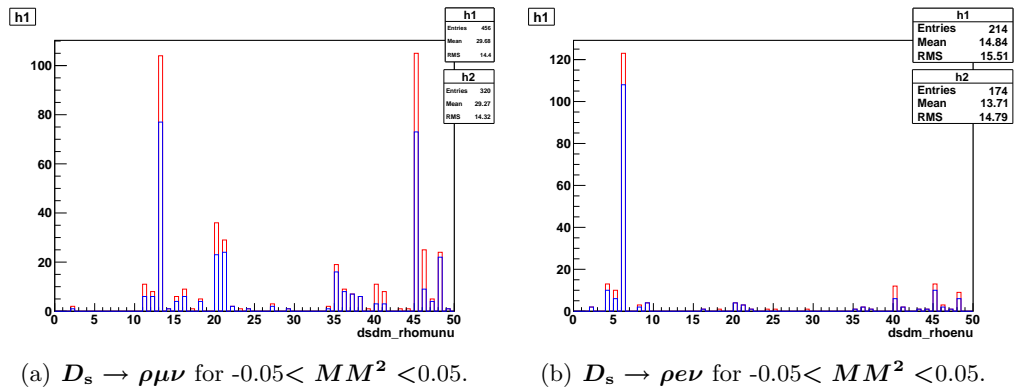


FIGURE 3.28: dsdm distributions for  $D_s \rightarrow \rho l \nu$  candidates in Generic MC. Blue line: optimal  $(E_{ecl}, E_\nu)$  cuts. Red line: No optimal  $(E_{ecl}, E_\nu)$  selection.

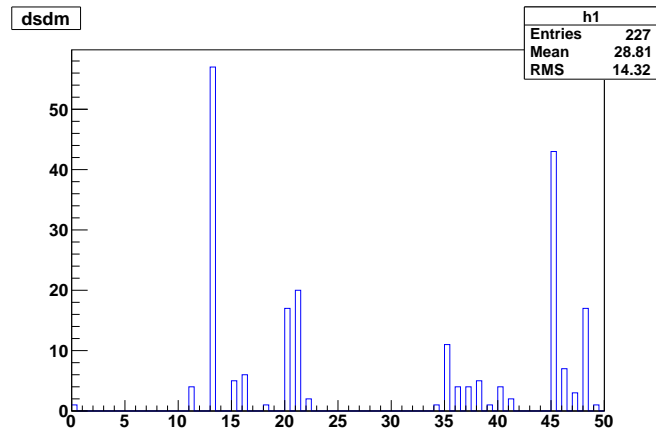
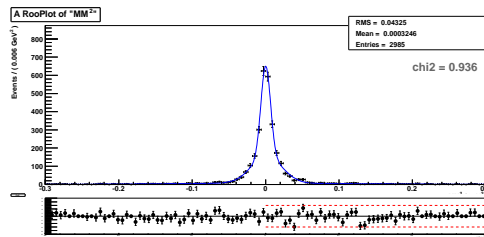
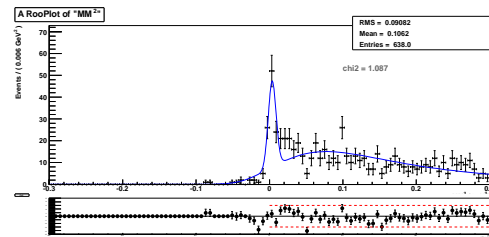


FIGURE 3.29: generic MC:  $dsdm$  distribution for  $D_s \rightarrow \rho\mu\nu$ , with optimal  $(E_{ecl}, E_\nu)$  for  $-0.05 < MM^2 < 0.05$ . Blue line: optimal  $(E_{ecl}, E_\nu)$  cuts. Red line: no  $(E_{ecl}, E_\nu)$  cuts.

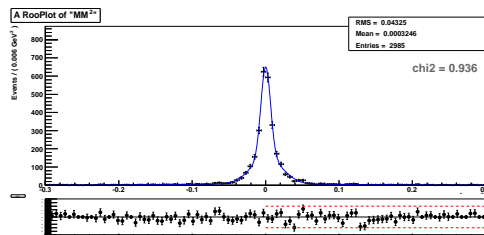


(a) Signal MC  $MM^2$ , using only  $f_s$  function.

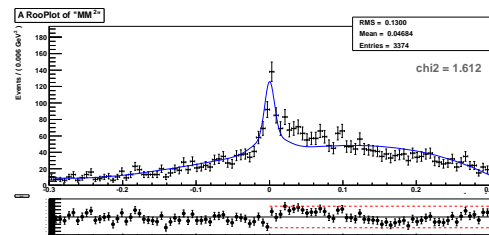


(b) Gen. MC  $MM^2$ , using the Signal MC  $f_s$  result and a background shape combining a Crystal ball and a Landau function.

FIGURE 3.30: Fit to  $MM^2$  distribution,  $D_s \rightarrow \rho\mu\nu$  candidates.

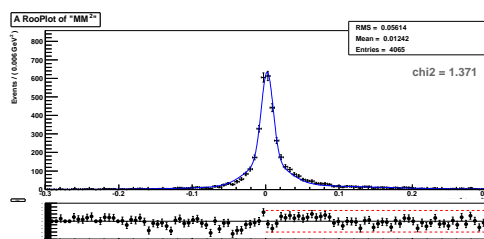
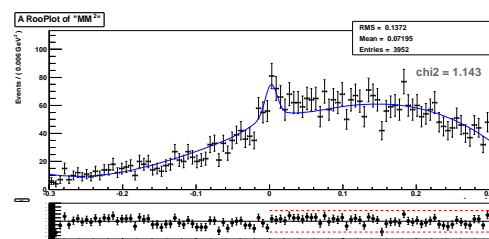


(a) Signal MC  $MM^2$ , using only  $f_s$  function.



(b) Gen. MC  $MM^2$ , using the Signal MC  $f_s$  result and a background shape of a cubic polynomial function.

FIGURE 3.31: Fit to  $MM^2$  distribution,  $D_s \rightarrow \rho\mu\nu$  candidates.

(a) Signal MC, using only  $f_s$ .(b) Gen. MC  $MM^2$ , using the Signal MC  $f_s$  result and a background shape of a cubic polynomial functionFIGURE 3.32: Fit to  $MM^2$  distribution,  $D_s \rightarrow \rho e \nu$  candidates.

### 3.8 $D_s \rightarrow K_s l \nu$ analysis.

$K_s$  signal selection is as follows.

1.  $|M_{\pi\pi} - M_{K_s^0}| < 20$  MeV
2. Vertex fit is performed

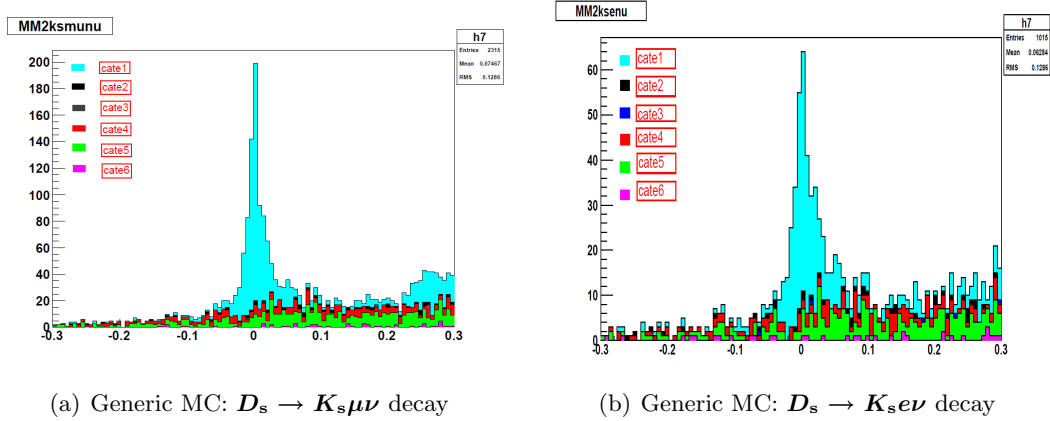


FIGURE 3.33:  $MM^2$  for  $D_s \rightarrow K_s l \nu$  decay, category specific color code given

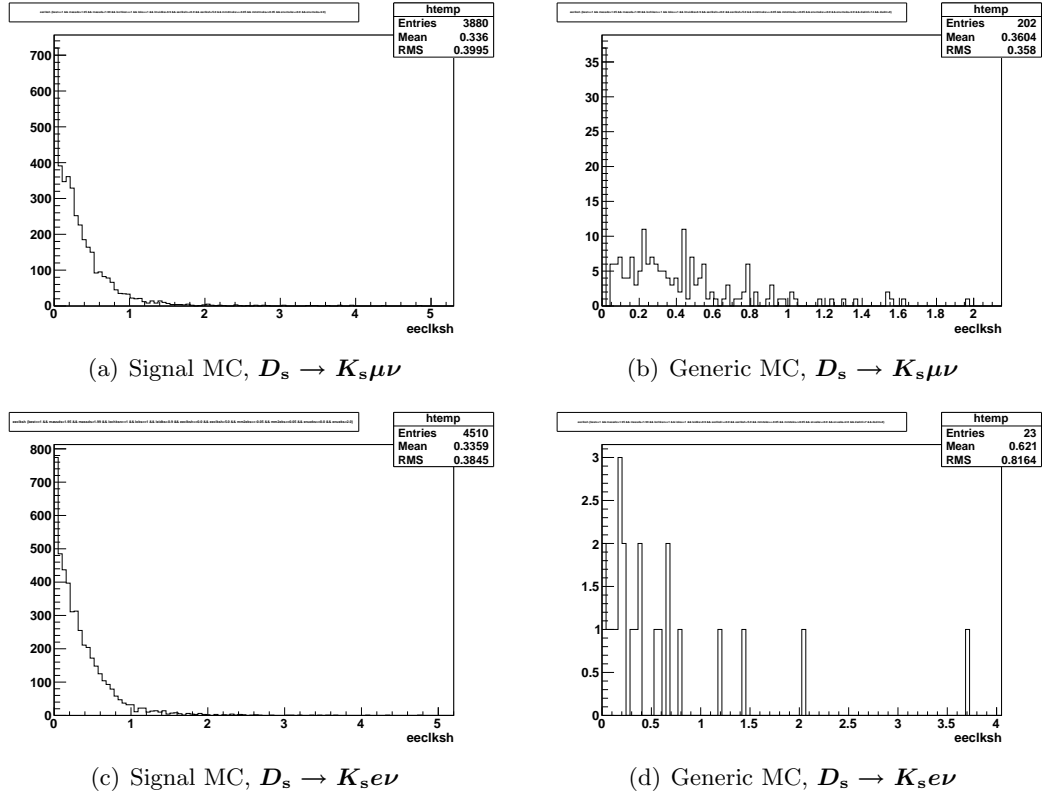
#### 3.8.1 MC analysis.

In the analysis of  $D_s \rightarrow K_s \mu \nu$  and  $D_s \rightarrow K_s e \nu$  decays using Generic MC we look at the background events present in the correctly reconstructed inclusive  $D_s$  sample using category 1: true signal and the background events coming from each of the other five categories in Fig. 3.33. The inclusive  $MM^2$  distributions for  $D_s \rightarrow K_s l \nu$  and  $D_s \rightarrow K_s e \nu$  decays in Generic MC are in Fig. 3.33. Note the presence of a clear signal, since these decays are present in GENMC.

The one dimensional  $E_{ecl}$  distributions for  $D_s \rightarrow K_s l \nu$  decays are shown in Fig. 3.34, and the  $E_\nu$  distributions are in Fig. 3.35.

In this analysis, the generic MC contains the signal with a branching ratio of  $3.7 \times 10^{-3}$ . We present fit results with and without the signal mode, and also cross check our analysis chain by measuring the branching ratio in the MC.

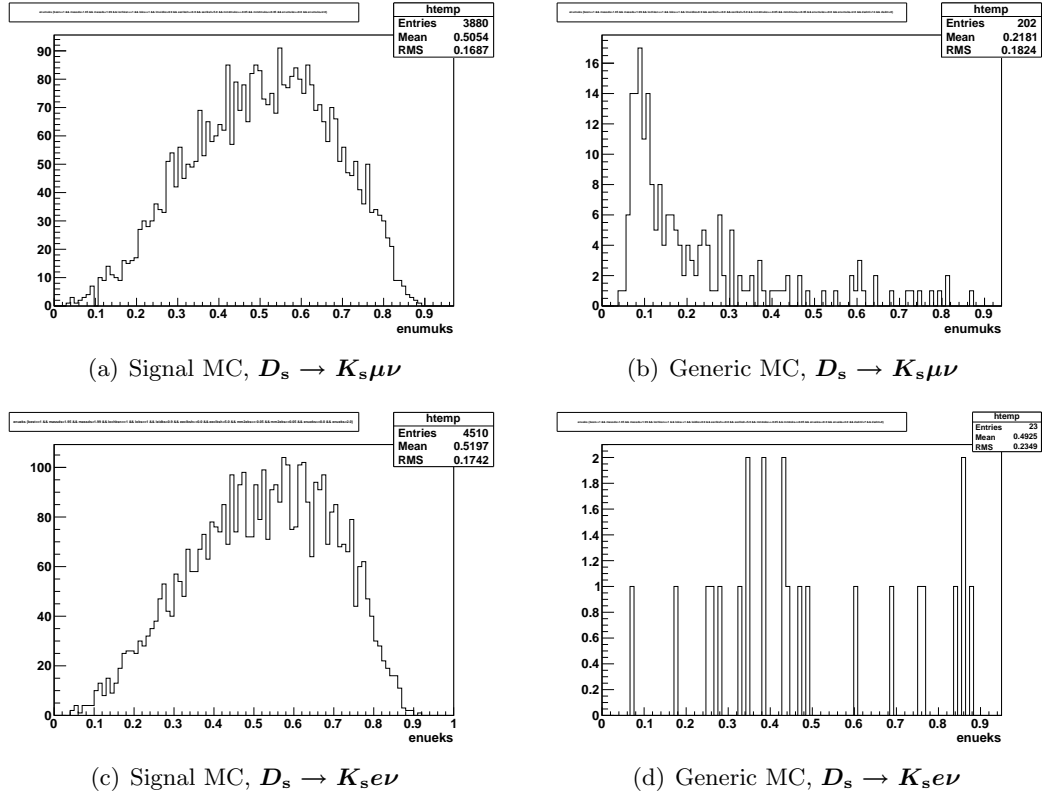
For  $D_s \rightarrow K_s \mu \nu$  and  $D_s \rightarrow K_s e \nu$  decays the two dimensional scatter plots are displayed in Fig. 3.36 through Fig. 3.38. The optimal  $(E_{ecl}, E_\nu)$  cuts are presented in Table 3.4. The fit to  $MM^2$  distributions for  $D_s \rightarrow K_s l \nu$  have been performed the same way as described in Subsection 3.6.2. The signal fitting function used in signal

FIGURE 3.34:  $E_{ecl}$  distribution for  $D_s \rightarrow K_s l \nu$  decay

MC is defined as  $f_s$  and The signal present in the Generic MC (mode **14** :  $\bar{K}^0 \mu^+ \nu_\mu$  and mode **7** :  $\bar{K}^0 e^+ \nu_e$ ) is fitted with the sum of the  $f_s$  and a polynomial function, shown in Fig. 3.43 and in Fig. 3.44. The backgrounds for  $K_s \mu \nu$  candidates after taking off mode **14** are fitted with a Crystal ball added to a linear polynomial function. The backgrounds in  $K_s e \nu$  decay after taking off mode **7** are fitted with a Gaussian and a linear polynomial added to it. The background fits in  $K_s l \nu$  decay are shown in Fig. 3.45.

The  $MM^2$  distributions of exclusive  $D_s \rightarrow K_s \mu \nu$  decay after applying the best selection cut have been plotted in signal MC and six streams of generic MC and are shown in Fig. 3.39 and 3.40.

Fig. 3.41 shows the FOM main characteristics. In the first column, the dependence of FOM on the  $E_{ecl}$  cut is shown, for the nominal  $\mathcal{B}_l$ . The second column shows the dependence of the optimal FOM on the branching ratio  $\mathcal{B}$  for  $E_{ecl}$  cuts alone, square and slanted ( $E_{ecl}, E_\nu$ ) cuts. There is a significant improvement for  $K_s \mu \nu$ , but there is only modest improvement for  $K_s e \nu$ . Since the  $K_s e \nu$  GEN MC sample contained only 23 events, and optimal selection cuts only one, we chose not to apply this cut in the electron channel.

FIGURE 3.35:  $E_\nu$  distribution for  $D_s \rightarrow K_s l \nu$  decay

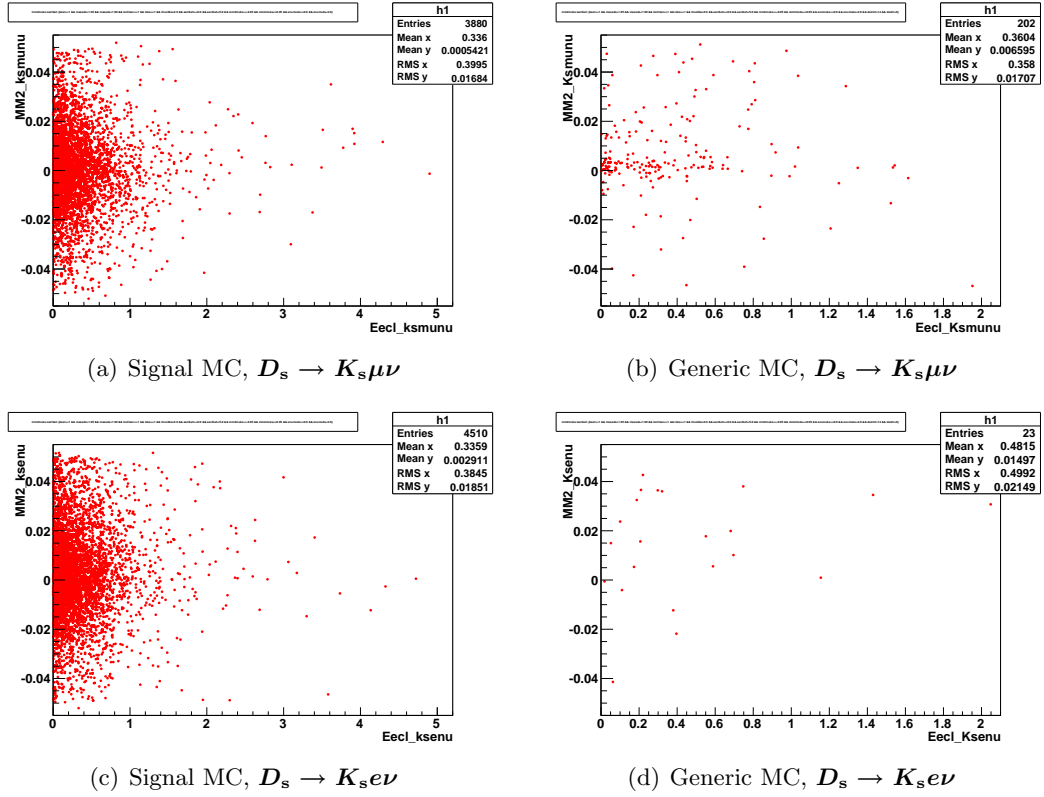
The sources of the backgrounds in  $D_s \rightarrow K_s l \nu$  decay mode is presented in terms of the `dsdm` variable as done in the previous two modes. Mode 7 and mode 14 correspond to  $\bar{K}^0 e^+ \nu_e$  and  $\bar{K}^0 \mu^+ \nu_\mu$  respectively and these are the signal modes present in Generic MC. The distributions of the `dsdm` variables for  $K_s l \nu$  decays are shown in Fig. 3.42. For  $D_s \rightarrow K_s \mu \nu$  decay, the dominant backgrounds are:

- mode 18:  $\bar{K}^0 K^+$
- mode 21:  $\bar{K}^{*0} K^+$
- mode 23:  $K^{*+} \bar{K}^0$

The dominant backgrounds in  $D_s \rightarrow K_s e \nu$  are

- mode 18:  $\bar{K}^0 K^+$

The effect of best  $(E_{ecl}, E_\nu)$  cut is shown on the  $D_s \rightarrow K_s \mu \nu$  decay only.

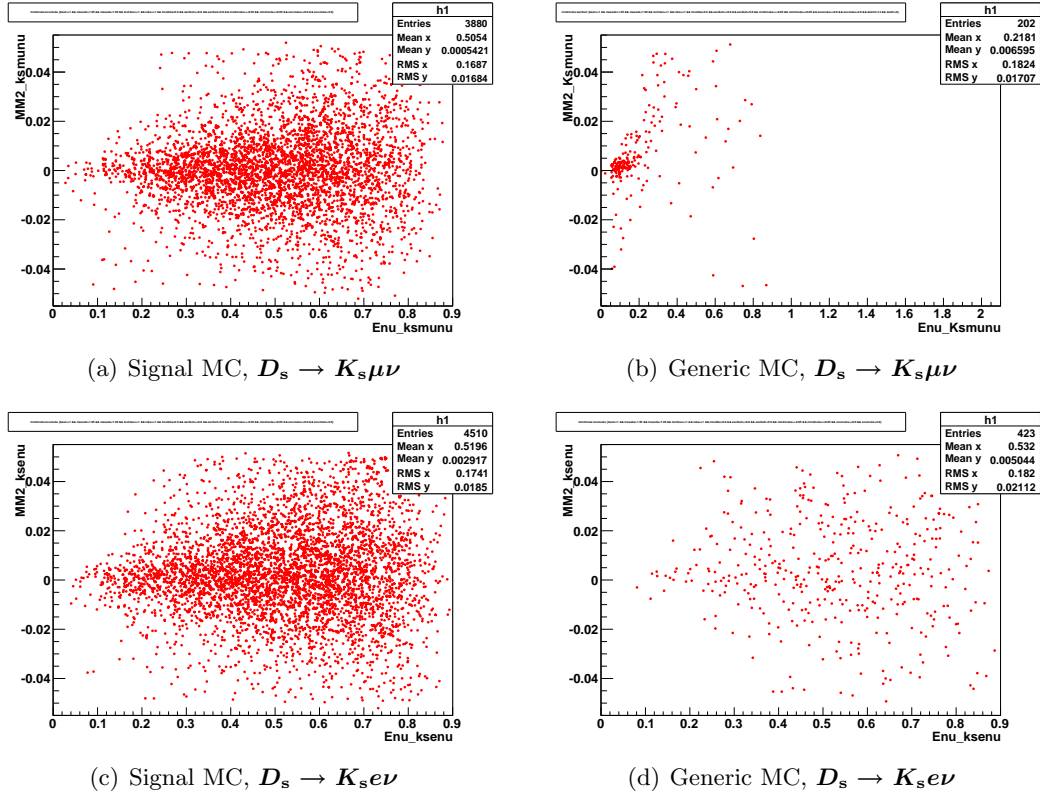
FIGURE 3.36:  $MM^2$  vs.  $E_{ecl}$  for  $D_s \rightarrow K_s l \nu$  decay.**Muon mode:**

The fit result of the  $MM^2$  distribution for  $D_s \rightarrow K_s \mu \nu$  decay with signal MC sample applying only  $f_s$  is shown in Fig. 3.43, left. Where Fig. 3.43, right, shows the fit result for the signal mode in the Generic MC sample: number 14: ( $\bar{K}^0 \mu^+ \nu_\mu$ ) and it is obtained using the fixed  $f_s(MM^2)$  from the signal MC sample and a quadratic background added to it.

**Electron mode:**

The fit result of the  $MM^2$  for  $D_s \rightarrow K_s e \nu$  decay with only  $f_s$  in signal MC sample is displayed in Fig. 3.44, left. The fit result for the signal mode in the Generic MC sample: number 7: ( $\bar{K}^0 e^+ \nu_e$ ) has been performed the same way as in the  $\mu$  mode, using the fixed  $f_s(MM^2)$  function obtained from the signal MC sample and a quadratic background added to it as shown in the Fig. 3.43, right.



FIGURE 3.37:  $MM^2$  vs.  $E_\nu$  for  $D_s \rightarrow K_s l \nu$  decay.

### Summary of MC analysis.

The  $K_s l \nu$  mode is peculiar because it allows us to both test the software for signal reconstruction (using modes 7 and 14) and also to measure the irreducible backgrounds (all other modes). In other words, we can assess both the robustness of our signal evaluation, and estimate a major source of systematic errors.

We discuss first the “signal” modes, by requesting that the events were originally mode 7 or 14. Effectively, this is a signal MC embedded in the Generic MC. We find a Signal MC efficiency of 0.0572 and number of exclusively reconstructed  $D_s \rightarrow K_s \mu \nu$  events in six streams of Generic MC to be  $288 \pm 8.8$ . Using these numbers we calculate a branching ratio of  $D_s \rightarrow K_s \mu \nu$  decay in Monte Carlo:  $(3.77 \pm 0.12) \times 10^{-3}$ . Similarly for  $D_s \rightarrow K_s e \nu$  decay, the signal efficiency is 0.0785 and the number of exclusively reconstructed  $D_s \rightarrow K_s e \nu$  events in six streams of Generic MC is  $373 \pm 14.7$ , which give the branching ratio of  $D_s \rightarrow K_s e \nu$  decay in Monte Carlo:  $(3.56 \pm 0.14) \times 10^{-3}$ . Based on these numbers and the nominal branching ratio, we estimate the combined Belle statistical error to be  $0.9 \times 10^{-4}$ .

For the background modes, the events must be neither mode 7 nor mode 14. We fit the background modes (excluding mode 7 and 14 respectively for the  $D_s \rightarrow K_s \mu \nu$  and

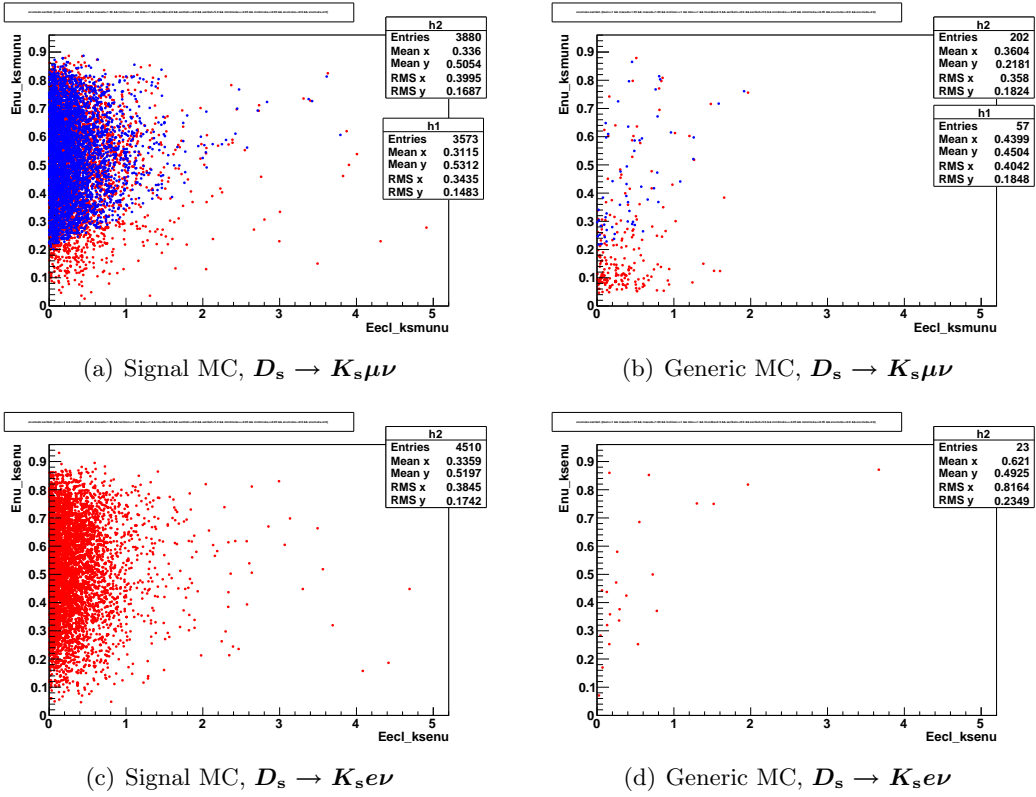


FIGURE 3.38:  $E_\nu$  vs.  $E_{ecl}$  for  $D_s \rightarrow K_s l \nu$  candidates. In  $D_s \rightarrow K_s \mu \nu$  mode: Blue Markers: for the events selected with Best  $(E_{ecl}, E_\nu)$  Selection Criteria

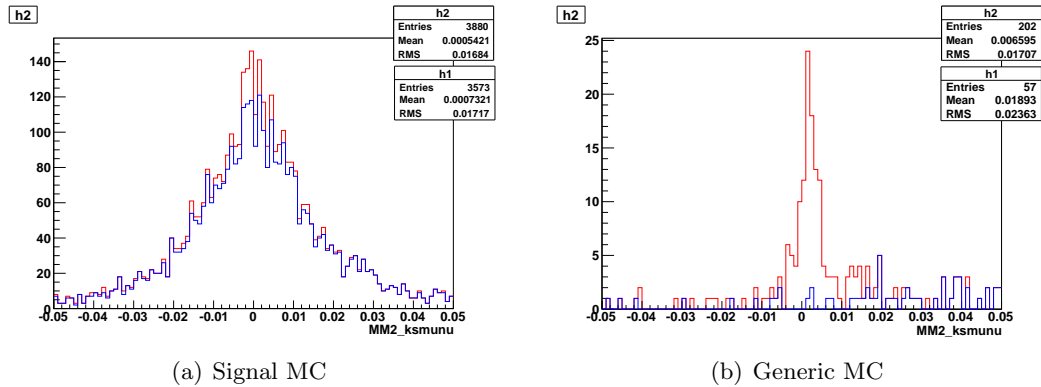


FIGURE 3.39:  $MM^2$  distribution for  $D_s \rightarrow K_s \mu \nu$  decay. Blue line: optimal  $(E_{ecl}, E_\nu)$  cuts. Red line: no  $(E_{ecl}, E_\nu)$  selection.

$D_s \rightarrow K_s e \nu$  channels with the fixed signal function  $f_s$  added to a cubic polynomial function as shown in Fig. 3.45. In case of  $D_s \rightarrow K_s \mu \nu$  mode, we restrict the upper limit of  $MM^2$  at 0.2, because of a bump between  $0.2 < MM^2 < 0.3$  that was difficult to fit. We use the Signal MC efficiency of 0.0572 and the number of exclusively reconstructed  $D_s \rightarrow K_s \mu \nu$  events in six streams of Generic MC to be  $3.18 \pm 8.09$ . With these numbers we get an estimation of the backgrounds in terms of a branching ratio to be  $(4 \pm 11) \times 10^{-5}$ . For  $D_s \rightarrow K_s e \nu$  decay, we use the signal efficiency of 0.0785. We

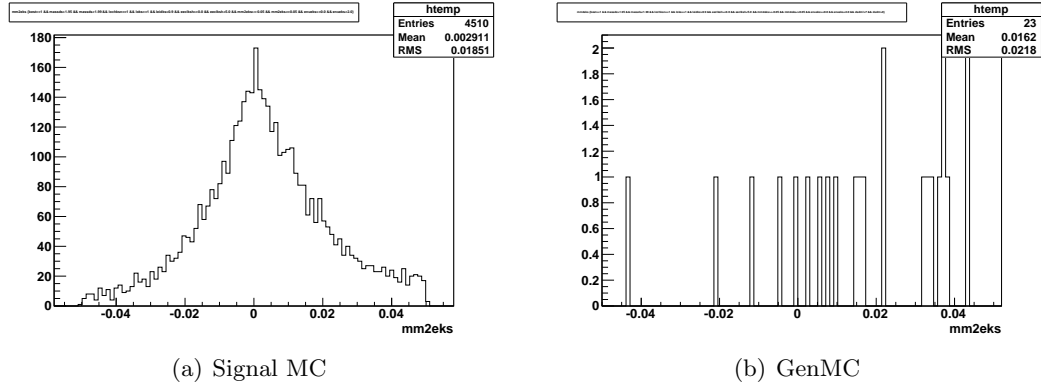


FIGURE 3.40:  $MM^2$  distribution of  $D_s \rightarrow K_s e \nu$ . No  $(E_{ecl}, E_\nu)$  selection is applied.

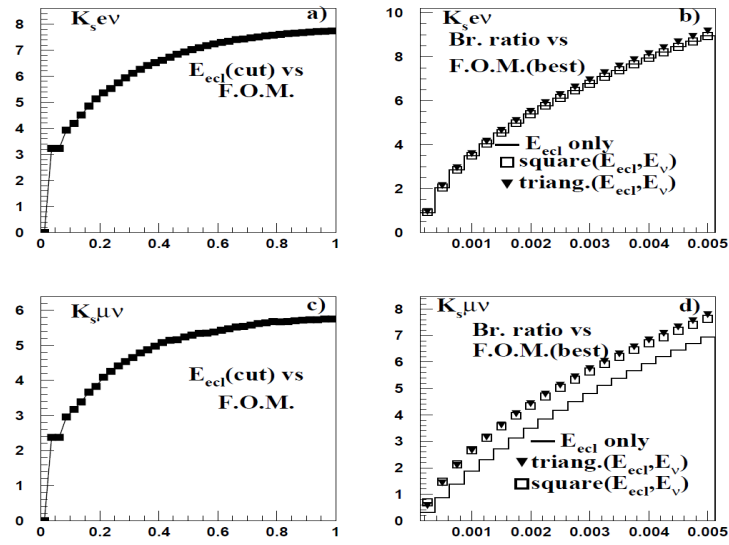
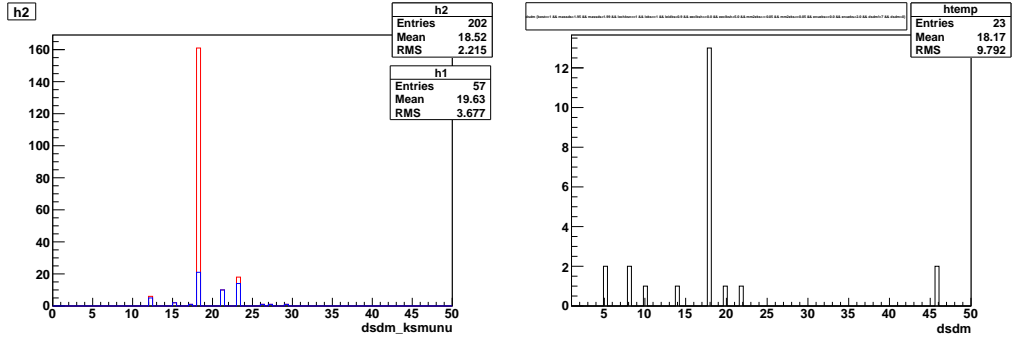


FIGURE 3.41: First row:  $D_s \rightarrow K_s e \nu$ , Second row:  $D_s \rightarrow K_s \mu \nu$ . First column: FOM versus  $E_{ecl}$  cut for nominal branching ratios as described in the text. Second column: optimized FOM as a function of the assumed branching ratio. FOM for  $E_{ecl}$ , “square” and “triangular” cuts are shown.

find that the number of exclusively reconstructed  $D_s \rightarrow K_s e \nu$  events in six streams of Generic MC is  $13.92 \pm 6.67$ . Based on these numbers, we estimate the irreducible backgrounds in data to correspond to a branching ratio in  $D_s \rightarrow K_s e \nu$  of  $(1.33 \pm 0.64) \times 10^{-4}$ . These systematics from background subtraction are not going to be dominant in the final analysis.

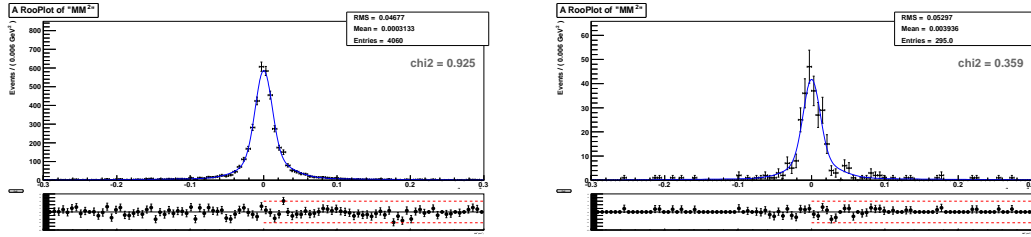
## Conclusions.

It is evident that, while the  $K_s l \nu$  analysis has small, manageable backgrounds, the other two analyses have significant irreducible backgrounds. Our proposal is to drop the  $\rho \mu \nu$



(a)  $D_s \rightarrow K_s \mu \nu$  candidates. Black line: (b)  $D_s \rightarrow K_s e \nu$  candidates. No optimal with optimal  $(E_{ecl}, E_\nu)$  cuts. Red line: no  $(E_{ecl}, E_\nu)$  cut

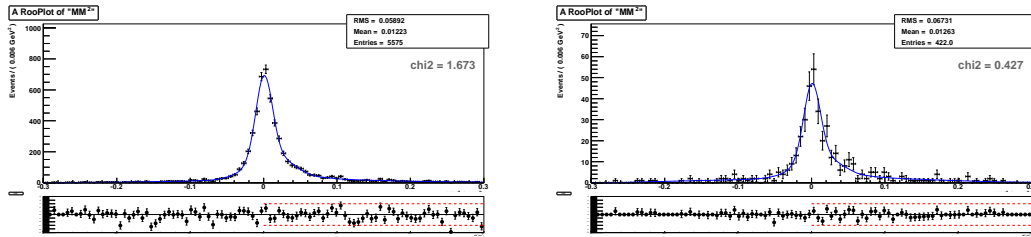
FIGURE 3.42: Generic MC dsdm distributions for  $D_s \rightarrow K_s l \nu$



(a) Signal MC, using only  $f_s$

(b) Gen. MC.

FIGURE 3.43: Fit to  $MM^2$  distribution for  $K_s \mu \nu$  candidates.



(a) Signal MC, using only  $f_s$

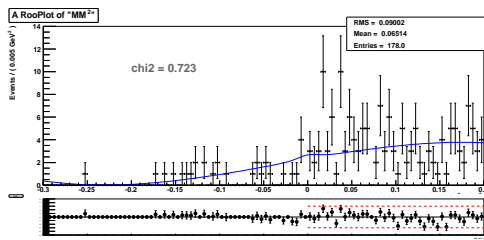
(b) Gen. MC.

FIGURE 3.44: Fit to  $MM^2$  distribution for  $K_s e \nu$  candidates.

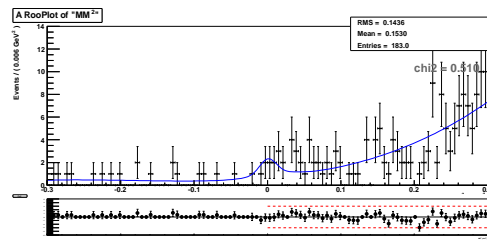
analysis from this paper, because one would have to trust the background subtraction error at the 8% level.

For completeness below we have added an Appendix showing the complete list of background modes. We have not found any particular mode that could create the small bumps seen in the  $(\pi^0, \rho) l \nu$  analyses.

The Appendix also shows the lepton probability distributions for signal and Generic MC. This is because  $\tau \nu$  backgrounds arise from imperfect lepton identification. We see no significant differences.



(a) Gen. MC background modes for  $K_s\mu\nu$  candidates (excluding mode 14) fitted with the  $f_s$  added to a cubic polynomial function



(b) Gen. MC background modes for  $K_se\nu$  candidates (excluding mode 7) fitted with the  $f_s$  added to a cubic polynomial function

FIGURE 3.45: Fit to  $MM^2$  distribution for  $K_sl\nu$  background candidates only in Generic MC

## Chapter 4

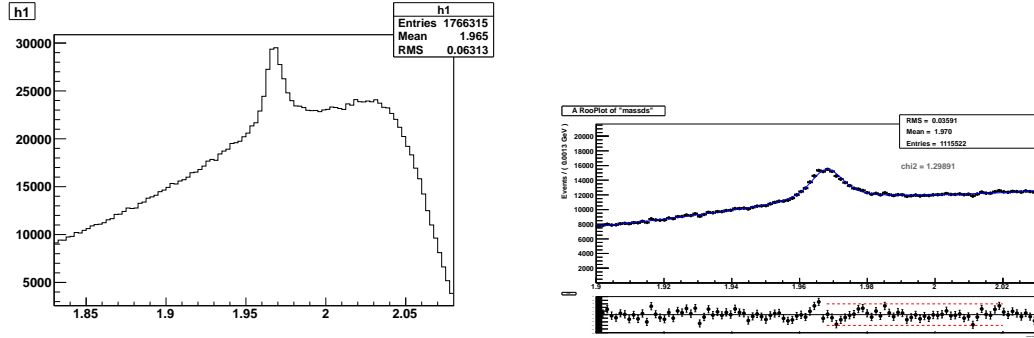
# Data analysis

### 4.1 Introduction

After we establish the best selection criteria for signal optimization for each of our channels using Monte Carlo data samples, we use real data to acquire the final result by fitting the  $MM^2$  distributions. We have decided to discard the  $\rho\mu\nu$  channel in the final analysis due to the presence of significantly large irreducible background contribution in this channel. We will discuss the fit procedures to fit the  $M_0$  and  $MM^2$  distributions for  $D_s \rightarrow \pi^0\mu\nu$ ,  $D_s \rightarrow \pi^0e\nu$ ,  $D_s \rightarrow K_s\mu\nu$ ,  $D_s \rightarrow K_se\nu$  and  $D_s \rightarrow \rho e\nu$  channels in data in the following sections.

### 4.2 Reconstruction of Inclusive $D_s$ candidates in Data

The reconstruction yield of inclusive sample of  $D_s$  meson is done by performing a binned maximum likelihood fit to the  $M_0$  ( $D_{tag}KX_{frag}\gamma$ ) distribution for all  $X_{frag}$  modes combined. 3.1.4. Fig. 4.1 shows the fit result with  $M_0 > 1.83$  and  $M_0 < 2.08$ , right and the histogram with  $M_0$  distribution in data is shown in the left. In the histogram we see a shoulder near 2.03 GeV and we cut off the shoulder and fit the  $M_0$  distribution in data with a Crystal ball function added to two Gaussian functions plus a quadratic Polynomial function between 1.9 and 2.02 GeV. We obtain a signal yield as:  $N_{D_s} = 119360.854 \pm 1095.88$  from the fit.



(a) Data:  $M_0$  distribution for correctly reconstructed inclusive  $D_s$  candidates with  $M_0 > 1.83$  and  $M_0 < 2.08$ .

(b) Data:  $M_0$  Fit with a Crystal ball added to two Gaussian functions plus a quadratic polynomial function for correctly reconstructed inclusive  $D_s$  events with  $M_0 > 1.9$  and  $M_0 < 2.03$ .

FIGURE 4.1: Fit to  $M_0$  distribution background candidates only in Generic MC

### 4.3 $D_s \rightarrow \pi^0 l \nu$ fit in Data

The  $MM^2$  distribution for  $D_s \rightarrow \pi^0 l \nu$  mode has been fitted in data with the signal function  $f_s$  as obtained from the signal MC fit and a quadratic polynomial function as a background added to it. The signal function  $f_s$  is defined in Section 3.6.2 as the sum of a Crystal Ball function and two Gaussian functions.

#### Muon mode:

The fit result in data is shown in Fig. 4.2 fitted with  $f_s$  added to a quadratic polynomial. In  $D_s \rightarrow \pi^0 \mu \nu$  channel the signal yield in data is  $N_s = 8.16 \pm 9.53$ . The  $\epsilon_{sigMC}$  is

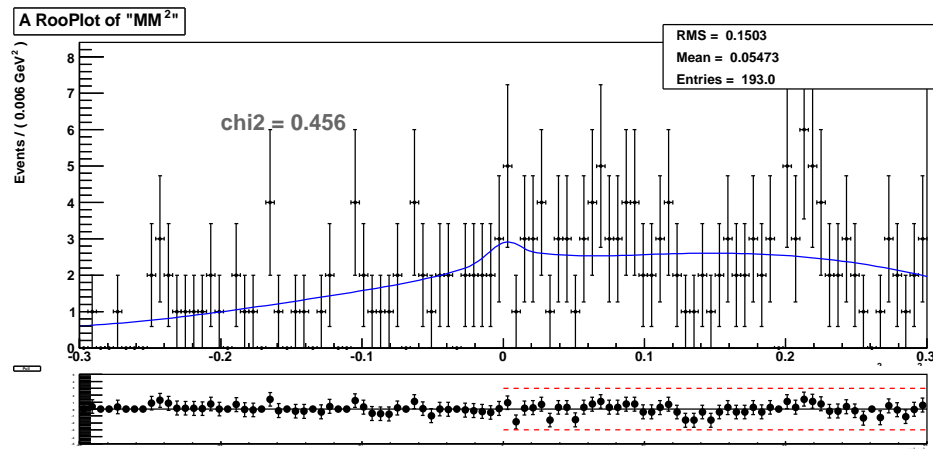


FIGURE 4.2: Data fit to  $MM^2$  for  $D_s \rightarrow \pi^0 \mu \nu$  decay. The signal function is obtained from the signal MC sample, plus a background shape of a quadratic polynomial.

0.0575. Using these numbers, the branching fraction of  $D_s \rightarrow \pi^0 \mu \nu$  channel in data is  $1.19 \pm 1.39 \times 10^{-3}$ .

### Electron mode:

Here  $f_s$  is used as mentioned in the previous section to fit the signal peak, the PDF of the background is again expressed by a quadratic polynomial function. The fit result in data is shown in Fig.4.3.

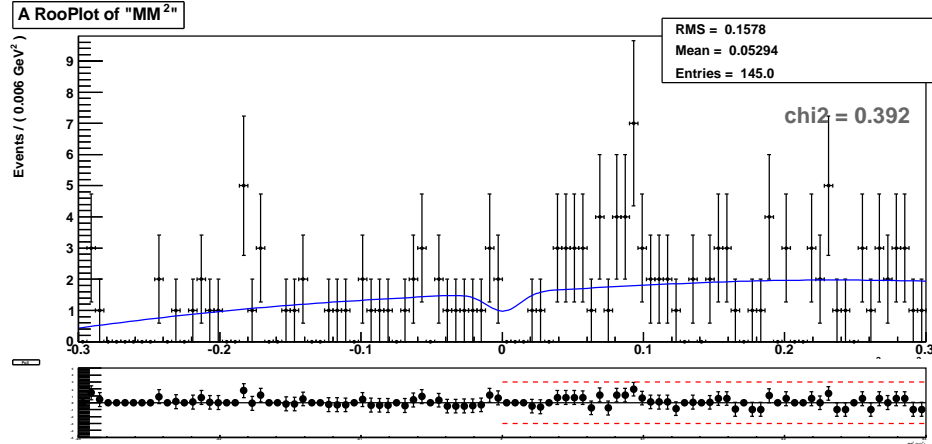


FIGURE 4.3: Data fit to  $MM^2$  for  $D_s \rightarrow \pi^0 e \nu$  decay. The signal function is obtained from the signal MC sample, plus a background shape as described in the text.

In  $D_s \rightarrow \pi^0 e \nu$  channel the signal yield in data is  $N_s = -13.40 \pm 12.35$ . The  $\epsilon_{sigMC}$  is 0.0615. The branching fraction of  $D_s \rightarrow \pi^0 e \nu$  channel in data is  $\mathcal{B} = -1.83 \pm 1.68 \times 10^{-3}$ .

#### 4.3.1 True branching fraction: $\mathcal{B}$ (in data)- $\mathcal{B}$ (in MC)

In  $D_s \rightarrow \pi^0 \mu \nu$  channel, the irreducible backgrounds correspond to a branching ratio of  $1.67 \pm 0.43 \times 10^{-3}$  in Monte Carlo. Subtracting the branching fraction in Monte Carlo from the branching fraction in data gives the true branching fraction  $\mathcal{B}$  in  $D_s \rightarrow \pi^0 \mu \nu$  channel:  $-0.48 \pm 1.45 \times 10^{-3}$ . Similarly, in  $D_s \rightarrow \pi^0 e \nu$  channel, the irreducible error produces a branching ratio in Monte Carlo:  $0.97 \pm 0.34 \times 10^{-3}$ . So the true branching fraction in this channel is  $-2.8 \pm 1.71 \times 10^{-3}$ . The error here is statistical only adding the statistical errors from data and MC quadratically. The systematics uncertainties will be discussed in the following subsection.

The two measurements average to a single measurement of  $-2.9 \pm 2.44 \times 10^{-3}$  for the branching ratio  $D_s \rightarrow \pi^0 l \nu$ . The result is not unlikely, if the true branching ratio is zero. The 90% confidence level (C.L.) limit is  $0.90 \times 10^{-3}$ , with only statistical errors considered.



### 4.3.2 Systematic errors

To be filled.

## 4.4 $D_s \rightarrow \rho e \nu$ fit in Data

For  $D_s \rightarrow \rho e \nu$  mode, a binned maximum likelihood fit has been performed to fit the  $MM^2$  distribution in data, with the signal function  $f_S$  from the signal MC fit plus a quadratic polynomial function. Here  $f_S$  is a combination of a crystal ball function added with two Gaussian functions. The fit result in data is shown in Fig.4.4.

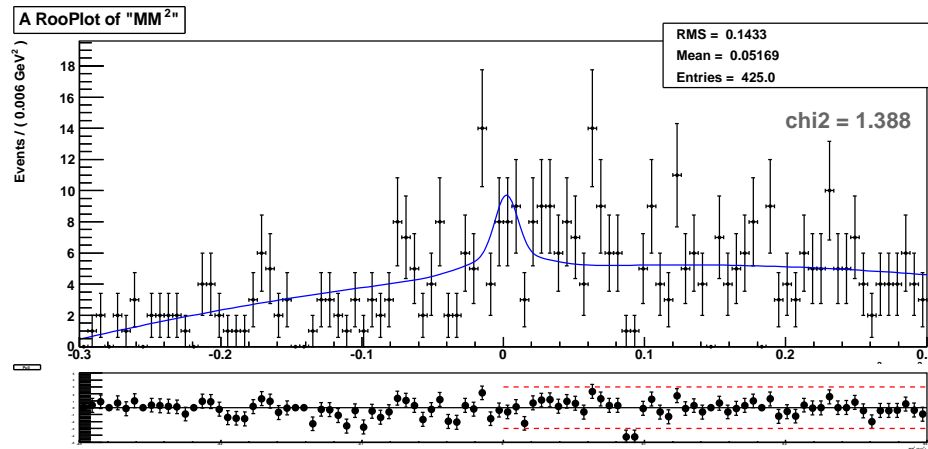


FIGURE 4.4: Data fit to  $MM^2$  for  $D_s \rightarrow \rho e \nu$  decay. The signal function  $f_S$  is from the signal MC sample, plus a quadratic background shape.

In  $D_s \rightarrow \rho e \nu$  channel the signal yield in data is  $N_s = 32.43 \pm 12.43$  and the  $\epsilon_{sigMC}$  is 0.0762. With these numbers, the branching fraction of  $D_s \rightarrow \rho e \nu$  channel in data is  $\mathcal{B} = 3.57 \pm 1.37 \times 10^{-3}$ .

#### 4.4.1 True branching fraction: $\mathcal{B}(\text{in data}) - \mathcal{B}(\text{in MC})$

In  $D_s \rightarrow \rho e \nu$  channel, the irreducible error produces a branching ratio in Monte Carlo:  $1.99 \pm 0.36 \times 10^{-3}$ . The  $f_0 e \nu$  background, which is not present in the generic MC data corresponds to a current branching ratio of  $2.00 \pm 0.32 \times 10^{-3}$ . Considering these contributions, the true branching fraction  $\mathcal{B}$  in  $D_s \rightarrow \rho e \nu$  channel:  $-0.42 \pm 1.45 \times 10^{-3}$  where the error has been obtained by a quadratic addition of the errors from data and MC.

The result is not unlikely, if the true branching ratio is zero. The 90% confidence level (C.L.) limit is  $1.54 \times 10^{-3}$ , with only statistical errors considered.

### 4.4.2 Systematic errors

To be filled.

## 4.5 $D_s \rightarrow K_s l \nu$ fit in Data

For  $D_s \rightarrow K_s l \nu$  mode also we perform a binned likelihood fit to the  $MM^2$  distribution in data, with the signal function  $f_s$  from the signal MC fit plus a quadratic polynomial function. The signal function  $f_s$  is the same as described subsection 4.2.

### Muon mode:

In the muon mode, the fit result in data is shown in Fig. 4.5 fitted with  $f_s$  and a background function made of a quadratic polynomial. In  $D_s \rightarrow K_s \mu \nu$  decay, we get a

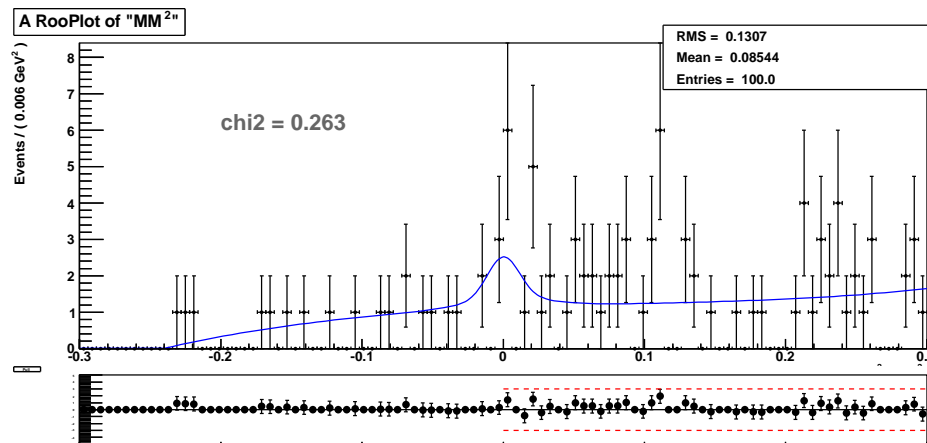


FIGURE 4.5: Data fit to  $MM^2$  for  $D_s \rightarrow K_s \mu \nu$ . The signal function  $f_s$  is from the signal MC sample and a quadratic background shape.

signal yield:  $N_s = 9.83 \pm 5.55$ . The efficiency of the exclusive decay of  $D_s \rightarrow K_s \mu \nu$  in Signal MC is:  $\epsilon_{sigMC}$  is 0.0572. The branching fraction of  $D_s \rightarrow K_s \mu \nu$  channel in data is  $\mathcal{B} = 1.44 \pm 0.81 \times 10^{-3}$ .

### Electron mode:

We fit the  $MM^2$  distribution for  $D_s \rightarrow K_s e \nu$  decay, using the fixed  $f_s(MM^2)$  function obtained from the signal MC sample and a quadratic background added to it as shown in the Fig. 4.6

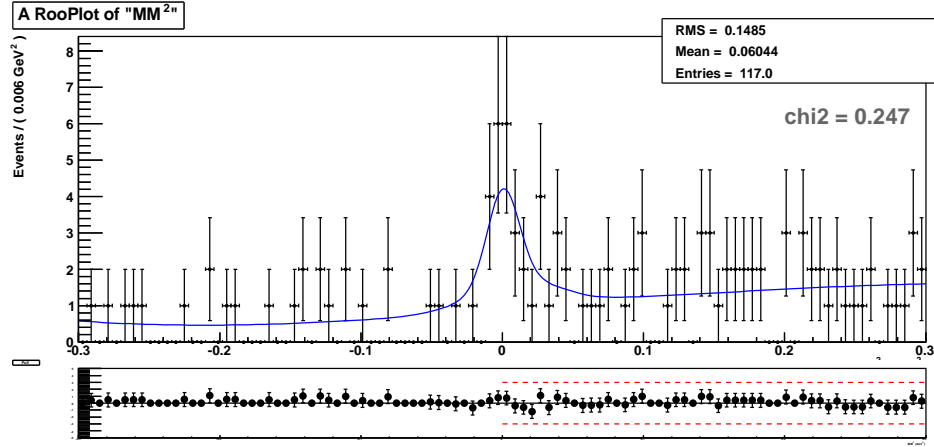


FIGURE 4.6: Data fit to  $MM^2$  for  $D_s \rightarrow K_s e \nu$ . The signal function  $f_s$  is from the signal MC sample, plus a quadratic background shape.

In  $D_s \rightarrow K_s e \nu$  channel the signal yield in data is  $N_s = 27.40 \pm 7.30$  and the  $\epsilon_{sigMC}$  is 0.0785. The branching fraction of  $D_s \rightarrow K_s e \nu$  channel in data is  $\mathcal{B} = 2.92 \pm 0.78 \times 10^{-3}$ .

#### 4.5.1 True branching fraction: $\mathcal{B}(\text{in data}) - \mathcal{B}(\text{in MC})$

In  $D_s \rightarrow K_s \mu \nu$  channel, the irreducible backgrounds correspond to a branching ratio of  $4 \pm 11 \times 10^{-5}$  in Monte Carlo. The true branching fraction  $\mathcal{B}$  in  $D_s \rightarrow K_s \mu \nu$  channel is  $1.40 \pm 0.82 \times 10^{-3}$ .

In  $D_s \rightarrow K_s e \nu$  channel, the irreducible error produces a branching ratio in Monte Carlo:  $1.33 \pm 0.64 \times 10^{-4}$ . The true branching fraction  $\mathcal{B}$  in  $D_s \rightarrow K_s e \nu$  channel is  $2.79 \pm 0.78 \times 10^{-3}$ . Here we are considering the statistical error from quadratic addition of statistical errors from data and MC. The two measurements average to a single measurement of  $4.15 \pm 1.13 \times 10^{-3}$  for the branching ratio  $D_s \rightarrow K_s l \nu$ , with only statistical errors considered.

#### 4.5.2 Systematic errors

To be filled.

## Chapter 5

# Conclusion

To summarize my research work, I have optimized the signal in each of our sub decay channels and calculated efficiencies in those channels and calculated the true branching fractions of each of these channels. The final branching fractions including the statistical errors are listed in the table 5.1.

TABLE 5.1: Final branching fractions  $\mathcal{B}$

Decay Mode	Final B.R.	PDG value
$D_s \rightarrow \pi^0 \mu \nu$	$< \times 10^{-3}$ (within 90% confidence level)	—
$D_s \rightarrow \pi^0 e \nu$	$< \times 10^{-3}$ (within 90% confidence level)	—
$D_s \rightarrow \pi^0 l \nu$	$< 0.90 \times 10^{-3}$ (within 90% confidence level)	—
$D_s \rightarrow \rho e \nu$	$< 1.54 \times 10^{-3}$ (within 90% confidence level)	—
$D_s \rightarrow K_s \mu \nu$	$1.40 \pm 0.82 \times 10^{-3}$	—
$D_s \rightarrow K_s e \nu$	$2.79 \pm 0.78 \times 10^{-3}$	$3.7 \pm 1.0 \times 10^{-3}$
$D_s \rightarrow K_s l \nu$	$4.15 \pm 1.13 \times 10^{-3}$	—

These are all world best measurements.

# Appendix A

## Appendix.

For  $D_s \rightarrow \pi^0 \mu \nu$  decay mode, the backgrounds come from:

- mode 1:  $\mu^+ \nu_\mu$
- mode 2:  $\tau^+ \nu_\tau$
- mode 11:  $\phi \mu^+ \nu_\mu$
- mode 12:  $\eta \mu^+ \nu_\mu$
- mode 13:  $\eta' \mu^+ \nu_\mu$
- mode 14:  $\bar{K}^0 \mu^+ \nu_\mu$
- mode 17:  $K^0 \bar{K}^0 \mu^+ \nu_\mu$
- mode 18:  $\bar{K}^0 K^+$
- mode 20:  $\phi \pi^+$
- mode 21:  $\bar{K}^{*0} K^+$
- mode 23:  $K^{*+} \bar{K}^0$
- mode 24:  $K^+ K^- p i^+ p i^0$
- mode 35:  $f_0 \pi^+$
- mode 36:  $f'_0 \pi^+$
- mode 37:  $f_0(1500) \pi^+$
- mode 38:  $f_2 \pi^+$

- mode 40:  $\eta\pi^+$
- mode 44:  $\pi^+\pi^+\pi^+\pi^-\pi^-\pi^0$
- mode 45:  $\eta'\pi^+$
- mode 46:  $\rho^+\eta'$
- mode 49:  $K^+\rho(2S)^0$

The dominant background modes in  $D_s \rightarrow \pi^0 e \nu$  are:

- mode 2:  $\tau^+\nu_\tau$
- mode 5:  $D_s \rightarrow \eta e^+\nu_e$
- mode 7:  $\bar{K}^0 e^+\nu_e$
- mode 30:  $K^+K^-\rho i^+\rho i^+\rho i^-$
- mode 35:  $f_0\pi^+$
- mode 49:  $K^+\rho(2S)^0$

Most of the background events for  $D_s \rightarrow \rho\mu\nu$  decay are coming from:

- mode 2:  $\tau^+\nu_\tau$
- mode 11:  $\phi\mu^+\nu_\mu$
- mode 12:  $\eta\mu^+\nu_\mu$
- mode 13:  $\eta'\mu^+\nu_\mu$ ,
- mode 14:  $\bar{K}^0\mu^+\nu_\mu$
- mode 15:  $\bar{K}^{*0}\mu^+\nu_\mu$
- mode 16:  $K^+K^-\mu^+\nu_\mu$
- mode 19:  $K^+K^+\pi^-$
- mode 20:  $\phi\pi^+$
- mode 21:  $\bar{K}^{*0}K^+$
- mode 22:  $\bar{K}^{*0}K^+$
- mode 23:  $K^{*+}\bar{K}^0$

- mode 24:  $K^+K^-\pi^+\pi^0$
- mode 27:  $\bar{K}^0K^+\pi^+\pi^-$
- mode 29:  $\bar{K}^{*0}K^{*+}$
- mode 34:  $\pi^+\pi^+\pi^-$
- mode 35:  $f_0\pi^+$
- mode 36:  $f'_0\pi^+$
- mode 37:  $f_0(1500)\pi^+$
- mode 38:  $f_2\pi^+$
- mode 40:  $\eta\pi^+$
- mode 41:  $\omega\pi^+$
- mode 45:  $\eta'\pi^+$
- mode 46:  $\rho^+\eta'$
- mode 47:  $K^+\pi^+\pi^-$
- mode 48:  $\rho^0K^+$
- mode 50:  $K^{*0}\pi^+$

In Fig. 3.25, we identify the peak in  $D_s \rightarrow \rho\mu\nu$  (in blue: with the optimal  $(E_{ecl}, E_\nu)$  cuts) near  $MM^2 \approx 0$  to be coming dominantly from mode 13 and mode 45.

The dominant background mode in  $D_s \rightarrow \rho e\nu$  is

- mode 2:  $\tau^+\nu_\tau$
- mode 4:  $\phi e^+\nu_e$
- mode 5:  $D_s \rightarrow \eta e^+\nu_e$
- mode 6:  $\eta' e^+\nu_e$
- mode 8:  $\bar{K}^{*0} e^+\nu_e$
- mode 9:  $K^+K^- e^+\nu_e$
- mode 16:  $K^+K^- \mu^+\nu_\mu$
- mode 20:  $\phi\pi^+$

- mode 21:  $\bar{K}^{*0}K^+$
- mode 22:  $\bar{K}^{*0}K^+$
- mode 35:  $f_0\pi^+$
- mode 36:  $f'_0\pi^+$
- mode 37:  $f_0(1500)\pi^+$
- mode 40:  $\eta\pi^+$
- mode 41:  $\omega\pi^+$
- mode 43:  $\pi^+\pi^+\pi^-\pi^-\pi^0$
- mode 44:  $\pi^+\pi^+\pi^-\pi^-\pi^0$
- mode 45:  $\eta'\pi^+$ ,
- mode 47:  $K^+\pi^+\pi^-$
- mode 48:  $\rho^0K^+$
- mode 49:  $K^+\rho(2S)^0$

The side-to-side comparisons of lepton probability distributions for signal and Generic MC are shown in Figs.A.1 to A.4.

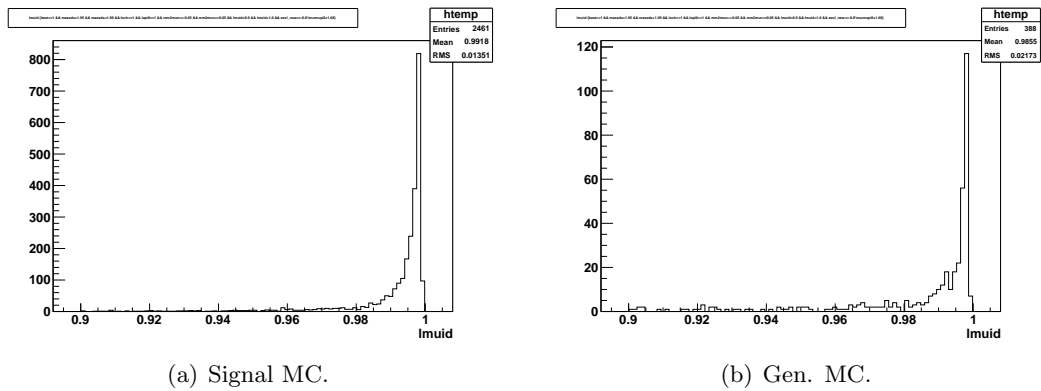
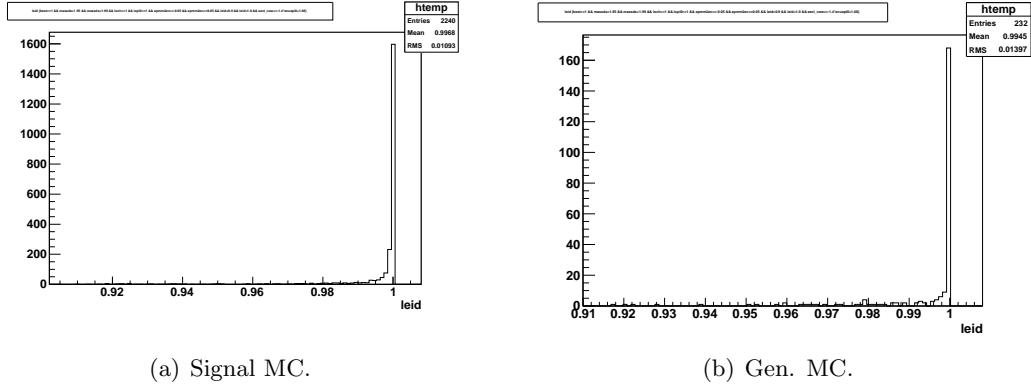
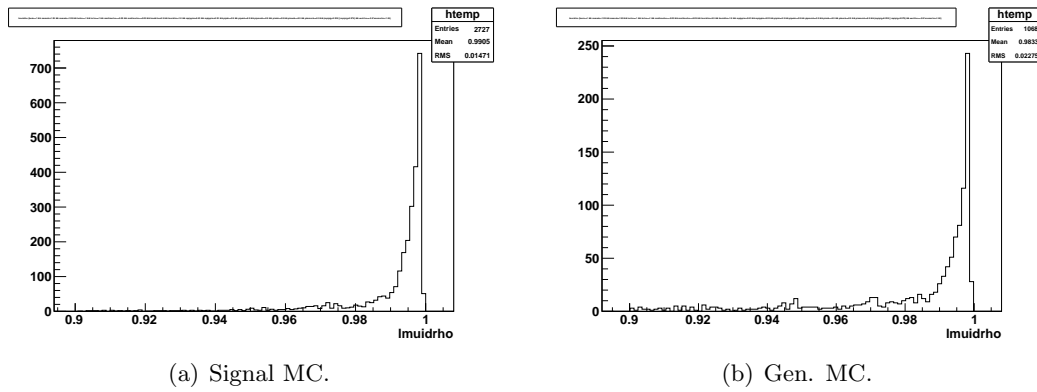
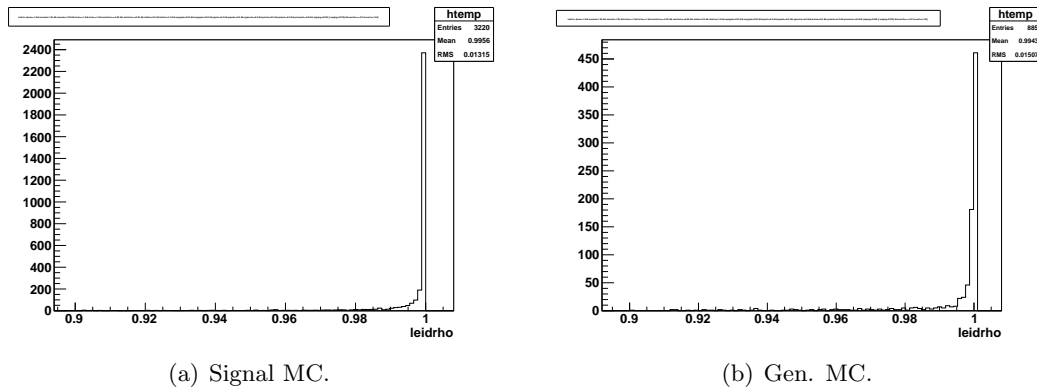


FIGURE A.1:  $\pi^0\mu\nu$  muon probability distributions, for  $-0.05 < MM^2 < 0.05$ .



FIGURE A.2:  $\pi^0 e \nu$  electron probability distributions, for  $-0.05 < MM^2 < 0.05$ .FIGURE A.3:  $\rho \mu \nu$  muon probability distributions, for  $-0.05 < MM^2 < 0.05$ .FIGURE A.4:  $\rho e \nu$  electron probability distributions, for  $-0.05 < MM^2 < 0.05$ .

# Bibliography

- [1] D.J. Gross, F.Wilczek, Phys. Rev. Lett, 30:1343, 1973.
- [2] H.D. Politzer, Phys. Rev. Lett, 30:1346 1973.
- [3] D. Perkins, Introduction to High Energy Physics, 4th ed.(Cambridge University Press, 2000)
- [4] S. Glashow, Nucl. Phys. 22, 579 (1961).
- [5] A. Salam and J. Ward, Phys. Lett. 13, 168 (1964).
- [6] S.Weinberg, Phys. Rev. Lett. 19, 1264 (1967).
- [7] CKM Fitter Group, J. Charles *et al.*, Eur. Phys. J. C41, 1 (2005), updated results and plots available at: <http://ckmfitter.in2p3.fr>.
- [8] E. Noether. Math. Phys., pages 235257, 1918.
- [9] N. Cabibbo. Phys. Rev. Lett., 10:531533, 1963.
- [10] L.L. Chau and W.-Y. Keung (1984). "Comments on the Parametrization of the Kobayashi-Maskawa Matrix". Physical Review Letters 53 (19): 1802.
- [11] Wu, C. S.; Ambler, E; Hayward, R. W.; Hoppes, D. D.; Hudson, R. P. (1957).
- [12] Muzzin, S. T. (19 March 2010).
- [13] J.E. Augustin *et al.* Phys. Rev. Lett., 33:1406, 1974.
- [14] J.J. Aubert *et al.* Phys. Rev. Lett., 33:1404, 1974.
- [15] G. P. Lepage and S. J. Brodsky. Phys. Rev. D, 22:21572198, 1980.
- [16] S. J. Brodsky *et al.* Phys. Rept., 301:299486, 1998.
- [17] K. Abe *et al.* Phys. Rev. Lett., 98:082001, 2007.
- [18] B. Aubert *et al.* Phys. Rev. D, 73:011101, 2006.

- 
- [19] Q. He *et al.* Phys. Rev D, 74:091104, 2006.
- [20] S. K. Choi *et al.* Phys. Rev. Lett., 100:142001, 2008.
- [21] F. E. Close and P. R. Page. Physics Letters, B578:219, 2003.
- [22] M. B. Voloshin. Phys. Lett., B579:316, 2004.
- [23] N. A. Torngvist. Physics. Letters, B590:209, 2004.
- [24] E. S. Swanson. Physics Letters, B588:189, 2004.
- [25] E. Braaten and M. Kusunoki. Phys. Rev. D, 69:114012, 2004.
- [26] C. Y. Wong. Phys. Rev. C, 69:055202, 2004.
- [27] I. Bigi *et al.* Phys. Rev. D, 72:114016, 2005.
- [28] L. Maiani *et al.* Phys. Rev. D, 72:031502, 2005.
- [29] T. W. Chiu and T. H. Hsieh. Physics Letters, B646:205, 2007.
- [30] A. Abashian *et al.* [BELLE Collaboration], Nucl. Instrum. Meth. A 479, 117 (2002).
- [31] S. Uno, Nucl. Instrum. and Meth. A 379, 421 (1996); H. Hirano *et al.*, KEK Preprint 2000-2; M. Akatsu *et al.*, DPNU-00-06.
- [32] Th. Peters, Die Kettenlinie, [www.mathe-seiten.de](http://www.mathe-seiten.de) (2004)
- [33] <http://mathsrv.ku-eichstaett.de/MGF/homes/grothmann/Projekte/Kettenlinie/>
- [34] P. Marmier E. Sheldon, Physics of Nuclei and Particles, Vol. 1, Academic Press, New York (1969)
- [35] J.V. Jelley, Cherenkov Radiation and its Applications, Pergamon Press, London/New York (1958)
- [36] H. Ikeda *et al.*, Nucl. Instrum. Meth. A 441, 401 (2000).
- [37] J. L. Rosner and S. Stone, arXiv:1201.2401 [hep-ex].
- [38] T. Sjostrand, "PYTHIA 5.7 and JETSET 7.4: Physics and manual," arXiv:hep-ph/9508391.
- [39] T. Sjostrand, P. Eden, C. Friberg, L. Lonnblad, G. Miu, S. Mrenna and E. Norrbin, "High energy- physics event generation with PYTHIA 6.1," Computer Physics Commun. 135 238(2001).

- [40] R. Brun, R. Hagelberg, M. Hanstroul, and J. C. Lasalle, "Geant: Simulation Program For Particle Physics Experiments. User Guide And Reference Manual," CERN-DD-78-2-REV ; R. Brun *et al.*, GEANT 3.21, CERN Report DD/EE/84-1 (1984).
- [41] EvtGen-A Monte Carlo Generator for B-Physics; February 5, 2004.
- [42] A. Zupanc *et al.* (Belle Collaboration) JHEP 1309, 139 (2013).
- [51] L. Widhalm *et al.* (Belle Collaboration), Phys. Rev. Lett. 100, 241801 (2008). L. Widhalm, Belle Note 997.
- [52] P. del Amo Sanchez *et al.* (BaBar Collaboration), Phys. Rev. D 82, 091103 (2010) [arXiv:1008.4080].
- [45] K. Abe *et al.*, Phys.Rev.Lett. 98, 082001 (2007).
- [46] B. Aubert *et al.*, Phys.Rev. D73, 011101 (2006).
- [47] Q. He *et al.*, Phys.Rev.D74, 091104 (2006).
- [48] S. K. Choi *et al.*,Phys.Rev.Lett. 100, 142001 (2008).
- [49] A. Abashian *et al.* (Belle Collaboration), Nucl. Instrum. Methods Phys. Res. Sect. A 479, 117 (2002); also see detector section in J.Brodzicka *et al.*, Prog. Theor. Exp. Phys. (2012) 04D001.
- [50] S. Kurokawa and E. Kikutani, Nucl. Instrum. Methods Phys. Res. Sect. A 499, 1 (2003), and other papers included in this Volume; T.Abe *et al.*, Prog. Theor. Exp. Phys. (2013) 03A001 and following articles up to 03A011.
- [51] L. Widhalm *et al.* (Belle Collaboration), Phys. Rev. Lett. 100, 241801 (2008). L. Widhalm, Belle Note 997.
- [52] P. del Amo Sanchez *et al.* (BaBar Collaboration), Phys. Rev. D 82, 091103 (2010) [arXiv:1008.4080].
- [53] S. Nishida, Study of Kaon and Pion Identification Using Inclusive D\* Sample, Belle internal note 779
- [54] K. Hanagaki *et al.* Electron Identification in Belle. In: Nucl.Instrum.Meth. A485 (2002), p. 490. eprint: arXiv:hep-ex/0108044v1.
- [55] J. Beringer *et al.* (Particle Data Group), Phys. Rev. D 86, 010001 (2012) and 2013 partial update for the 2014 edition.